

# POLITECNICO DI TORINO

Collegio di Ingegneria Chimica e dei Materiali

**Master of Science Course  
in Materials Engineering**

Master of Science Thesis

## **Rheological conditions to obtain all-polymer composites with fibrillar structure: a simulation-based approach**



**Tutor**

Prof.ssa Rossella Arrigo  
Prof. Alberto Frache

**Candidate**

Eugenia Montaldo

March 2021



# Index

|  |    |
|--|----|
| I. Riassunto in italiano per tesi in inglese .....                   | 1  |
| 1. Introduction.....   | 15 |
| 1.1 Description of fibrillar composites and production process ..... | 16 |
| 1.2 Fibrils in PET .....   | 17 |
| 1.3 Fibrils in PTFE.....   | 38 |
| 1.4 Fibrils in PA6.....  | 50 |
| 1.5 Fibrils in PC .....  | 55 |
| 2. Extruders and Ludovic Software .....                              | 60 |
| 2.1 Description of an extruder .....                                 | 60 |
| 2.2 Ludovic Software.....  | 62 |
| 2.2.1 Molten polymers' behavior.....                                 | 62 |
| 2.2.2 Geometrical description of Ludovic's elements .....            | 63 |
| 2.2.3 Ludovic's mechanical model for screw and die elements .....    | 67 |
| 2.2.4 Ludovic's thermal model for screw and die elements .....       | 70 |
| 2.2.5 How to set a simulation with Ludovic software .....            | 72 |
| 3. Materials and methods .....                                       | 75 |
| 3.1 Materials .....  | 75 |
| 3.2 Setting of Ludovic simulations .....                             | 78 |
| 3.2.1 "Extruder" section.....  | 79 |
| 3.2.2 "Products" section.....  | 80 |
| 3.2.3 "Process" section .....  | 81 |
| 4. Results and discussion .....                                      | 82 |
| 4.1 Analysis of the obtained results .....                           | 82 |
| 4.1.1 Simulation 1 – 120rpm - PP 70% + PET 30%.....                  | 82 |
| 4.1.1.1 Temperature .....  | 82 |
| 4.1.1.2 Shear Rate .....   | 83 |
| 4.1.1.3 Viscosity .....  | 84 |
| 4.1.2 Simulation 2 – 180rpm - PP 70% + PET 30%.....                  | 85 |
| 4.1.2.1 Temperature .....  | 86 |
| 4.1.2.2 Shear Rate .....   | 86 |
| 4.1.2.3 Viscosity .....  | 87 |
| 4.1.3 Simulation 3 – 200rpm - PP 70% + PET 30%.....                  | 87 |
| 4.1.3.1 Temperature .....  | 88 |
| 4.1.3.2 Shear Rate .....   | 88 |
| 4.1.3.3 Viscosity .....  | 89 |

|   |     |
|---|-----|
| 4.1.4 Simulation 4 – 250rpm - PP 70% + PET 30%.....                     | 89  |
| 4.1.4.1 Temperature .....   | 90  |
| 4.1.4.2 Shear Rate .....  | 90  |
| 4.1.4.3 Viscosity .....   | 91  |
| 4.1.5 Simulation 5 – 120rpm and PP 90% + PET 10% .....                  | 91  |
| 4.1.5.1 Temperature .....   | 92  |
| 4.1.5.2 Shear Rate .....  | 92  |
| 4.1.5.3 Viscosity .....   | 93  |
| 4.1.6 Simulation 6 – 120 rpm and change in the temperature profile..... | 93  |
| 4.1.6.1 Temperature .....   | 94  |
| 4.1.6.2 Shear Rate .....  | 94  |
| 4.1.6.3 Viscosity .....   | 95  |
| 4.1.7 Residence Time.....   | 95  |
| 4.2 Conditions to obtain fibrillation.....                              | 99  |
| 5. Conclusions.....   | 104 |
| 6. References.....  | 105 |

## I. Riassunto in italiano per tesi in inglese

I materiali compositi e nanocompositi a base polimerica hanno suscitato un interesse costantemente crescente negli ultimi decenni, grazie alle loro proprietà, sia funzionali che strutturali, migliorate rispetto a quelle delle matrici polimeriche di partenza. Infatti, l'introduzione di micro- e nanoparticelle all'interno di diversi sistemi polimerici, garantisce l'ottenimento di proprietà meccaniche, ottiche, elettriche e termiche superiori, permettendo un ampliamento del campo di applicazione tipico dei polimeri termoplastici. Tuttavia, affinché il miglioramento delle proprietà del polimero di partenza venga effettivamente raggiunto, è necessario che sia ottenuta una distribuzione ottimale delle cariche all'interno della matrice, riuscendo ad evitare i fenomeni di aggregazione tipici delle particelle comunemente utilizzate, e raggiungendo un buon livello di adesione interfacciale fra la matrice e la carica. Inoltre, l'utilizzo di micro- e nanocariche frequentemente pone problemi legati alla sicurezza, oltre a limitare le possibilità di riciclo dei materiali compositi.

Per cercare di porre una soluzione a queste problematiche, negli ultimi anni stanno suscitando un interesse sempre maggiore compositi detti "all-polymers" in cui sia la fase matrice sia la fase dispersa sono costituiti da materiale polimerico; in particolare, il polimero che funge da fase dispersa, viene sottoposto a particolari condizioni di flusso tali da generare la formazione di micro- o nano-fibrille che fungono da rinforzo direttamente durante il processo di lavorazione. La formulazione dei compositi "all-polymers", inoltre, permette la valorizzazione di materiale polimerico proveniente da processi di riciclo meccanico, in quanto la frazione in polvere che solitamente costituisce un sottoprodotto delle operazioni di riciclo meccanico può essere utilizzata come fase fibrillare di rinforzo.

Infatti, ai giorni nostri, il continuo aumento della produzione e del consumo della plastica rappresenta una grande sfida da un punto di vista ambientale in quanto il massiccio consumo di materie plastiche implica un aumento costante della quantità di rifiuti in questo materiale che si ritrovano ad essere dispersi nell'ambiente terrestre e marino. Per questo, le strategie di riciclo e riutilizzo delle materie plastiche a fine vita come alternativa allo smaltimento in discarica (e/o mediante l'inceneritore) stanno suscitando un interesse sempre maggiore e una grande attenzione è volta a trovare nuovi metodi per l'impiego di questi materiali. Nella maggior parte dei casi, materiali polimerici provenienti da processi di riciclo meccanico trovano impiego nella formulazione di miscele polimeriche, in cui solitamente si trovano ad essere accoppiati con determinate quantità dello stesso polimero vergine. Negli ultimi anni, grazie alle ricerche svolte nel campo dei compositi "all-polymers", sta diventando particolarmente interessante il potenziale utilizzo di materiale plastico proveniente da riciclo come fase di rinforzo in sistemi di questo tipo. In particolare, i materiali vengono sottoposti a lavorazione da fuso in determinate condizioni di flusso, tali da permettere la formazione della fase dispersa "in-situ", direttamente all'interno della matrice durante lo step di lavorazione, sotto forma di fibrille, aventi diametro nell'ordine dei micro- o nano-metri.

Poiché la produzione di questi compositi interamente polimerici è un processo relativamente nuovo, la prima parte del presente elaborato è dedicata ad una accurata analisi dei sistemi di questo tipo già presenti in letteratura. Nello specifico, l'attenzione è stata rivolta principalmente allo studio delle condizioni operative imposte durante il processo in estrusione che portano alla formazione di micro- o nanofibrille costituite dalla fase dispersa.

In particolare, dall'analisi dei pochi lavori presenti in letteratura sull'argomento, è emerso che i materiali principalmente impiegati per la creazione della fase rinforzante di forma fibrillare sono il polietilentereftalato (PET), il politetrafluoroetilene (PTFE o Teflon), la poliammide (PA) ed il policarbonato (PC). Indipendentemente dal polimero utilizzato, le fibrille rinforzanti

possono avere diametro compreso fra 1 e 10  $\mu\text{m}$  e, dunque, dare vita a compositi microfibrillari, oppure dell'ordine di 50-150 nm; in quest'ultimo caso, i compositi vengono detti nanofibrillari.

Come già anticipato prima, affinché si ottenga la fibrillazione in-situ della fase polimerica che funge da rinforzo, è necessario selezionare i parametri di processo ottimali. Nel meccanismo di deformazione della fase dispersa, che porta poi all'ottenimento delle fibrille, fondamentale risulta la conoscenza del numero capillare del sistema polimerico in esame e, soprattutto, l'influenza dei parametri operativi del processo di estrusione su tale parametro. Il numero capillare,  $Ca$ , è definito come il rapporto tra gli stress di natura viscosa e quelli interfacciali ed il suo valore risulta essere determinante nella predizione della morfologia di una miscela polimerica. Inoltre, la formazione delle fibrille dipende anche da un altro parametro: il rapporto di viscosità  $p$ , definito come il rapporto tra la viscosità della fase rinforzante e quella della matrice. Per poter quindi prevedere la possibilità di formazione di compositi "all-polymers" fibrillati è indispensabile la conoscenza dei suddetti parametri e dell'influenza delle condizioni operative del processo di estrusione (quali profilo delle viti, profilo di temperatura, velocità di rotazione delle viti, portata, ecc.) su tali parametri.

Dall'analisi dei lavori presenti in letteratura sull'argomento è stato possibile individuare due diverse strategie per l'ottenimento di tale tipologia di materiali.

La prima prevede l'ottenimento di compositi fibrillati sottoponendo i materiali ad un processo di estrusione condotto ad una temperatura di processo inferiore rispetto a quella di fusione del materiale rinforzante. In questo caso, quindi, la fase dispersa rimane allo stato solido durante l'estrusione, mentre la matrice si trova allo stato fuso. Tale processo è comunemente impiegato per l'ottenimento di compositi fibrillati in cui la fase dispersa sia costituita da PTFE. In questo caso, il polimero che costituisce la fase dispersa deve essere introdotto all'interno dell'estrusore sotto forma di polvere avente determinate caratteristiche geometriche. Gli sforzi di taglio subiti dalle particelle di PTFE all'interno dell'estrusore inducono una variazione della forma cristallina prevalente dei cristalli di PTFE, causando l'ottenimento di forme fibrillari. La variazione della morfologia che si ottiene tipicamente durante un processo di questo tipo è mostrata in Figura 1.

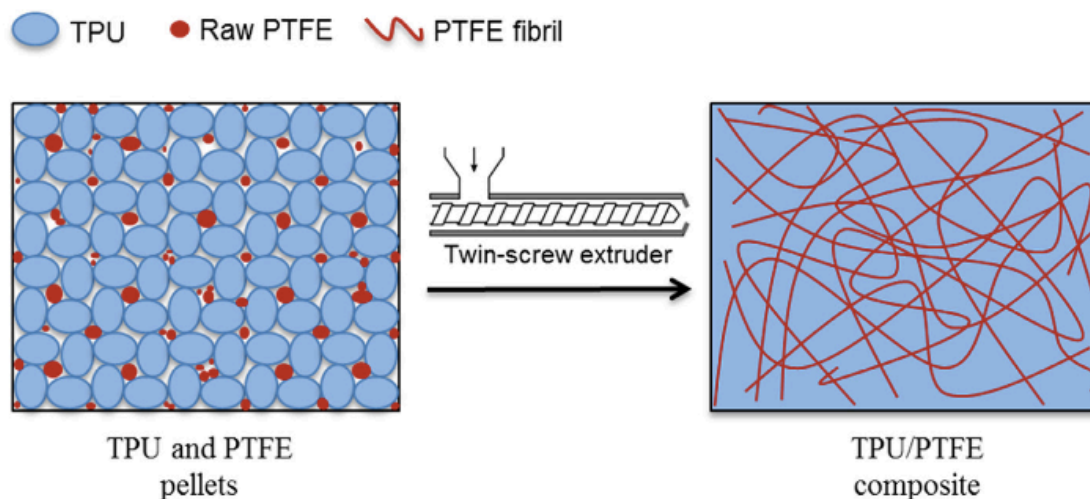


Figura 1. Schema rappresentante la formazione di fibrille del PTFE.

Il PTFE si presta bene ad una lavorazione di questo tipo grazie alla sua elevata cristallinità e alla bassa densità di *entanglements* nelle catene polimeriche. Il solo processo di *compounding* ad una temperatura inferiore alla temperatura di fusione ( $T_m$ ) del PTFE, infatti, è sufficiente per ottenere la deformazione plastica della fase dispersa, che assume la forma fibrillare direttamente all'interno della matrice sottoposta a sforzo di taglio. Tipicamente, le fibrille ottenuti in processi

simili a quello descritto, portano all'ottenimento di fibrille molto sottili, aventi diametro nell'ordine di 1  $\mu\text{m}$ , le quali subiscono un processo di *entangling* durante la miscelazione, con il risultato di dare vita all'interno della matrice ad un network con elevate capacità rinforzanti. La formazione di tale network tridimensionale disperso all'interno del polimero che funge da matrice, provoca una notevole variazione del comportamento reologico del materiale (Figura 2). Infatti, prove in frequenza condotte in flusso di shear hanno mostrato come i materiali fibrillati mostrino un comportamento tipicamente solid-like che implica un aumento dei valori di viscosità complessa nella regione a basse frequenze, e un corrispondente aumento dei valori dei moduli conservativo e dissipativo. Inoltre, le curve dei moduli in funzione della frequenza mostrano una diminuzione della pendenza nella regione a basse frequenze, con l'ottenimento di un plateau. Tali notevoli variazioni del comportamento reologico rispetto a quello della matrice pura sono da imputare all'azione del network formato dalle fibrille che, ostacolando le dinamiche delle macromolecole della matrice, causano un arresto dei processi di rilassamento delle catene polimeriche.

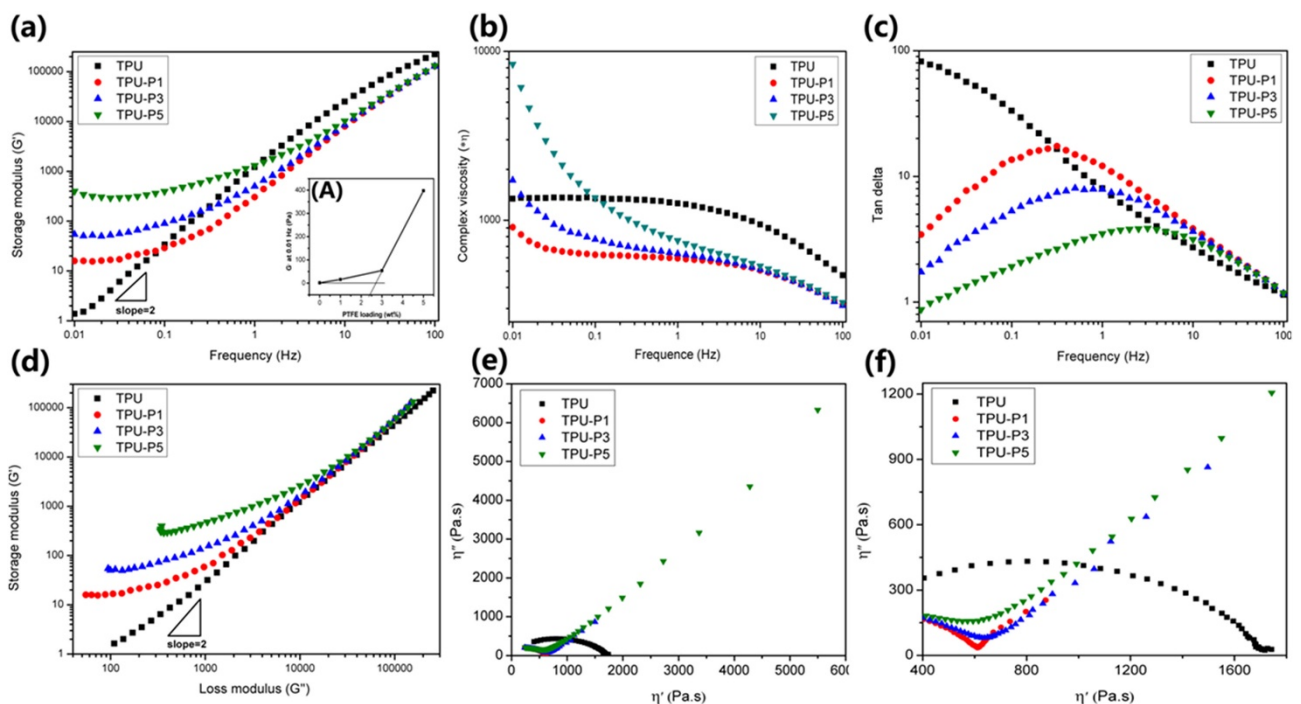


Figura 2. Proprietà reologiche di compositi “all-polymers” contenenti microfibrille di PTFE.

Molti lavori presenti in letteratura riportano inoltre un processo ulteriore di “hot stretching” a cui il materiale in uscita dall'estrusore viene sottoposto per permettere una stabilizzazione della forma e delle dimensioni delle fibrille formate durante il processo.

Il secondo metodo riportato in letteratura per ottenere compositi polimerici fibrillari prevede invece di miscelare i due materiali all'interno dell'estrusore entrambi allo stato fuso. Secondo questa seconda strategia, si parte da una tipica miscela polimerica costituita da polimeri immiscibili e si induce, attraverso specifiche condizioni di processo che generano un determinato campo di flusso all'interno dell'estrusore, la deformazione delle gocce che costituiscono la fase dispersa fino alla formazione di strutture fibrillari.

In questo caso, il tipico processo di produzione prevede tre stadi successivi (Figura 3):

### 1) Mixing Step

I due materiali allo stato fuso e con due temperature di fusione diverse di almeno 40°C vengono miscelati all'interno di un estrusore.

## 2) Fibrillation Step

I due materiali sono sottoposti ad un processo di trafilatura a freddo o di stiramento a caldo o a freddo, in modo da dare vita alla forma fibrillare della fase dispersa.

## 3) Isotropization Step

Il materiale ottenuto dallo stadio precedente è sottoposto ad un trattamento termico ad una temperatura intermedia tra le due temperature di fusione dei due materiali. A volte, questo passaggio viene portato a termine mediante la tecnica dello stampaggio ad iniezione o a compressione.

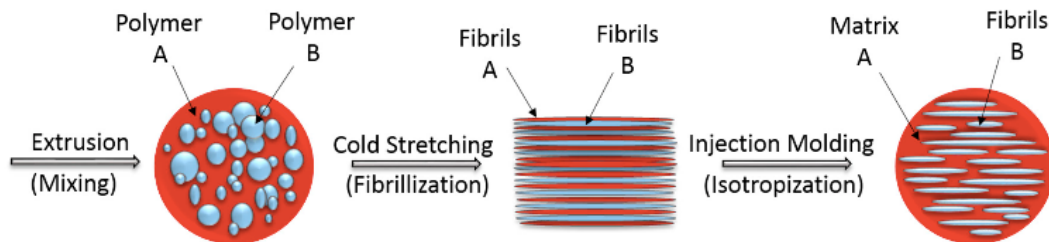


Figura 3. Rappresentazione schematica del processo di produzione di compositi fibrillari a partire dai due materiali fusi.

Il polietilentereftalato (PET) è tra i termoplastici più comunemente usati per produrre fibrille di rinforzo in compositi interamente polimerici, usando questa seconda metodologia. Ad esempio, Fakirov et al. [3] hanno utilizzato il processo descritto sopra per produrre compositi nanofibrillari polimerici costituiti da una matrice di polipropilene (80% in peso) con fibrille di PET (20% in peso) come rinforzo. I due polimeri sono stati lavorati in un estrusore bivite a 30 rpm e con un profilo di temperatura di 260-270-260-245 °C. La miscela così ottenuta è stata quindi sottoposta ad un processo di trafilatura a 130 °C per ottenere un composito con fase di rinforzo fibrillata. La caratterizzazione morfologica dei materiali ottenuti ha evidenziato l'ottenimento di fibrille con diametro di circa 100 nm che si presentano distribuite in modo uniforme e omogeneo.

Anche in questo caso, la caratterizzazione del comportamento reologico dei materiali è stata sfruttata per cercare di stabilire delle correlazioni lavorazione-struttura-proprietà per i materiali investigati. In modo simile a quanto già descritto prima nel caso di compositi contenenti fibrille in PTFE, anche in questo caso la presenza delle fibrille all'interno della matrice rappresenta un ostacolo al rilassamento delle macromolecole di PP e, a causa di ciò, le curve dei moduli in funzione della frequenza per i compositi microfibrillari hanno una pendenza inferiore rispetto a quella mostrata dalla matrice pura, soprattutto alle basse frequenze. Infatti, gli andamenti di entrambi i moduli tendono a diventare indipendenti dalla frequenza a valori bassi di  $\omega$  e il comportamento reologico del materiale tende a diventare solid-like. Ciò a causa dell'amplificazione della componente elastica del comportamento viscoelastico tipico dei polimeri. Come mostra la Figura 4, infatti, maggiore è l'efficienza del processo di formazione delle fibrille, più elevato è il loro fattore di forma, maggiore è la loro influenza sulle proprietà reologiche del polimero.

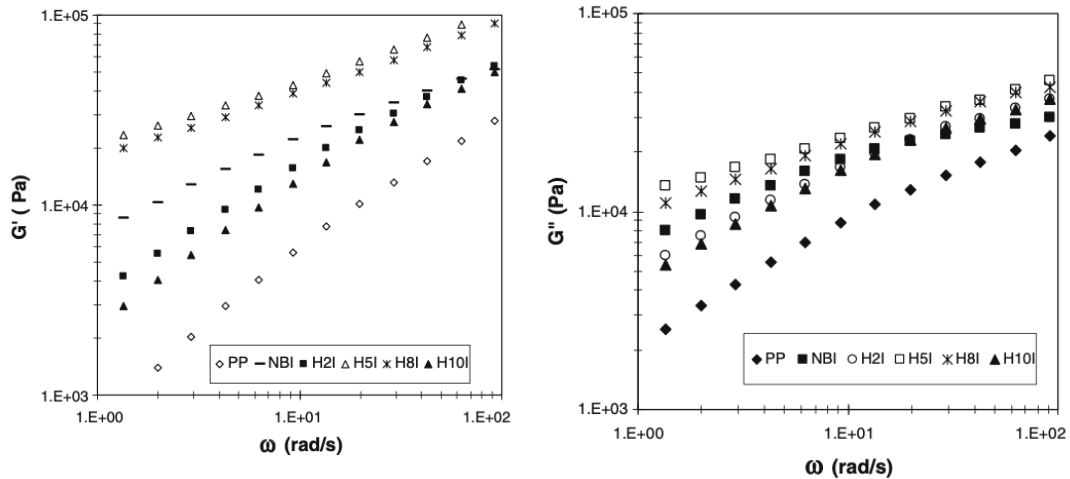


Figura 4. Proprietà reologiche per compositi PP/PET fibrillati.

Lo scopo principale della produzione di compositi “all-polymers” fibrillati è quello di ottenere un materiale finale avente proprietà superiori rispetto a quello della matrice pura. I lavori presenti in letteratura mostrano come l’impiego di un rinforzo polimerico in una matrice anch’essa polimerica, promuova l’ottenimento di notevoli miglioramenti da un punto di vista delle proprietà meccaniche, principalmente a causa della presenza di fibrille caratterizzate da un elevato grado di anisotropia e dell’ottima compatibilità tra i due componenti che promuove l’ottenimento di un’ottima adesione interfacciale. Si riportano di seguito due figure esemplificative, rappresentanti il tipico miglioramento tipicamente ottenuto per quanto riguarda le proprietà meccaniche della matrice conseguente alla creazione delle fibrille rinforzanti, nel caso di compositi contenenti fibrille in PET e in PLA.

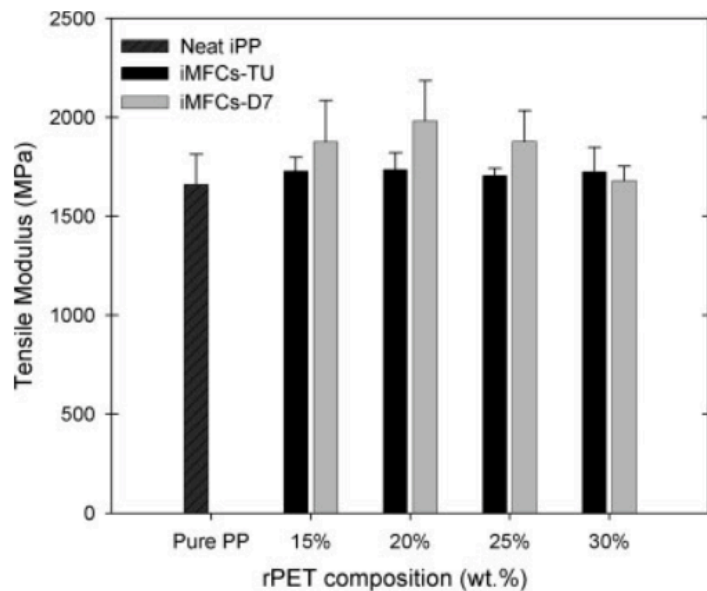


Figura 5. Miglioramento del modulo di trazione del PP in seguito alla creazione delle fibrille rinforzanti in PET.

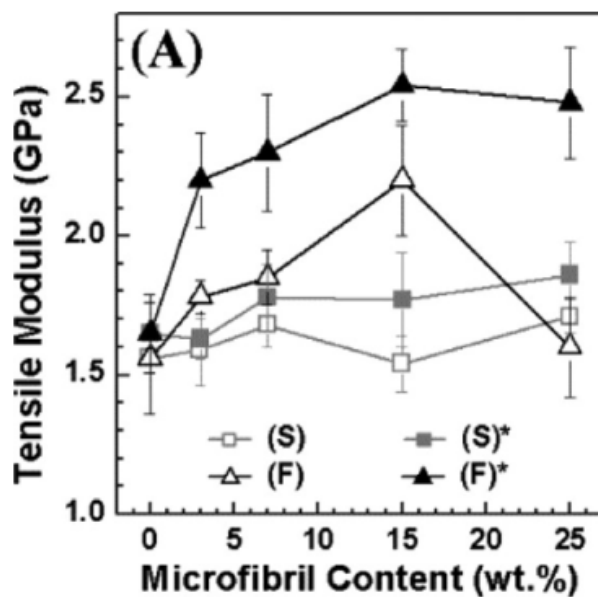


Figura 6. Miglioramento del modulo di trazione del PLA in seguito alla creazione delle fibrille rinforzanti in PA6 (curva nera con triangoli pieni).

Dopo aver esaminato i lavori presenti in letteratura sull'argomento, la seconda parte del presente lavoro ha riguardato la simulazione di un processo di estrusione di una miscela PP/PET e l'ottimizzazione delle condizioni di processo per indurre la fibrillazione in-situ delle particelle di fase dispersa.

A tale scopo, è stato preso in considerazione l'utilizzo di una polvere di PET proveniente da processi di riciclo meccanico e di un PP Moplen HP500N (LyondellBasell).

Poiché la ricerca delle condizioni di processo ottimali per ottenere compositi fibrillati è un processo che richiede tempo e provoca notevoli sprechi di materiale, la possibilità di utilizzare un software per poter simulare il processo e valutare tali parametri costituisce una risorsa estremamente utile.

Il software impiegato nell'ambito del presente lavoro per svolgere questa indagine si chiama Ludovic ed è un programma in grado di simulare le condizioni di flusso imposte al fuso polimerico durante un'operazione di estrusione. Per svolgere i calcoli ed i processi semplifica con modelli matematici la geometria del sistema ed i comportamenti termico e reologico del fuso all'interno dell'estrusore.

Il software consente di riprodurre un tradizionale estrusore partendo dalla costruzione del profilo vite desiderato. Per svolgere tale operazione, è sufficiente selezionare uno alla volta tutti gli elementi che si desidera comporgano la vite, scegliendoli tra i componenti presenti nel database del software.

In questo lavoro, l'estrusore usato è un bivate Leistritz ZSE 18HP di cui vengono riportati di seguito i due profili vite, quello reale e quello costruito con Ludovic.

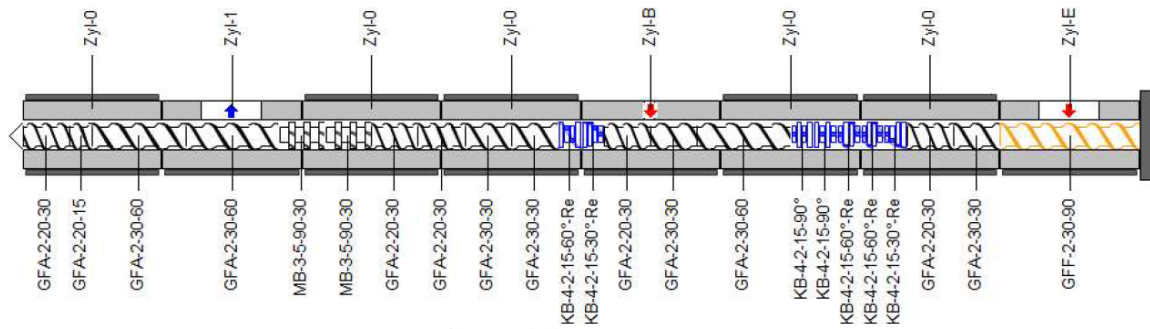


Figura 7. Profilo vite dell'estrusore Leistritz ZSE 18HP.

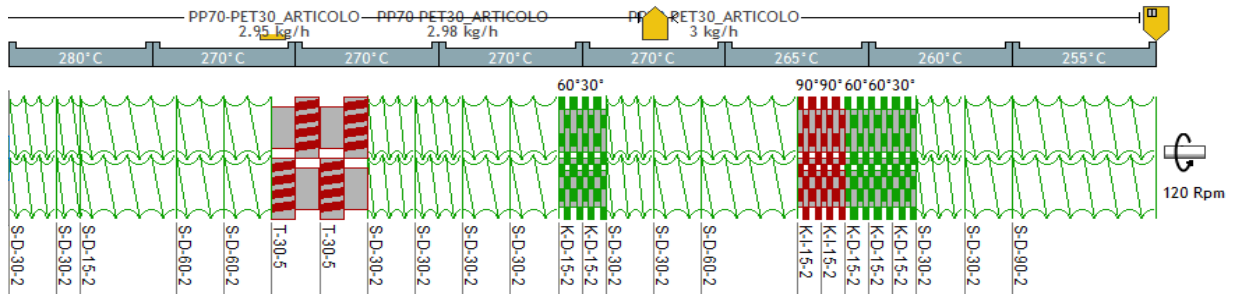


Figura 8. Profilo vite del Leistritz riprodotto con Ludovic software.

Affinché Ludovic sia in grado di simulare il processo, occorre fornire i dati relativi alle condizioni di processo desiderate e le proprietà termiche e reologiche dei materiali. A tale scopo, i materiali selezionati sono stati caratterizzati attraverso prove di calorimetria a scansione differenziale (DSC) e misure reologiche. In particolare, attraverso i test DSC si sono ricavati la temperatura di fusione dei materiali e la loro entalpia di fusione. L'analisi reologica è invece stata condotta al fine di ottenere le curve di variazione di viscosità dei materiali selezionati, a tre diversi valori di temperatura, che il software utilizza per poter simulare la viscosità del fuso polimerico nelle condizioni reali di estrusione.

Una volta inserite le specifiche del processo e dei materiali, ed aver costruito la ricetta di estrusione, viene avviata la simulazione, al termine della quale Ludovic restituisce informazioni riguardanti il consumo di energia, la distribuzione del tempo di residenza e una serie di altri parametri quali la temperatura, la viscosità e lo *shear rate* in funzione della distanza assiale rispetto alla filiera o rispetto al tempo. Nell'ambito di tale lavoro, mediante l'analisi dei grafici rappresentanti l'andamento di questi parametri, è stata verificata l'affidabilità di Ludovic e dei risultati da esso restituiti.

In un primo momento, si è provato ad impostare le simulazioni di modo che il PET (fase dispersa) rimanesse allo stato solido durante la lavorazione, e venisse deformato plasticamente all'interno della matrice fusa, seguendo quindi la prima strategia discussa precedentemente. Purtroppo, Ludovic non ha la possibilità di poter simulare il comportamento in estrusione di un materiale polimerico allo stato solido. Infatti, nelle impostazioni del software, un materiale può essere inserito come "carica" o come "prodotto": nel primo caso, Ludovic assume che il materiale rimanga solido indeformabile durante tutto il processo, mentre nel secondo è necessario che il materiale fonda per poter essere processato. Dunque, si è deciso di analizzare il metodo in cui entrambe le fasi (matrice e dispersa) si trovano allo stato fuso all'interno dell'estrusore e vengono miscelate durante processo di estrusione.

Una volta definito il sistema di interesse, nel caso del presente lavoro una miscela composta per il 70% in peso da PP e per il 30% in peso da PET, sono state lanciate sei simulazioni diverse, variando le condizioni operative di processo. L'obiettivo finale è in primo luogo verificare l'affidabilità dei risultati di Ludovic, e successivamente capire quali, tra i parametri variati, fossero quelli tali da garantire la formazione di fibrille.

Nelle prime quattro simulazioni si è mantenuto invariato il profilo di temperatura, selezionando diverse velocità di rotazione della vite, da 120 a 180, 200 e 250 rpm; nella quinta simulazione è stata modificata la composizione del sistema (90% in peso di PP e 10% in peso di PET) e nell'ultima è stato variato il profilo di temperatura.

I risultati ottenuti sono stati molto soddisfacenti. Innanzitutto, gli andamenti relativi alla temperatura, allo *shear rate* e alla viscosità in funzione della posizione assiale sulla vite hanno mostrato un aumento notevole di temperatura e *shear rate* in corrispondenza degli elementi di miscelazione e di masticazione, ed una conseguente diminuzione della viscosità del fuso a seguito dell'incremento delle altre due grandezze. Si riportano di seguito i risultati ottenuti nel caso della prima simulazione per mostrare quanto appena descritto (Figure 9-12).

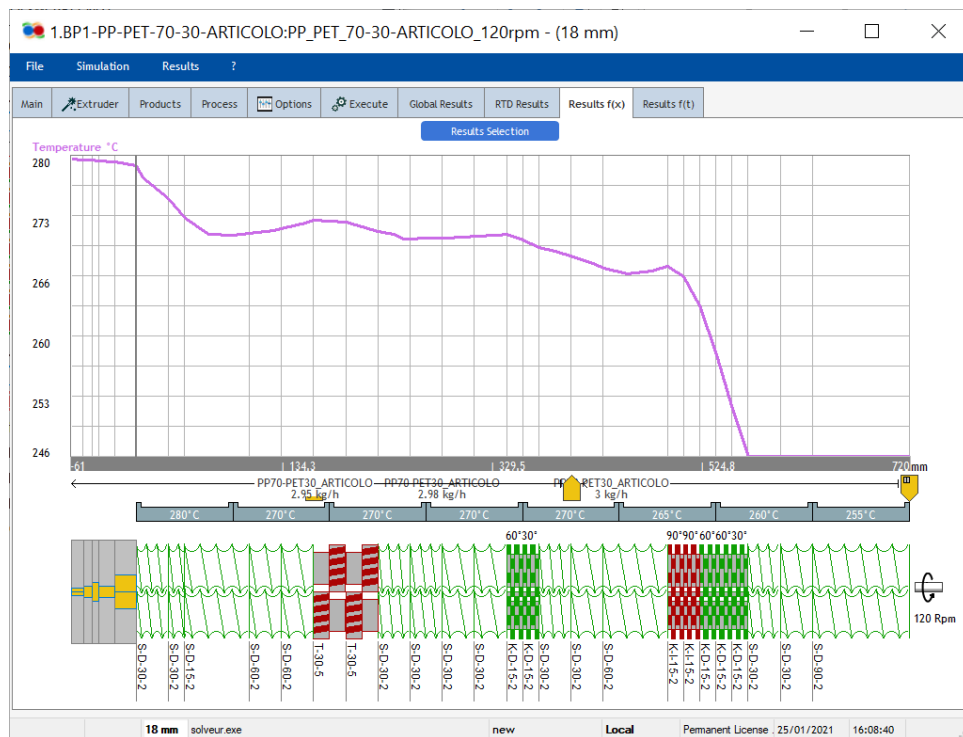


Figura 9. Andamento della temperatura riportato da Ludovic per il sistema 70% PP e 30% PET a 120 rpm.

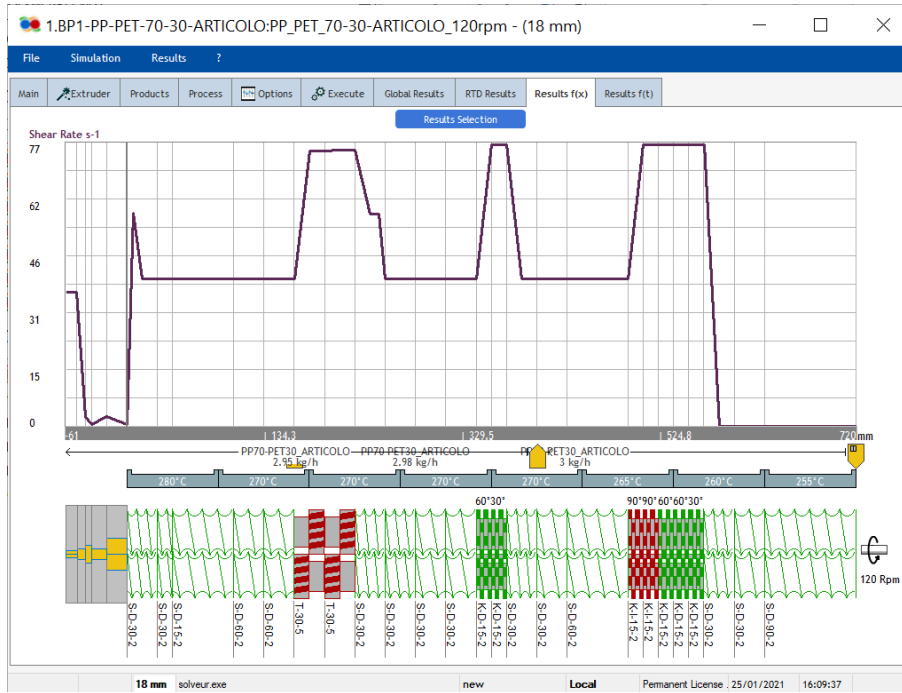


Figura 10. Andamento dello shear rate riportato da Ludovic per il sistema 70% PP e 30% PET a 120 rpm.

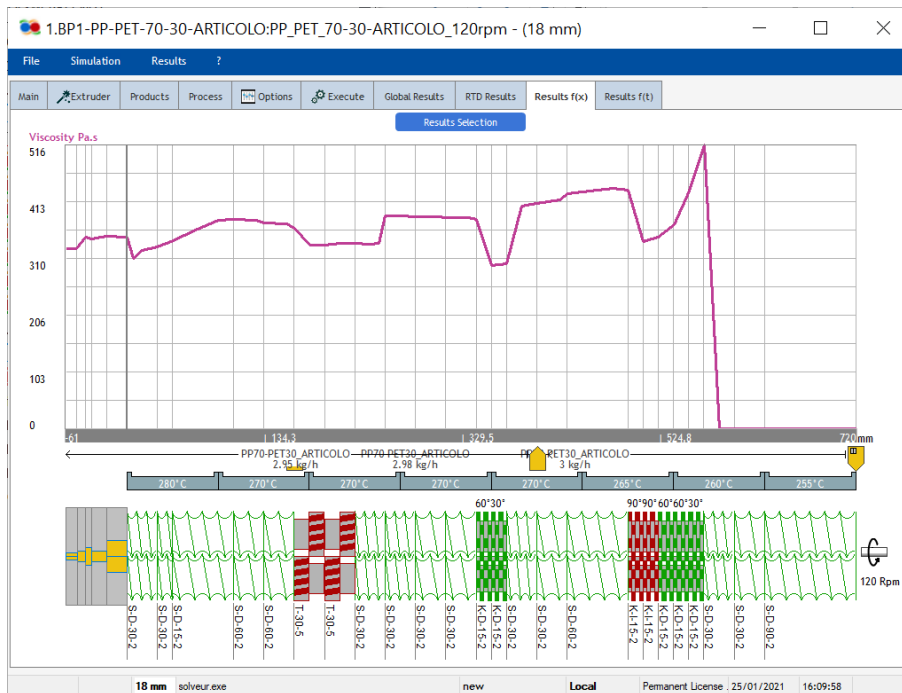


Figura 11. Andamento della viscosità riportato da Ludovic per il sistema 70% PP e 30% PET a 120 rpm

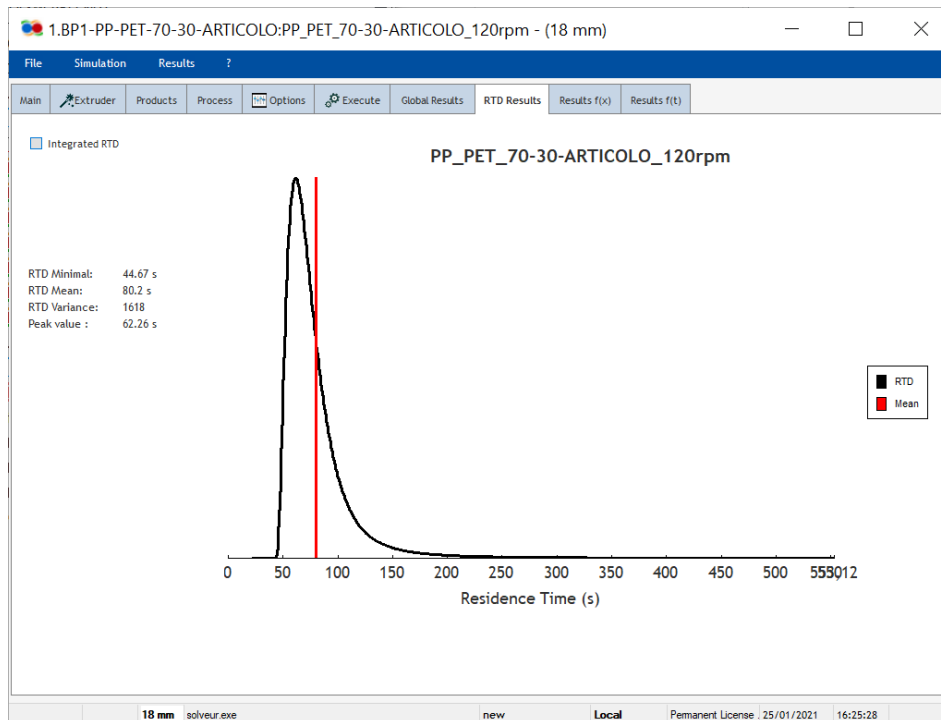


Figura 12. Andamento del tempo di residenza riportato da Ludovic per il sistema 70% PP e 30% PET a 120 rpm.

In seguito alla variazione della velocità di rotazione della vite da 120 a 250 rpm, il confronto tra le diverse curve ottenute ha nuovamente confermato l'attendibilità dei risultati ottenuti. Poiché lo *shear rate* è calcolato dal software prendendo in considerazione alcuni parametri geometrici dell'estrusore, risulta chiaro che, una volta definita la configurazione dello strumento, questo parametro dipenderà solo dalla variazione della velocità di rotazione. Aumentando lo *shear rate*, dunque, cresce anche l'energia dissipata, che provoca un aumento nei valori di temperatura riportati dei grafici corrispondenti. La viscosità, di conseguenza, risulta diminuita. L'aumento della velocità, poi, causa una diminuzione del tempo di residenza medio.

La modifica della composizione da quella iniziale a 90% di PP e 10% di PET, poi, non ha apportato nessuna modifica notevole ai grafici ottenuti per la temperatura e lo *shear rate*, mentre ha portato ad una importante diminuzione nella curva della viscosità. Anche questo fatto risulta in linea con quanto ci si aspettava, in quanto il 90% del blend è ora composto da PP, ovvero il materiale con la viscosità più bassa. Per questo stesso motivo, anche il tempo di residenza medio è leggermente inferiore.

La variazione del profilo di temperatura, da 255, 260, 265, 270, 270, 270, 270, 280°C a 260, 265, 270, 275, 280, 285, 290, 285°C, non ha giustamente apportato nessuna modifica all'andamento dello *shear rate*, in quanto questo parametro non dipende da T, mentre ha provocato una significativa diminuzione nella viscosità, come era atteso.

Appurata l'affidabilità di Ludovic, l'ultima parte del lavoro è stata dedicata allo studio dei parametri ottimali tra quelli impiegati nelle diverse simulazioni per ottenere una struttura fibrillare all'interno del sistema in esame.

In particolare, è noto come la forma finale assunta dalle particelle di fase dispersa dipenda dal rapporto esistente fra il numero di capillarità e il rapporto fra le viscosità della fase matrice e della fase dispersa. Per comprendere i parametri che influenzano il numero di capillarità e,

quindi, la morfologia generata all'interno delle miscele polimeriche, è necessaria una profonda comprensione delle condizioni di flusso a cui è sottoposta la miscela allo stato fuso. Diversi studi presenti in letteratura riguardanti la fluidodinamica dei processi di miscelazione fra due fluidi immiscibili aventi elevata viscosità hanno mostrato il differente effetto di diverse tipologie di flusso (shear o elongazionale) sulla deformazione delle particelle della fase dispersa (Figura 13). Durante il flusso, la variazione della geometria della fase dispersa dipenderà dal rapporto tra le forze idrodinamiche dettate dalla viscosità della fase che funge da matrice, e le forze di tensione interfacciale tra le fasi, che tendono a ripristinare la gocciolina a una forma sferica. Il suddetto rapporto è chiamato numero di capillarità, che in un campo di flusso di taglio dipende dallo shear rate, dalla viscosità della matrice, dalla tensione interfacciale fra le due fasi e dal raggio medio delle particelle di fase dispersa.

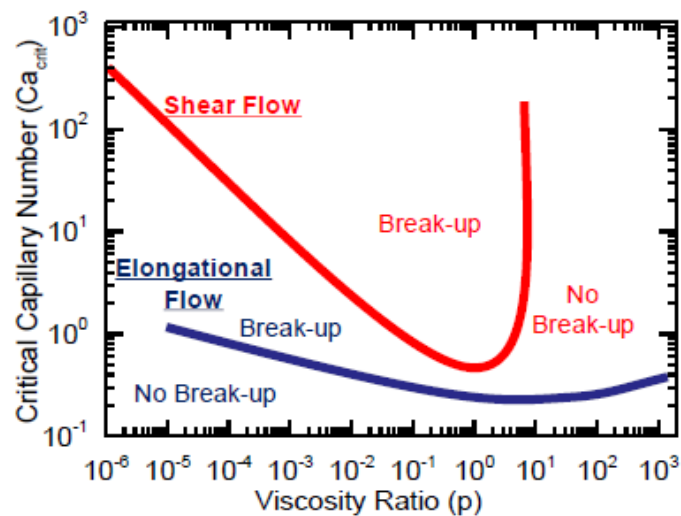


Figura 13. Influenza di diverse tipologie di flusso sulla geometria della fase dispersa, al variare del numero di capillarità e del rapporto di viscosità.

Dalla letteratura è emerso inoltre, che la forma e la geometria delle particelle di fase dispersa è influenzato in maniera significativa dal rapporto di viscosità tra la fase dispersa e la matrice (chiamato  $p$ ). Come visibile nella tabella riportata in Figura 14, valori molto bassi di tale parametro portano alla suddivisione della particella di fase dispersa in entità aventi dimensioni molto ridotte, promuovendo l'ottenimento di una morfologia molto uniforme. All'aumentare del parametro  $p$ , in particolare per valori compresi fra 0.1 e 1, risultano predominanti i fenomeni di Necking grazie al quale, da ogni particella di fase dispersa, se ne generano due gemelle aventi, quindi, dimensioni inferiori rispetto alla particella madre, e di End pitching. Secondo quest'ultimo meccanismo, la particella viene deformata in modo da produrre una geometria dumbbell che, se ulteriormente deformata, porta alla formazione di una particella aventi dimensioni maggiori e due ulteriori entità caratterizzate da dimensioni inferiori. Infine, per valori ancora più elevati del rapporto  $p$ , e in particolare per valori superiori ad un valore soglia pari a 3.8, non è possibile ottenere la rottura delle particelle sottoposte a flusso di shear; ciò implica che le particelle di fase dispersa possono, in questo specifico caso, deformate dal flusso di shear agente all'interno dell'estrusore, portando a particelle allungate aventi elevato fattore di forma.

| Viscosity Ratio ( $p$ ) | Break-up Mechanism   | Description  |
|-------------------------|--|--|
| Much lower 0.1          | Tip streaming<br>     | The break-up occurs at the tip of the deformed droplet and generally produce very fine droplets                    |
| $0.1 < p < 1$           | Necking<br>           | The deformed droplet breaks up into two daughter droplets.   |
|                         | End pinching<br>      | The deformation produces a dumbbell shape, after which the break-up occurs in the two droplets formed at the ends. |
| $1 < p < 3.8$           | Rayleigh break-up<br> | Interfacial instabilities produce disturbances that will break up the fibril into a line of droplets.              |
| $p > 3.8$               | No break-up<br>       | The break-up of the droplet under shear is not possible.   |

Figura 14. Meccanismi di deformazione e breakup legati al rapporto di viscosità  $p$ .

Poiché nel caso riportato nel presente lavoro si è interessati proprio a questa ultima condizione, le simulazioni già effettuate sono state ripetute sui polimeri puri, in modo da poter ottenere la variazione delle viscosità dei sistemi all'interno dell'estrusore, al variare delle condizioni di processo.

Una volta terminate le simulazioni, i dati relativi alla viscosità dei componenti sono stati rapportati in modo da ottenere il valore  $p$  per ogni set di parametri operativi impostati.

I valori ottenuti per i rapporti di viscosità  $p$  nelle diverse simulazioni, al variare della velocità di rotazione della vite e del profilo di temperatura sono stati riportati su grafici in funzione della coordinata assiale funzione della posizione lungo la vite (Figura 15-Figura 16).

Come si evince dal grafico riportato in Figura 15, le condizioni operative selezionate permettono in ogni caso l'ottenimento di valori di  $p$  superiori a 3.8, indicando la formazione di strutture fibrillari in seno alla fase PET. Andando a valutare l'influenza della velocità di rotazione della vite su tale parametro, si nota come il rapporto fra le viscosità delle due fasi diminuisce all'aumentare della velocità di rotazione, portando all'ottenimento di valori molto prossimi al valore soglia di 3.8 per il più elevato valore di rpm testato. Per lo scopo di tale lavoro, la scelta ottimale risulta essere 120 rpm, cioè il valore minimo tra quelli impostati che garantisce l'ottenimento di valori di  $p$  più elevati, corrispondenti ad una maggiore efficienza nel meccanismo di deformazione delle particelle di fase dispersa.

Il risultato ottenuto si spiega considerando che tempi di residenza più lunghi derivanti da minori velocità di rotazione promuovono la formazione delle fibrille più sottili e resistenti [1]. Va comunque specificato che anche 180 e 200 rpm sono velocità di rotazione che sembrano garantire la conformazione desiderata della fase dispersa. Soltanto a 250 rpm il rapporto tra le viscosità presenta in alcuni punti un valore inferiore a 3,8, motive per cui questo non risulta essere un valore ideale di velocità a cui lavorare il blend polimerico.

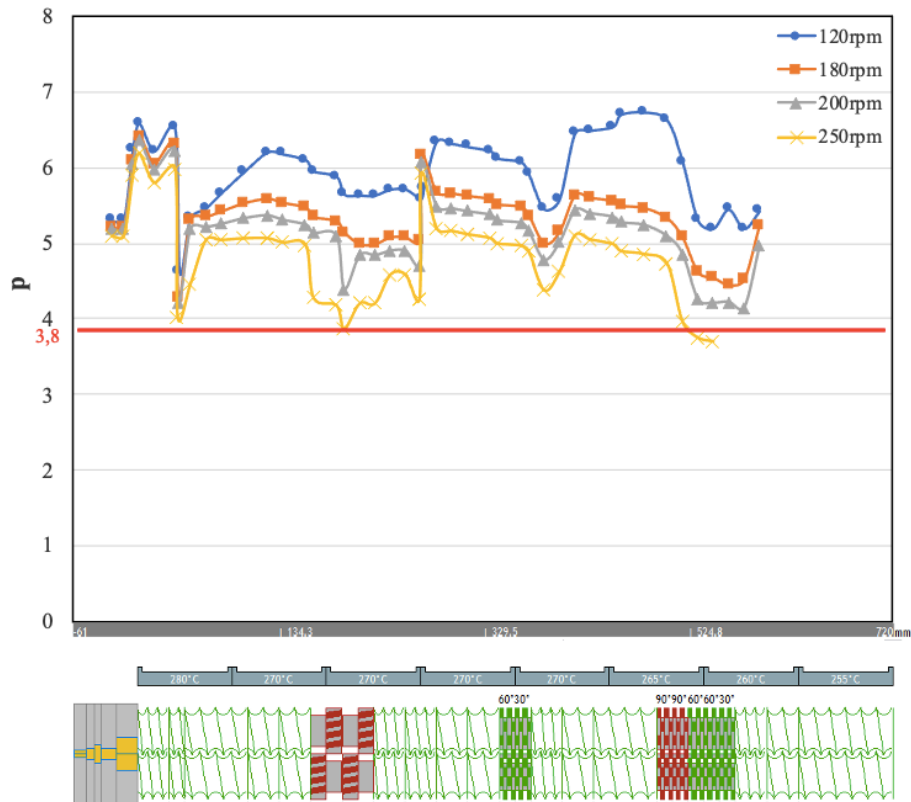


Figura 15. Rapporto di viscosità  $p$  in funzione del profilo vite al variare della velocità di rotazione.

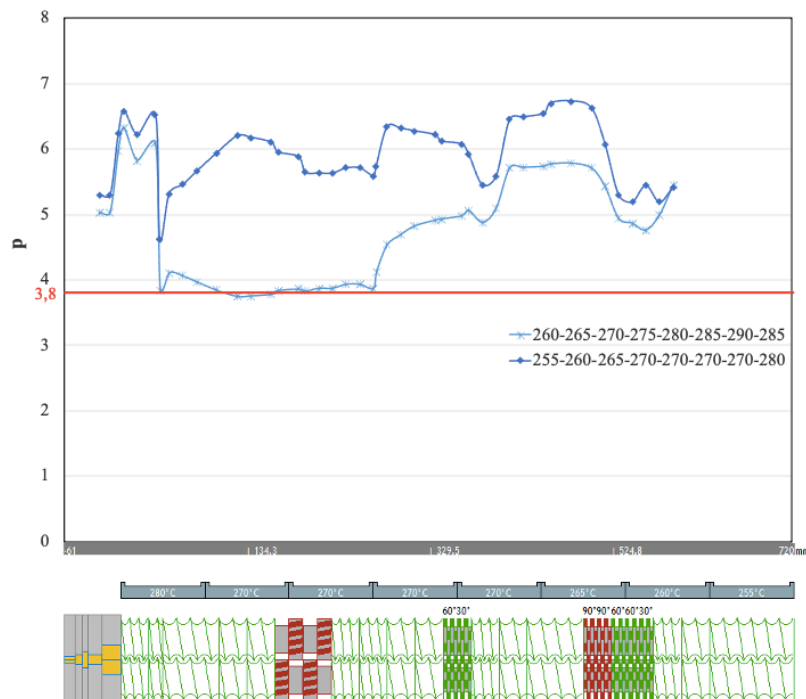


Figura 16. Rapporto di viscosità  $p$  in funzione del profilo vite al variare del profilo di temperatura.

Per quanto riguarda il confronto tra i due profili di temperatura, invece, si può concludere che la migliore performance è quella ottenuta applicando il primo profilo di temperatura, che

corrisponde alla curva blu in Figura 16. Infatti, quando si imposta il secondo profilo, leggermente più alto, il rapporto di viscosità subisce una notevole diminuzione fino a valori molto vicini a 3,8 e, in alcuni casi, inferiore. A più alte temperature, d'altronde, è noto che la viscosità diminuisca e, nel sistema in esame, questo andamento è notevolmente più marcato nel caso del PET. Come si evince dal grafico in Figura 17, infatti, la curva della viscosità nel caso del PET diminuisce in maniera molto marcata in seguito all'aumento della temperatura. Per queste ragioni, risulta chiaro che la scelta più conveniente per processare il blend in esame sia l'utilizzo del primo profilo di temperatura, ovvero 255, 260, 265, 270, 270, 270, 270, 280°C.

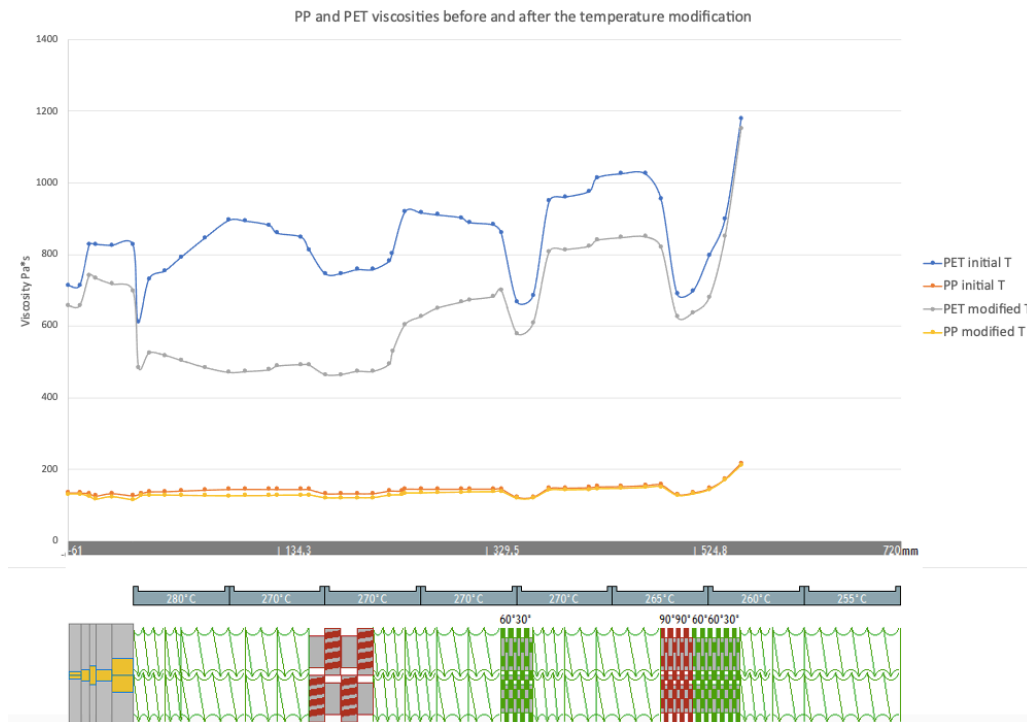


Figura 17. Variazione delle viscosità di PP e PET puri in seguito al cambio del profilo di temperatura.

## 1. Introduction

Nowadays, the continuous increase of production and consumption of plastics has become a relevant environmental problem because of the big amount of plastic waste generated.

An interesting solution to this issue is the recycling and reuse of the waste plastic materials instead of their disposal carried out by incineration. [2]

In this sense, blending of different immiscible semi-crystalline thermoplastic polymers is attracting an increasing attention in order to produce a relatively new kind of materials: all-polymer microfibrillar (or nanofibrillar) composites.

As the more traditional polymer blends, also the fibrillar composites are industrially realized with extrusion processes and, more often, with the use of twin-screw extruders. What is more difficult to achieve, especially in this case where the creation of the fibrils require particular conditions, is the correct definition of all the needed parameters, like screw configuration, screw speed rotation, screw temperature profile, each material's concentration and so on. Searching the perfect conditions with laboratory experiments can result to be very expensive and time consuming because many tests may be necessary before reaching the expected results. Very useful tools to limit this kind of problems are softwares able to accurately reproduce the extrusion process, like Ludovic software, the one employed by us to execute the simulations.

Due to the fact that the production of all-polymer fibrillar composites is a fairly new process in the field of polymer blends, the present work begins with a detailed analysis of the already existing systems of this kind present in literature. Particular attention has been paid to identifying the characteristics for which these materials result to be improved with respect to the initial ones, and these are mechanical and rheological properties above all.

As it has emerged from the analysed papers, these materials are mainly produced with a three-steps process that starts with the extrusion. The aim of this work is then simulating with Ludovic software this step of the production and verifying the reliability of the obtained results as well as finding the best conditions that, at the end of the whole process, will lead to the formation of the expected fibrillar materials.

To reach this objective, an insight in the principles governing Ludovic is necessary.

Therefore, the subsequent chapter is dedicated to the analysis of the mechanisms that the software follows in its functioning, from the theoretical mathematical principles to the more practical way in which the simulations must be organized and set. A detailed description of all the parameters that need to be defined is then provided.

In the present case, the chosen system on which the simulations have been carried out is composed by a PP matrix in which a reinforcing PET phase has been added. It is worth underlining the fact that the PET derives from the mechanical recycling of bottles, to demonstrate the effective importance of this new kind of materials. This system has been tested also after the variation of the screw speed rotation, profile temperature and melt's composition.

Finally, after the definition of all the parameters and the used materials, a detailed comment of the obtained results is presented in the final chapter. In particular, it is subdivided into two sections: the first one is dedicated to the examination of the temperature, shear rate, viscosity and residence time graphical results, in order to assess Ludovic's reliability in defining the optimal process parameters, while the second and last section presents a comparison between the results obtained after the parameters variation mentioned above.

## 1.1 Description of fibrillar composites and production process

Fibrillar composites are an example of all-polymer materials, they are made of an isotropic thermoplastic matrix reinforced by a dispersed phase constituted by another thermoplastic material. Using a polymer reinforce in a polymer matrix brings very notable improvements from the point of view of the mechanical properties, light weight and, above all, good compatibility among the two materials. Furthermore, the peculiarity of these composites with respect to the traditional ones, is that the reinforcing phase is created directly *in-situ* during the processing. [3].

The fibrils have a diameter of 50-150 nm if the resulting material is a nanofibrillar composite [4] and a diameter of 1-10  $\mu\text{m}$  in the case of MFC [3] [5].

This new type of composites offers several advantages which make it very interesting:

- There is no aggregation of the reinforcing particles, which means that their distribution is nearly perfect. This is very important because the increased surface area obtained produces an improvement of the final material's properties, such as tensile strength and Young's modulus. Furthermore, it is something difficult to control in the traditional processing techniques (because the shear force usually is not big enough to overcome the high viscosities of the molten polymers, and so the dispersion of nanoparticles is quite heterogeneous). [4] [6]
- The fibrils' high aspect ratio, which reaches values up to 7000, allows them to form an entangled network within the matrix which causes the increase of its melt strength and an easier processability. [4] [6]
- There is no need to add mineral additives nor extra-compatibilizers. [4]
- The process of production (presented in the following paragraph) is economic and eco-friendly. The obtained materials are lighter, cheaper and simpler to produce if compared to the traditional ones. [6]
- It is a very good option for recyclability of plastics waste. [4]

There are two possible ways to obtain a fibrillar composite: the first one is characterized by a processing temperature that is lower than the reinforcing material's  $T_m$ . In this case, then, the reinforcing phase is coupled with the matrix remaining in the solid state and the composite is generated through the shearing of the matrix where the crystalline reinforcing particles are dispersed. A critical value of shear stress must be reached in order to obtain the deformation of the reinforcing phase [1]. In literature, this process has been applied only to PTFE reinforcing particles. PTFE, in fact, has high crystallinity and low density of chain entanglements in its amorphous phase, which make it very suitable for this purpose. Only the compounding process at a temperature below the PTFE's  $T_m$ , in this case, is sufficient to obtain a plastic deformation of the dispersed phase, that is subjected to fibrillation inside the molten matrix subjected to shear stress. The obtained fibrils are so thin that they undergo an entangling process during mixing, which results into the formation inside the matrix of an entangled network with a very high reinforcing ability [7].

During a first attempt, also in our work the PET was meant to be added in the solid state to a molten PP matrix, but no ways have been found with Ludovic software to simulate the fibrillar deformation of this material. In fact, from the settings, it could have been inserted either as a solid "filler", and hence, according to the software's functioning, it would have remained solid during the whole process, or as another "material", and therefore it had to undergo a melting step in order to be processed by Ludovic.

So, it has been decided to simulate the second possible way to obtain a fibrillar composite: the melt blending of two polymeric materials. According to this method, both the materials inside

the extruder reach their melting temperatures and the fibrils are obtained deforming the reinforcing material drops. In this case, great attention must be paid when choosing the processing conditions because, as it will be explained in the last chapter, only with specific values of viscosity ratio (PET viscosity to PP viscosity), screw speed rotation and screw temperature profile, the fibrillation can be obtained. In the present work, Ludovic software has been used to understand which extrusion conditions were the ones more likely to bring the material to fibrillation, but it must be underlined that some further stretching steps are necessary in order to consolidate the final morphology. In literature, the process mainly applied to obtain the fibrillar composites is constituted by three steps [3] [4] [8] (Figure 18):

4) Mixing Step

The two materials are melt-blended in an extruder. An important aspect to take into account during this process is that the difference in the melting temperature of the two materials used must be of at least 40 °C.

5) Fibrillation Step

This is the step in which the two components obtain a reciprocal good orientation by cold drawing or cold/hot stretching.

6) Isotropization Step

The obtained material is subjected to a thermal treatment. The temperature at which it is carried out must be intermediate between the melting temperatures of the two components. The machine used is an injection or compression molder.

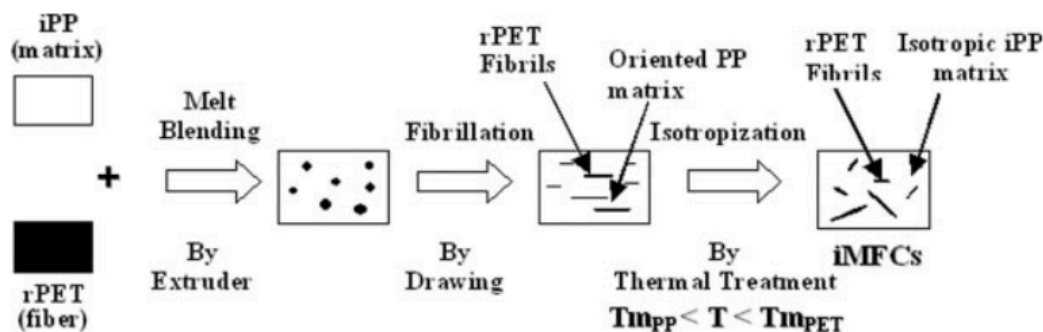


Figure 18. Production process of melt-blended all-composite materials.

## 1.2 Fibrils in PET

Polyethyleneterephthalate (PET) is among the most commonly used thermoplastic to produce reinforcing fibrils in all-polymer composites. Several studies in literature report the preparation of PET-containing all composites and their characterization. In the following, a brief overview about the most significant results will be presented.

**Fakirov et al.** [4] used the process described above to produce polymeric nanofibrillar composites. In particular, they produced a composite material made of a polypropylene (PP) matrix (80% wt) with fibrils of PET (20%wt) as reinforcement. The two polymers were melt-blended in a twin-screw extruder at 30 rpm and with a temperature profile of 260-270-260-245°C (starting from the feeding zone), and then cooled down at room temperature. At the

end of this procedure, a further amount of PP has been added to the obtained blend, so that the final amount of PET became 16,7% wt.

The blend was then submitted to the drawing process at 130 °C in order to obtain filaments of 30 µm. Finally, these filaments were knitted together to produce a sheet and then compression moulded in a hot press at 180°C and at a pressure of 650 kPa.

Figure 19 shows the samples after blending and spinning (a), after knitting (b) and in the last two pictures SEM images at different magnifications of the final compression moulded composite are reported. It is important to underline the fact that it becomes a composite material only after the thermal treatment, taking place during the compression moulding step, at a temperature between the  $T_m$  of the two materials (here 170°C for PP and 250°C for PET), otherwise it is a blend. In fact, it is only after the compression moulding that the component with the lower melting temperature becomes an isotropic matrix with its reinforcement, as shown in Figure 19c and 2d.

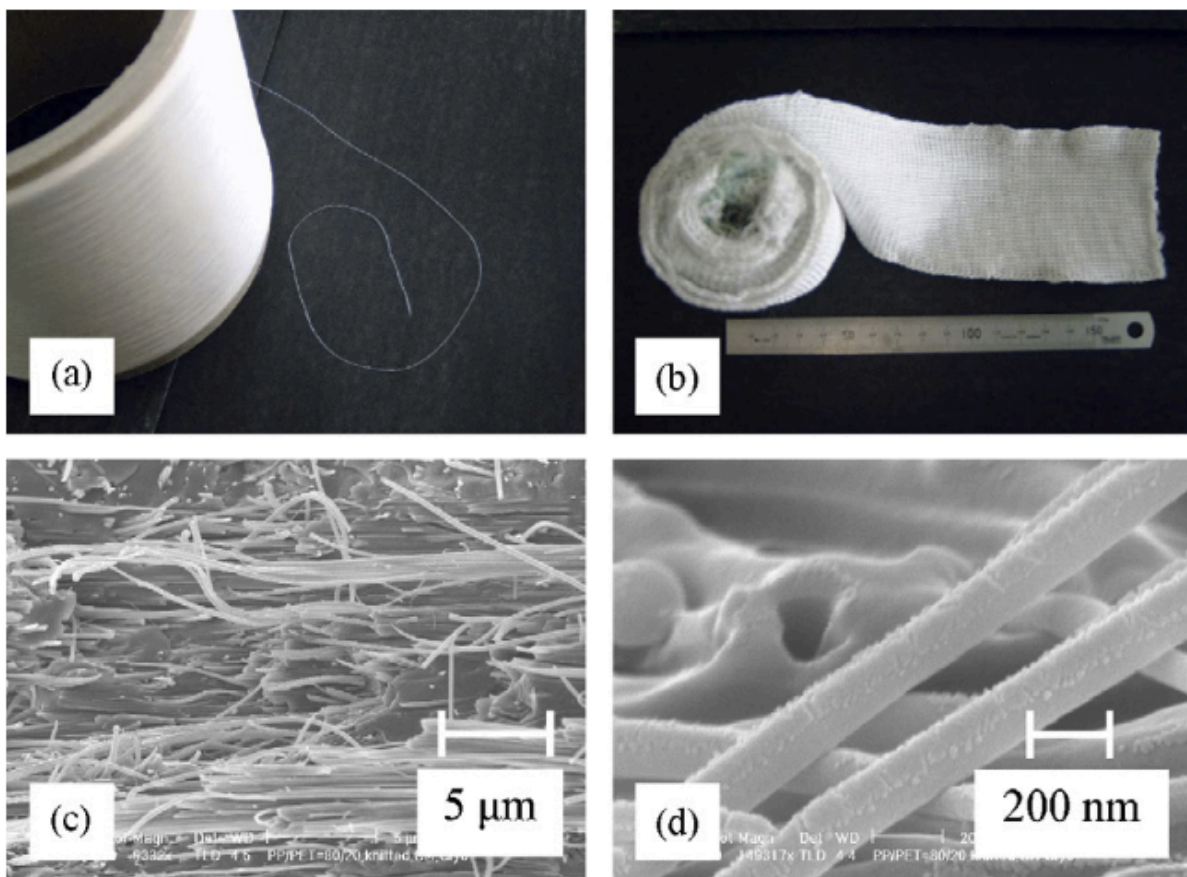


Figure 19. Blended and spun (a), knitted (b) samples and SEM images of the compression molded composite.

As mentioned before, SEM characterization was carried out, as well as Wide-Angle X-Ray Scattering analysis (WAXS) to gain information about the initial, intermediate and final orientation and crystallization of the fibrils.

From the SEM images in Figure 19 (c and d), fibrils with diameter of about 100 nm are observed and it is noteworthy the fact that the fibrils are very well distributed without aggregates. This is one of the greatest advantages of this kind of composites. Moreover, the fibrils are disposed perpendicularly to each other, according to the knitting process.

Another key aspect to consider about all-polymer composites is the aspect ratio, the ratio between the length of a fibril and its diameter. In the case of NFCs, it reaches values up to 7000, which are incredibly high.

From the WAXS analysis, the following results are obtained (Figure 20).

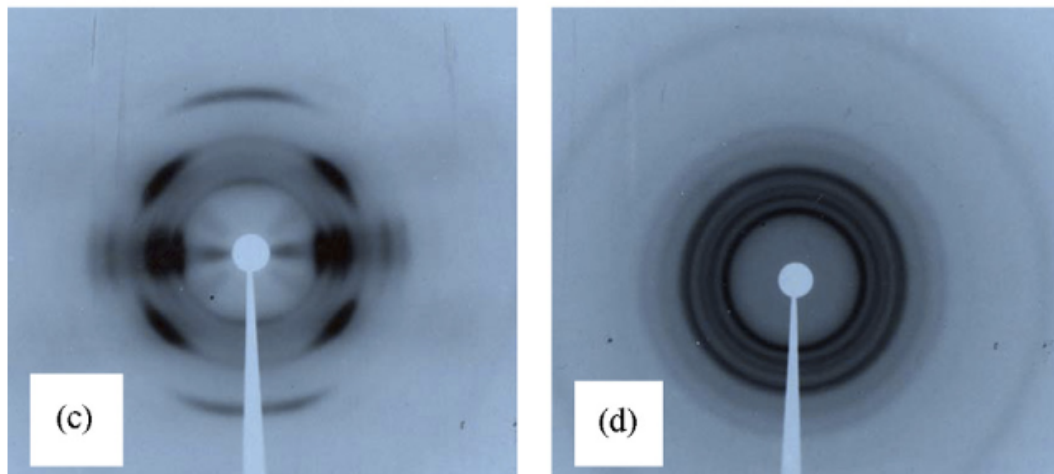


Figure 20. WAXS analysis of the PP/PET spun filament.

On the left side of the picture (c) it is reported the WAXS pattern of the spun filament of PP/PET, while on the right side (d) there is the knitted and compression molded filament, which has undergone an annealing process at 145°C. The comparison between the two patterns shows that the spun filament presented perfectly uniaxial orientation that disappeared after the sample was subjected to compression molding. This finding is attributed to the strong isotropization of the PP induced by the compression molding, as demonstrated by the isotensity circles and the absence of a preferential orientation in the right side of Figure 4. Another phenomenon to be noticed is that there are no precise reflections that come out from PET and this can be due to three possible phenomena:

- There is much more PP than PET in the composite material (83,3% of PP vs 16,7% of PET).
- PP crystallizes much more than PET, which instead is the main component of the amorphous phase.
- The reflections coming out of the crystalline phase of PET are in the same position as those of PP but are weaker, so those of the matrix cover them.

As far as the mechanical properties are concerned, a significant improvement is expected with respect to the neat PP, because of the high aspect ratio of the fibrils. In this case, because of an error during the measure the result is not as high as expected but is significant anyway, as shown in the following images (Figure 21). The first one reports the tensile strength and the second the tensile modulus. The increase in both cases is of about 35%.

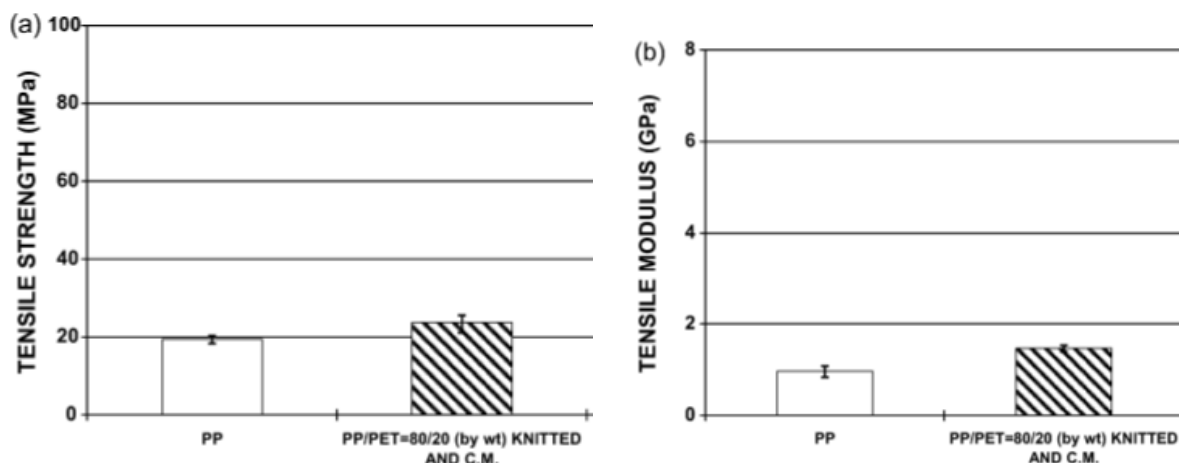


Figure 21. Tensile strength and tensile modulus of neat PP and PP/PET knitted and compression molded samples

Finally, an interesting point is highlighted in this article and is the possibility of isolating the neat nanofibrils from the polymer blend which can be used for different purposes. This result can be obtained thanks to a solvent (xylene in this case) applied before or after the compression molding, to remove the matrix. The SEM images below (Figure 22) show the aspect of the knitted fibrils once they are separated from the PP matrix, at different magnifications.

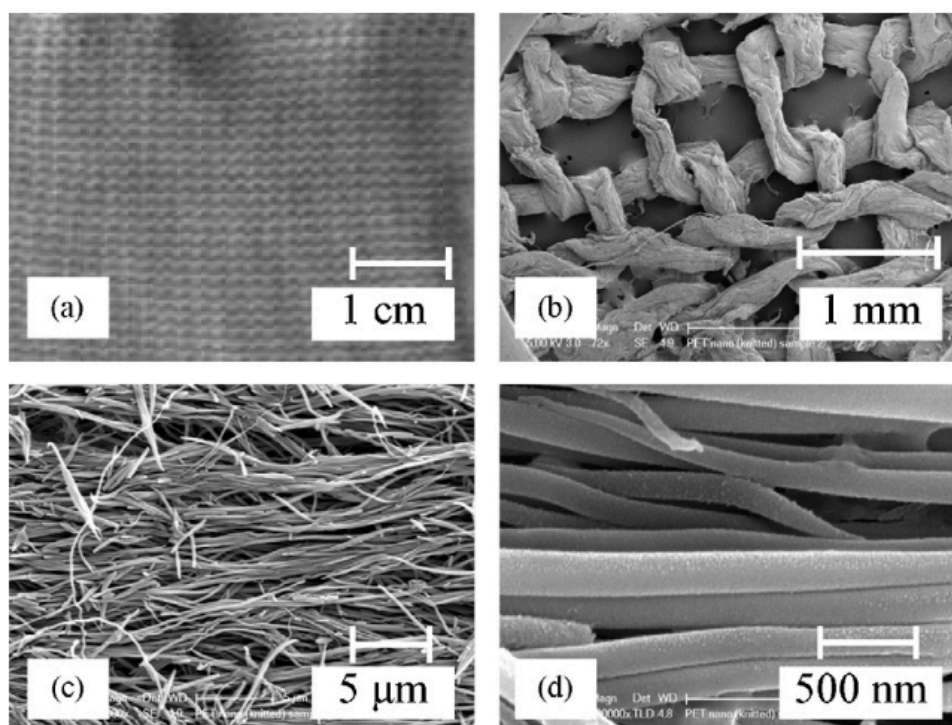


Figure 22. SEM images of knitted fibrils without matrix, at different magnifications.

The possible applications for these microfibrillar materials are several and vary from gas or liquid nanofilters to the much more promising biomedical field. In fact, there is great need for scaffold materials in the tissue engineering and these fibrils could be a promising option if one considers that the efficiency of a scaffold basically depends on the surface of its material. A further application for which the nanofibrillar composites are being investigated is the creation of carriers for the drug delivery. In order to be suitable for this purpose, fibrils should

have a rough or porous surface to be able to carry as much drug as possible, but what makes them very interesting is their small diameter and vast surface area.

**Another research that concerns all-polymer composites made of PP matrix and PET reinforcing fibrils was conducted by Jayanarayanan et al. [3]**

In their work, they focused on the dynamic rheology of composites with microfibrillar reinforcement at different draw ratios. In particular, they studied how the modification of the draw ratio during cold drawing could influence the morphology development of PP/PET blend at the specific composition of PP 85% wt and PET 15% wt. They took into consideration a traditional PP/PET blend, a microfibrillar blend and the corresponding microfibrillar composite.

To produce the material, the dried PET is kept at 100°C for 12 hours. They mixed it with the isotactic PP and melt-blended the resulting mixture in a single screw extruder at the temperatures of 225, 235, 250, 255, 260°C. After that, the resulting material was cooled down in a water bath and then moved to a hot air oven maintained at 100°C, as shown in Figure 23.

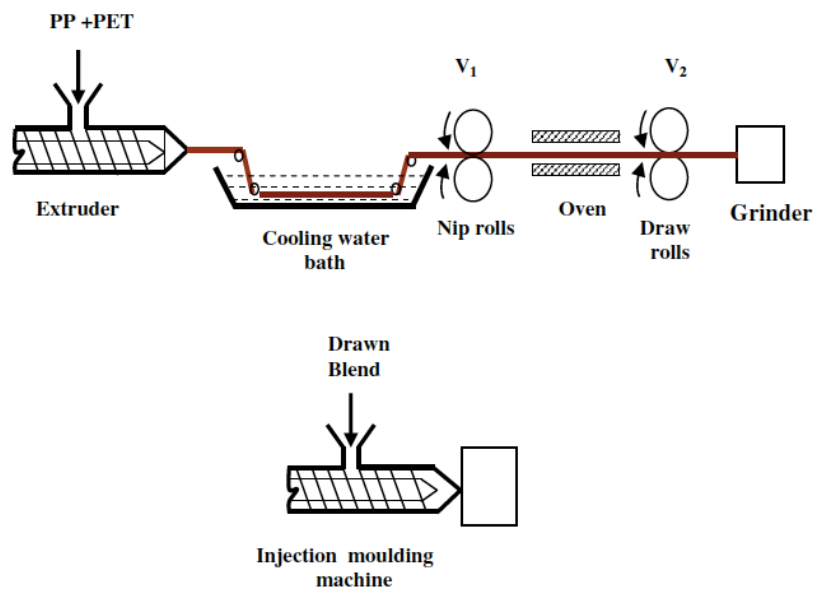


Figure 23. Scheme of the production process of MFCs

The two sets of rolls with ratio of speed given by the formula

$$\text{Ratio of speed} = \frac{V_2}{V_1}$$

imparted to the melt blended material the different draw ratios desired by the authors, obtained varying the ratio of speed. The draw ratio is defined as the ratio between the cross-section areas of the drawn samples and the die. More in detail, the draw ratios were 1 (in the case of neat blend NB), 2, 5, 8 and 10.

The NB, after extrusion, underwent the injection molding with a temperature profile of 185, 225, 245 and 270 °C, while the other drawn samples with a temperature profile of 160, 170, 190 and 205 °C. The specimens were then called NBI, H2I, H5I, H8I and H10I, symbols that indicate the different draw ratios used and the fact that they went through injection molding.

After this process, the samples' morphology was tested using SEM analysis at a 20kV acceleration voltage, removing PP phase with hot xylene to better detect PET fibrils, or removing PET with tetra-chloroethane to investigate PP.

The thermal analysis was conducted using a DSC at a heating and cooling rate of 5°C/min. The specimens were heated up to 200°C, held there for 3 minutes and then cooled down to room temperature. PP, NBI and MFCs' tensile properties were measured following the ASTM D-638 standard method using the injection molded samples at a constant speed of 50 mm/min. They reported the mean value of the five tested specimens.

Finally, dynamic rheological properties, such as dynamic complex viscosity  $\eta^*$ , storage and loss moduli  $G'$  and  $G''$ , mechanical loss factor  $\tan\delta$  in function of angular frequency  $\omega$ , were investigated using a rotational rheometer with a 35 mm diameter parallel plate sensor, varying from 0,6 to 100 rad/s at 205°C.

From the SEM analysis emerged that the extruded blends were isotropic but in both the phases the fibrils were highly oriented after drawing. The neat blend samples obtained at draw ratio 1, after extrusion and drawing, showed a spherical PET particles dispersion in a continuous matrix made of PP, as reported in the image below (Figure 24).

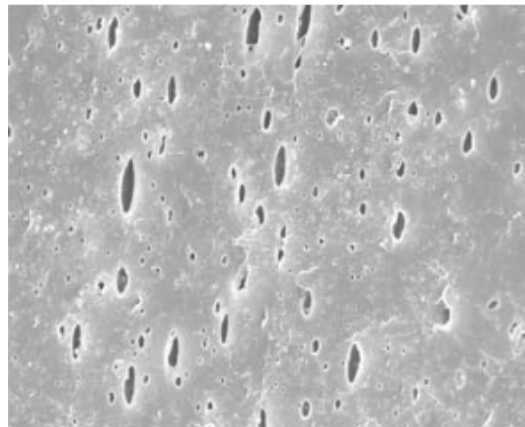


Figure 24. SEM image of neat blend

Instead, the samples obtained at different draw ratios (2, 5, 8 and 10) revealed the presence of PET fibrils in the PP matrix, both of the phases oriented by the drawing process, probably because of the elongational flow.

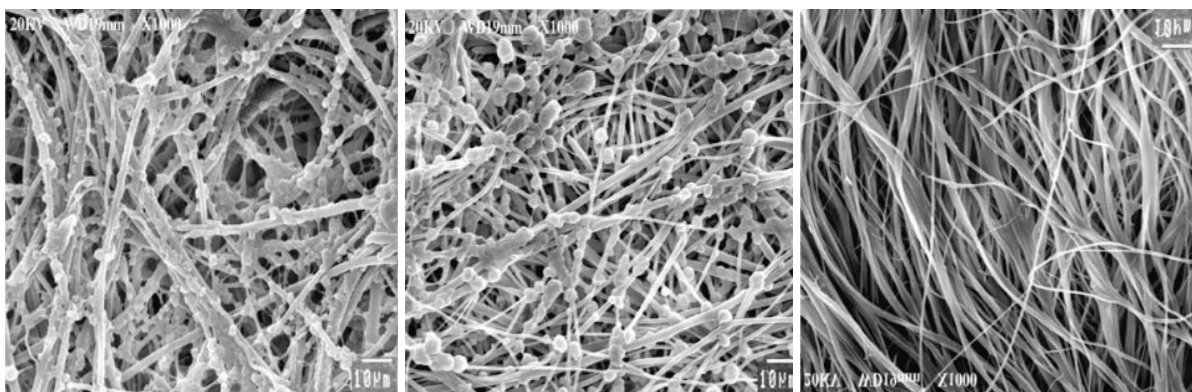


Figure 25. SEM images of PET fibrils at draw ratio 2, 5 and 8 respectively, in the same order of the pictures.

As shown by the images above, the fibrils changed their mean diameter according to the draw ratio they underwent. In particular, it can be said the mean diameter decreased with the decreasing of the draw ratio (8,6  $\mu\text{m}$  for specimens H2, 4,9  $\mu\text{m}$  for H5 and 4,1  $\mu\text{m}$  H8), but

there is an exception for the case with draw ratio of 10. In this situation, in fact, it grew up to 6,9  $\mu\text{m}$  and this is due to the presence of large fibrils (Figure 26). Furthermore, there are studies that show that, in presence of very high draw ratios, the elongated drops break up and their aspect ratio is significantly reduced because they can't bear the extensional stress, and that is why in this image some of the fibrils are broken.

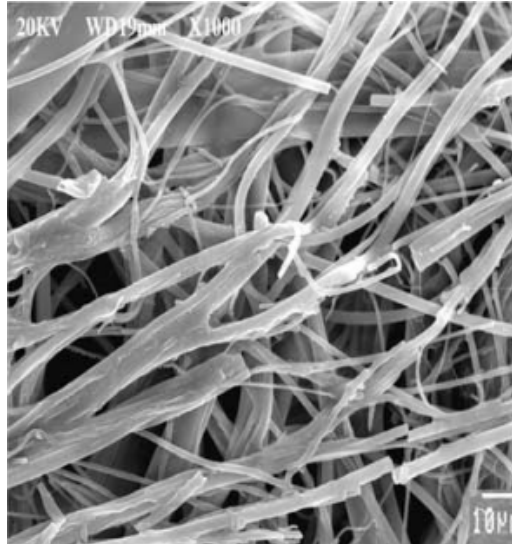


Figure 26. SEM image of the PET fibrils obtained at draw ratio 10.

Only after the injection molding the orientation of the two phases was modified, in particular the PET fibrils became randomly distributed in the PP matrix. What happened is that the process of injection molding, conducted at a temperature between the  $T_m$  of the two materials, brought to the melting and consequent loss of orientation of the PP matrix, while it left unmodified the fibrillar morphology of PET. But another thing to take into account is the fact that during injection molding, the reinforcing PET was subjected to a temperature that was quite higher than its  $T_g$  and this phenomenon led to the creation of fibrils with an irregular diameter along their length if compared to the drawn samples.

In addition, another SEM analysis was carried out on the samples after injection molding. As expected, in the case of neat blend there are not fibrils because of the molding temperature.

As far as the thermal properties are concerned, the melting and crystallization behaviors of PP, neat blend, H2, H5, H8 and H10 blend were investigated. It has been observed that the melting temperature of PP decreased varying from pure PP (167,7  $^{\circ}\text{C}$ ), NB (167,6  $^{\circ}\text{C}$ ), PP phase in H2 (165,3  $^{\circ}\text{C}$ ), in H5 (166,3  $^{\circ}\text{C}$ ), in H8 (166,3  $^{\circ}\text{C}$ ) and in H10 (164,7  $^{\circ}\text{C}$ ). This phenomenon indicates how the presence of the PET reinforcing fibrils reduced the PP's capability of creating perfect crystals, compared to the pure PP or the neat blend.

Another aspect that was investigated was the fact that PET fibrils bring the crystallization temperature of PP to noticeably higher values, moving from 114  $^{\circ}\text{C}$  for pure PP to 121  $^{\circ}\text{C}$  for NB, 122  $^{\circ}\text{C}$  for PP in H2, 122,7  $^{\circ}\text{C}$  and 122,6  $^{\circ}\text{C}$  for H5 and H8 and 120,8  $^{\circ}\text{C}$  for H10.

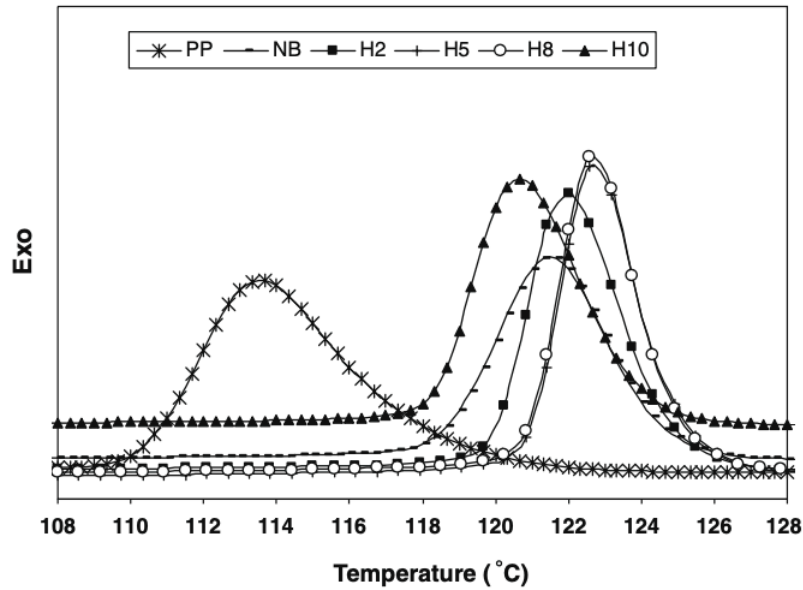


Figure 27. DSC curves showing the different crystallization peaks.

The highest values are reached with H5 and H8, while H10 has a lower temperature of crystallization because higher aspect ratios often cause the breakup of the fibrils thus reducing its capability of influencing crystallization (Figure 27). In addition, it was understood that the presence of PET microfibrils acted as an ideal site of nucleation of PP crystals, which is something that can be translated into a general positive effect of the length of fibrils on the crystallinity of the continuous phase.

Regarding the tensile properties, the obtained curves are reported in Figure 28.

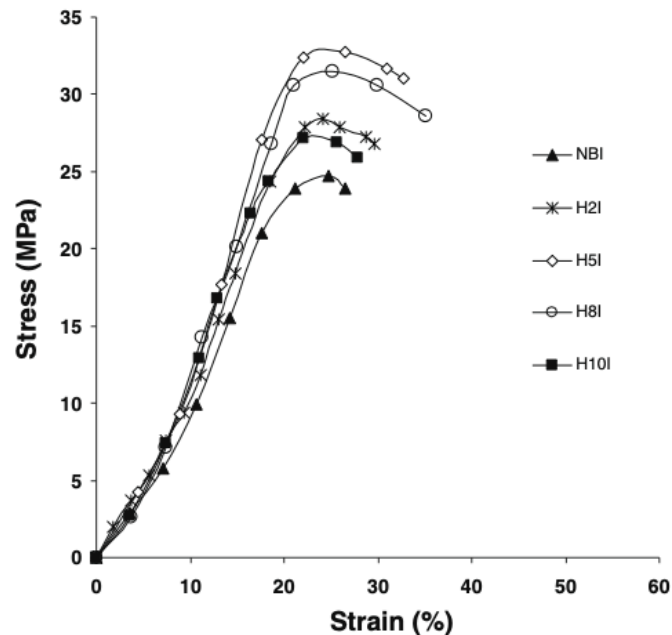


Figure 28. Stress-strain curves obtained for the injection molded samples.

As observable from the reported graph, the injection molded neat blend breaks at the lowest value of stress, which means that the spherical PET particles in it do not give a significant contribution to the reinforcement of the material. H2I and H10I have a similar behavior but H2I

slightly exceeds H10I because its fibrils are a bit longer. Moreover, in H10I has the lowest aspect ratio. Instead, H5I and H8I show a more ductile behavior compared to the others, they can undergo higher strains before breaking, beyond the yield stress. This means that these two samples are the stiffer and more resistant ones.

However, the tensile modulus of each microfibrillar composite created was proved to be higher than that of PP and of NB and the tensile properties of microfibrillar composites improved as the draw ratios increased. This tendency was inverted for high stretch ratios.

H5I and H8I have the longest fibrils inside and show high tensile modulus and high elongation at break. These are the reasons why these two composites have proved to be much tougher with respect to the NBI.

In addition, the dynamic rheology was investigated, carrying out the tests at a temperature of 205 °C. At this temperature, PP is in the molten state, whereas PET is in a semi crystalline phase and is rigid with respect to the matrix.

As the graph in Figure 29 shows, the storage modulus  $G'$  increases with the angular frequency  $\omega$  for all the tested specimens.

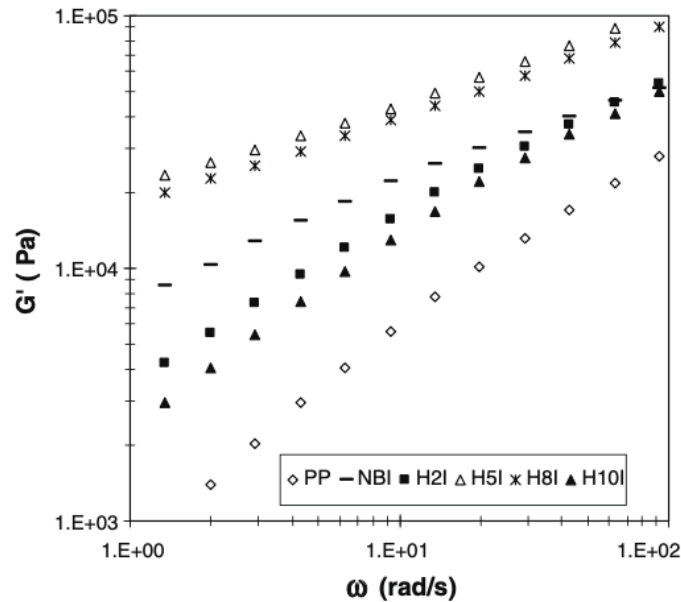


Figure 29. Storage modulus  $G'$  in function of angular frequency  $\omega$ .

The presence of a reinforcing phase within the matrix represents an obstacle to the relaxation of the PP macromolecules and that is the reason why the curves of the microfibrillar composites have a lower slope with respect to the neat polymer, especially at low frequencies. In fact, these curves tend to become flat at low values of  $\omega$  and the rheological behavior of the material becomes solid-like, instead of liquid-like, that is the more typical of pure polymers (PP in this case). This means that there is an increase in the elastic component of the typical viscoelastic behavior of polymers. As Figure 29 demonstrates, in fact, the better the reinforcing fibrils work, which means for example the higher aspect ratio they have (H5I and H8I here), the more the curves become flat and the final composite material results improved.

Also, the loss modulus  $G''$ , calculated at 205 °C increased with the angular frequency, but when  $\omega$  reached values around 100 rad/s all the curves assumed a similar viscous behavior and the differences in  $G''$  in all the specimens could be neglected (Figure 30).

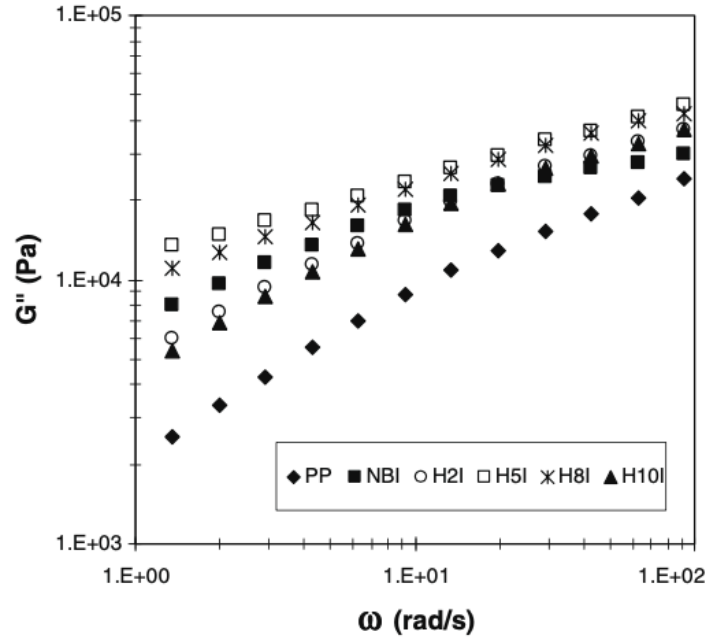


Figure 30. Loss modulus  $G''$  in function of angular frequency  $\omega$ .

Due to the fact that the difference between H5I, H2I and H10I at low values of  $\omega$  is much smaller than in the case of  $G'$ , it can be said that the PET reinforcing microfibrils play a more important role on the elastic behavior of the composite materials.

Finally, the complex viscosity  $\eta^*$  and the mechanical loss factor  $\tan\delta$  were investigated. As far as the complex viscosity is concerned, it has been calculated with the formula:

$$\eta^* = \left[ \left( \frac{G'}{\omega} \right)^2 + \left( \frac{G''}{\omega} \right)^2 \right]^{\frac{1}{2}}$$

again, at 205 °C.

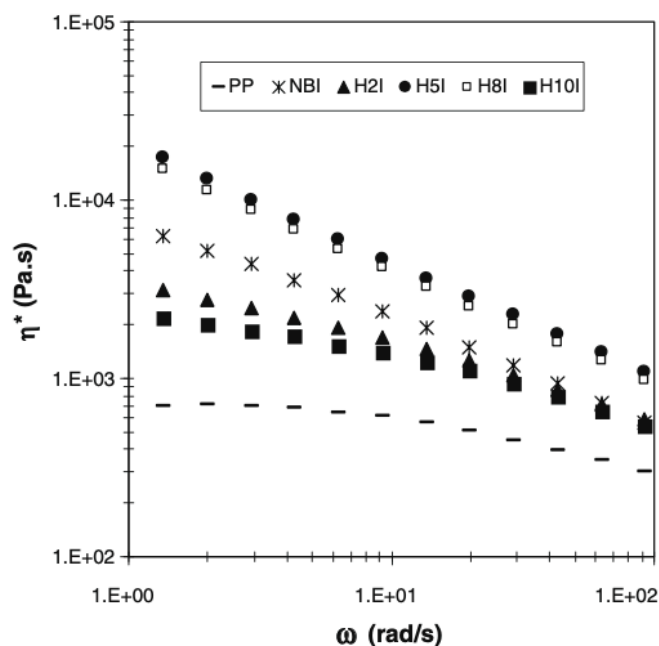


Figure 31. Complex viscosity as a function of angular frequency  $\omega$ .

As the graph in Figure 31 shows, also in this case H5I has the highest value of  $\eta^*$ . In all the specimens considered, the value of  $\eta^*$  is greater at very low frequencies and decreases with increasing the frequency. PP has the lowest complex viscosity, and this is in line with the fact that there is no reinforcement in it. Furthermore, at low values of  $\omega$ , it presents a Newtonian behavior.

The mechanical loss factor  $\tan\delta$ , instead, is expressed by the formula

$$\tan\delta = \frac{G''}{G'}$$

and has the evolution reported in Figure 15.

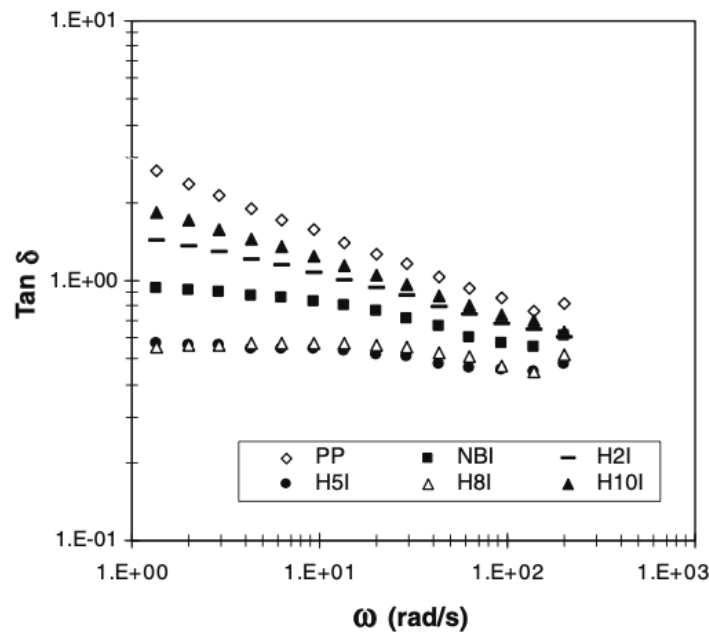


Figure 32. Loss factor as a function of angular frequency  $\omega$ .

It can be observed that H5I and H8I show a plateau region from low values of frequency until about 10 rad/s, and this means that in that region there is the formation of a network between the solid reinforcing fibrils in PET and the molten matrix in PP. As already explained for the storage modulus, this network blocks the relaxation of the macromolecules of PP and reinforces the final material. On the other hand, H2I and H10I are composed by fibrils with a low aspect ratio and for this reason their curves have a different behavior, in fact in these cases the PET reinforcement is not able to influence the relaxation of the PP matrix.

**Another interesting research conducted in 2006 by Taepaiboon et al. [9]** exploited the recycled PET coming from waste plastic bottles to produce a microfibrillar composite with an isotactic PP matrix. In their work, among the other results, they found out that the size of the PET flakes inserted at the very beginning of the process did not influence the final diameter of the fibrils that resulted at the end. Furthermore, they confirmed that the mechanical properties of the isotactic PP (iPP) were improved by the presence of PET fibrils, but they also investigated the effect of the addition of a compatibilizer, maleic anhydride-grafted polypropylene (PP-g-MA), to analyze its role in reinforcing the matrix. The immiscibility of the two coupled polymers, in fact, can provoke a lack of interfacial adhesion between the matrix and the reinforcement. The presence of a compatibilizer should enhance the interfacial bonding

between PET fibrils and PP matrix and, in this way, it is expected an improvement in the transferring of the stress from the matrix to the reinforcement. The obtained results, however, do not seem to confirm this hypothesis, as it will be shown in the following pages.

To prepare the composites with different concentrations, they dry-mixed pure iPP pellets, recycled PET (called rPET) flakes and PP-g-MA. The amount of PET was varied from 0 to 30% and PP-g-MA from 0 to 7%. These blends, then, underwent melt-blending carried out by a twin-screw extruder at 45 rpm and with a temperature profile of 130, 210, 240, 260, 270 and 280°C. The extruded material was collected by a rotating device with a speed of 400 rpm. Then, as shown in Figure 6, also in this case the extrudate was drawn between two sets of rolls situated across a heating tunnel, here set at 90°C. The leading rolls had a fixed speed of 10 rpm while the second was varied from 20 to 70 to achieve different draw ratios (from 2 to 7). After palletization, the composite materials were injection molded to obtain testable samples. The temperature range in this step of the process was 150, 160, 170, 180 and 185 °C and the injection pressure was 1700 bar.

The specimens were tested at room temperature and following the ASTM D638-91 standard test method. The flexural properties were investigated according to the ASTM D790 standard test method. The morphology of as-extruded and as-injection-molded samples was studied by scanning electron microscopy (SEM), they were cryo-fractured and covered with a thin layer of gold to provide a view of the transversal section. This procedure permitted to get a precise idea of the average diameter of the obtained fibrils, which quite notably decreased from the as-extruded samples to the drawn ones. For example, at a draw ratio of 2, the average diameter decreased from 1  $\mu\text{m}$  for the as-extruded specimen, to 0,6  $\mu\text{m}$  of the as-drawn one. This behavior was even more marked as the draw ratio increased (Figure 33).

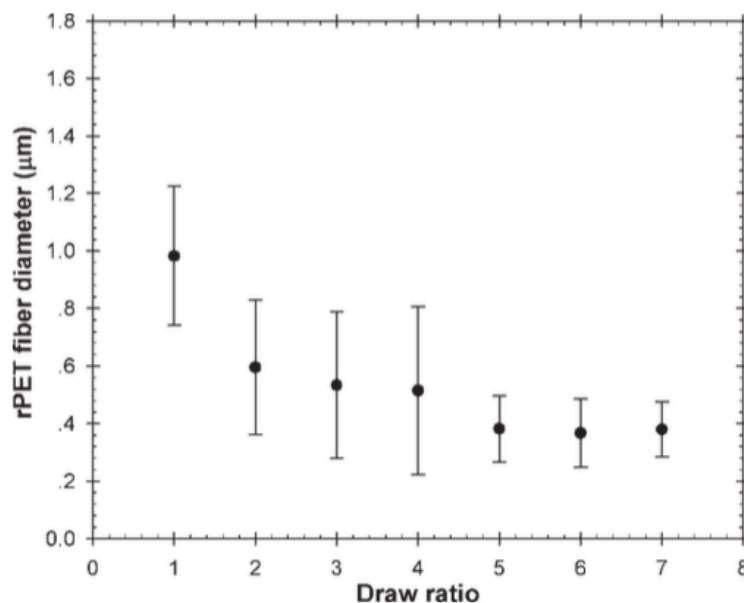


Figure 33. Fibrils diameter as a function of draw ratio.

The wide lines corresponding to low draw ratios (until draw ratio of 4) in the graph above were due to the irregular drawing, which caused a variable diameter of the fibers along their lengths, a phenomenon called “necking”. At high draw ratios (5 to 7), instead, the diameter of the fibrils reached a sort of plateau with a value of 0,4  $\mu\text{m}$ . To realize further investigations, the draw ratio of 7 was chosen because of the uniformity in the diameters shown in the mentioned tests conducted.

Subsequently, the effect of the initial size of rPET flakes on the mechanical properties of the resulting microfibrillar composite was investigated. To do this, the initial rPET flakes were subdivided into 3 groups according to their diameters:

- Group A: 0,5-1 mm;
- Group B: 1-2 mm;
- Group C: > 2 mm.

The amount of rPET in the blends was kept at 15%wt.

As mentioned before, the tests demonstrated that the size of the initial rPET flakes do not influence the final rPET fibrils diameter nor the mechanical properties of the iPP/rPET microfibrillar composite (Figure 34).

| Size of ground rPET flakes (mm) | rPET fiber diameter <sup>a</sup> (μm) | Tensile modulus (MPa) | Flexural modulus (MPa) | Impact resistance (J/m) |
|---------------------------------|---------------------------------------|-----------------------|------------------------|-------------------------|
| 0.5–1                           | 0.36 ± 0.11                           | 1914 ± 204            | 533 ± 40               | 34.1 ± 3.0              |
| 1–2                             | 0.38 ± 0.10                           | 1951 ± 189            | 528 ± 43               | 35.8 ± 2.5              |
| >2                              | 0.38 ± 0.11                           | 1877 ± 209            | 518 ± 37               | 34.3 ± 1.8              |

Figure 34. Influence of rPET flakes on fibrils' diameter and mechanical properties.

Thanks to the excellent mixing efficiency of the extruder used, the PET fibrils in the MFCs had very similar diameters despite the fact that the starting dimensions of the rPET particles were different, and this meant that there were no substantial differences even in the results of the mechanical tests.

Furthermore, the effect of rPET content was studied, in order to understand the optimal blend composition. To obtain this information, three kinds of rPET fiber samples were collected during different steps of the preparation of the MFCs.

- 1<sup>st</sup> kind of samples: as extruded material;
- 2<sup>nd</sup> kind: as-drawn samples at draw ratio of 7;
- 3<sup>rd</sup> kind: as-injection-molded samples.

In each type of samples, an increasing amount of rPET produced fibrils of bigger diameter and wider distribution (Figure 35).

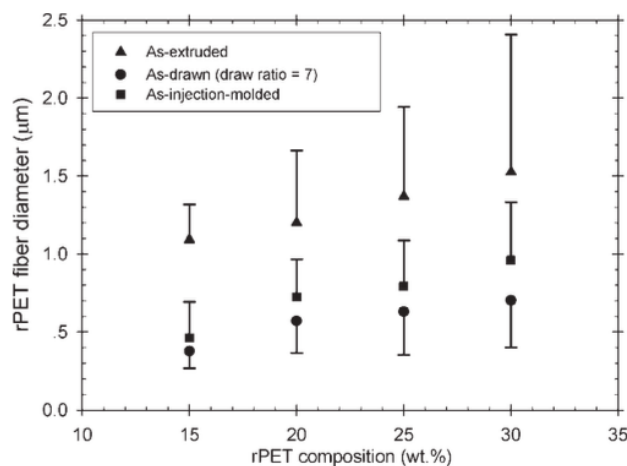


Figure 35. Fibrils diameter as a function of rPET composition.

The reason behind this result is probably the coalescence of the reinforcing phase. In fact, to a higher PET content corresponds a higher probability of collision and coalescence of two close reinforcing bodies. What is noteworthy is the fact that, regardless of the amount of rPET contained, the fibrils' diameters were higher in the as-extruded samples followed by the injection-molded and the drawn ones. This is in line with what one can expect because, after the drawing process at a draw ratio of 7, the diameter of rPET fibrils decreased of about three times (Figure 36), probably due to the shear and elongational stress implied in the drawing process.

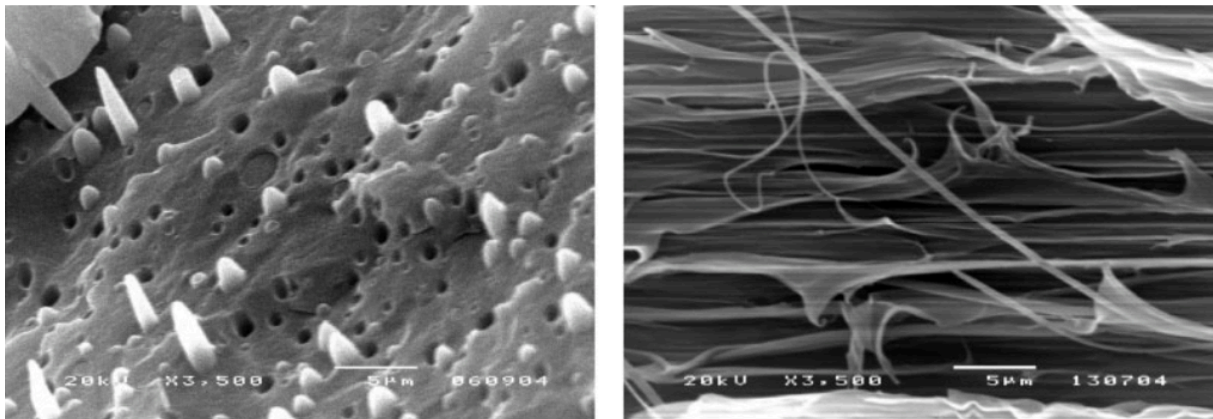


Figure 36. Composite iPP 85%wt and rPET 15% wt. rPET fibrils as-extruded (left) and as-drawn (right).

After injection molding, the reinforcing fibrils were basically kept in their positions and dimensions, but the diameters were found to be slightly increased, probably again due to the coalescence phenomenon. This can be explained because, even if the temperature set for the injection molding process was lower than PET  $T_m$ , it was notably higher than its  $T_g$ . Moreover, the conditions of pressure and shear required by this process may cause an increase in temperature.

As far as mechanical properties are concerned, the flexural modulus was the first investigated. As Figure 37 shows, the MFCs samples, both as-extruded and passed through the take-up device (MFCs-TU) and the drawn ones at draw ratio of 7 (MFCs-D7), presented notably improved results with respect to the pure iPP.

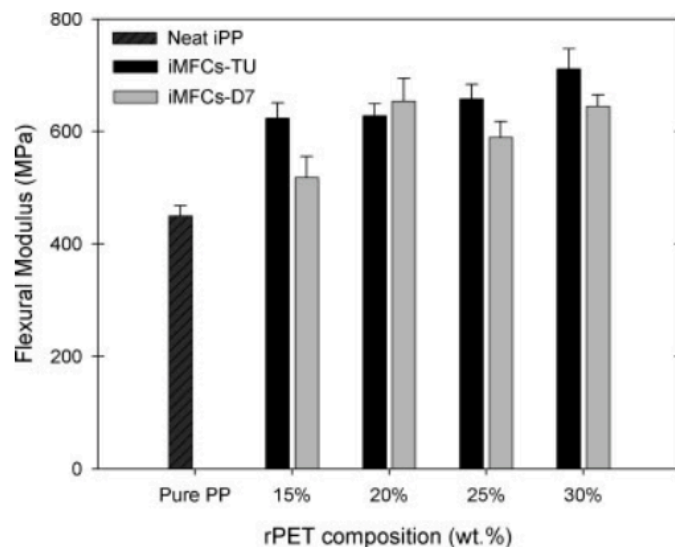


Figure 37. Flexural modulus as a function of rPET composition.

Instead, the flexural strength proved to be very similar to that of pure iPP.

The tensile modulus of microfibrillar composites MFC-TU seemed to be very similar to that of neat iPP, while it notably improved in the MFC-D7, especially with a rPET content of 20%wt (Figure 38).

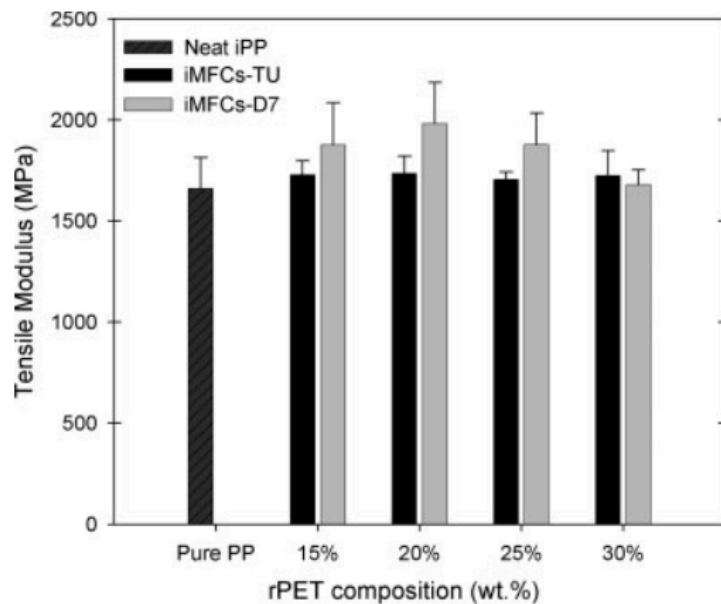


Figure 38. Tensile modulus as a function of rPET composition

Finally, the effect of PP-g-MA was investigated. The SEM images reported below and obtained for different compositions of the as-extruded composite show a significant lack of adhesion between the matrix and the fibrils, because of their mutual incompatibility (Figure 39).

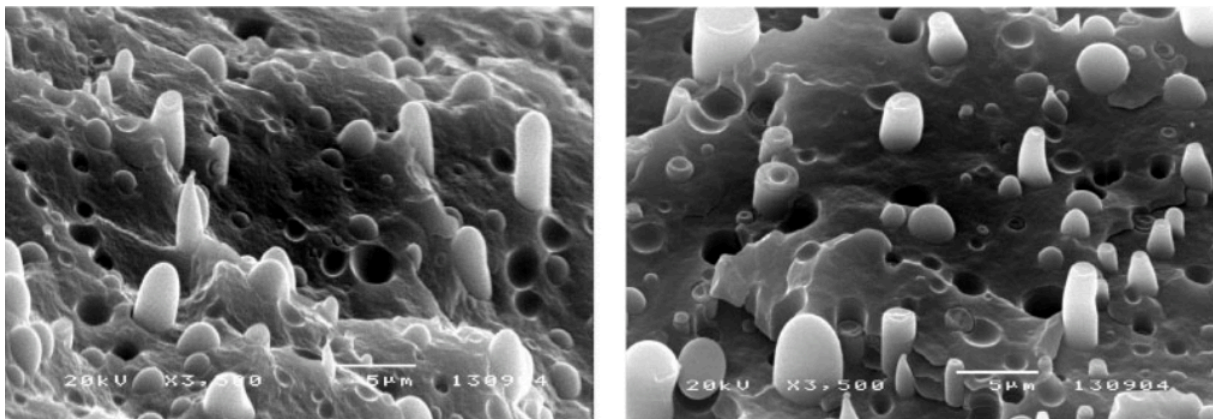


Figure 39 SEM images of as extruded iPP/rPET MFCs, 75%wt/25% wt (left) and 70%wt/30%wt (right)

To solve this problem, the addition of a compatibilizer in different amounts (0, 2, 3, 5, 7%wt) was attempted. In the following table (Figure 40) there are the results obtained for mechanical tests on samples containing different amounts of each component.

As it can be seen, not always the results are as good as expected and a SEM image (Figure 39) shows that there are not visible improvements in the interfacial tension.

| Composition of iMFCs (iPP/rPET/PP-g-MA) | Tensile properties |                      |                  | Flexural properties |                      |                  | Impact resistance (J/m) |
|---|--------------------|----------------------|------------------|---------------------|----------------------|------------------|-------------------------|
|   | Modulus (MPa)      | Yield strength (MPa) | Yield strain (%) | Modulus (MPa)       | Yield strength (MPa) | Yield strain (%) |                         |
| 100/0/0                                 | 1661 ± 153         | 31.1 ± 0.6           | 12.01 ± 0.43     | 450 ± 18            | 37.8 ± 0.7           | 0.31 ± 0.01      | 47.4 ± 3.1              |
| 85/15/0                                 | 1877 ± 96          | 29.4 ± 0.7           | 6.74 ± 2.10      | 518 ± 37            | 40.1 ± 0.4           | 0.33 ± 0.00      | 34.3 ± 1.8              |
| 85/15/2                                 | 1668 ± 43          | 30.7 ± 0.5           | 7.01 ± 0.28      | 579 ± 38            | 38.8 ± 0.8           | 0.29 ± 0.07      | 46.3 ± 3.2              |
| 85/15/3                                 | 1644 ± 56          | 31.0 ± 0.3           | 6.94 ± 0.42      | 624 ± 19            | 39.0 ± 0.7           | 0.27 ± 0.09      | 43.6 ± 2.3              |
| 85/15/5                                 | 1695 ± 39          | 31.2 ± 0.6           | 6.59 ± 0.37      | 592 ± 11            | 38.5 ± 0.8           | 0.27 ± 0.09      | 37.4 ± 2.3              |
| 85/15/7                                 | 1602 ± 23          | 31.1 ± 0.3           | 7.20 ± 0.41      | 595 ± 27            | 39.0 ± 0.7           | 0.32 ± 0.00      | 38.6 ± 2.7              |
| 70/30/0                                 | 1681 ± 74          | 32.0 ± 0.8           | 4.70 ± 0.39      | 645 ± 21            | 38.0 ± 1.6           | 0.13 ± 0.01      | 38.1 ± 2.3              |
| 70/30/2                                 | 2092 ± 104         | 28.4 ± 0.4           | 4.28 ± 0.22      | 623 ± 21            | 35.2 ± 1.0           | 0.13 ± 0.01      | 30.3 ± 1.2              |
| 70/30/3                                 | 2130 ± 92          | 29.6 ± 0.7           | 4.12 ± 0.45      | 632 ± 32            | 34.9 ± 0.4           | 0.13 ± 0.01      | 30.4 ± 1.3              |
| 70/30/5                                 | 2140 ± 81          | 30.1 ± 0.9           | 4.24 ± 0.44      | 622 ± 34            | 35.3 ± 1.3           | 0.13 ± 0.01      | 30.4 ± 2.6              |
| 70/30/7                                 | 1704 ± 114         | 27.9 ± 1.8           | 4.36 ± 0.55      | 613 ± 33            | 34.4 ± 0.8           | 0.13 ± 0.00      | 32.4 ± 2.4              |

Figure 40. Mechanical tests result for different compositions.

The Young's modulus improved with respect to that of pure iPP only in the uncompatibilized sample containing iPP/rPET 85/15 and in the compatibilized samples iPP/rPET/PP-g-MA 70/30/5.

The tensile strength proved to be nearly the same in all the specimens, there was no notable improvement with respect to the iPP and, as far as the yield strain is concerned, the samples' behavior was even a bit worse than that of neat matrix.

An enhancement, instead, was seen in the flexural modulus, where both the compatibilized and uncompatibilized specimens presented a higher value than the neat polymer. In all the other cases (yield strength, yield strain, impact resistance) the results were similar or even worse than the neat iPP.

After all, it can be said that the addition of the compatibilizer PP-g-MA in this system does not seem to change significantly its properties, but, if added, it is more suitable for MFCs with the composition of 85%wt/15%wt of iPP and rPET and an amount of compatibilizer ranging from 2 to 7%wt (Figure 41).

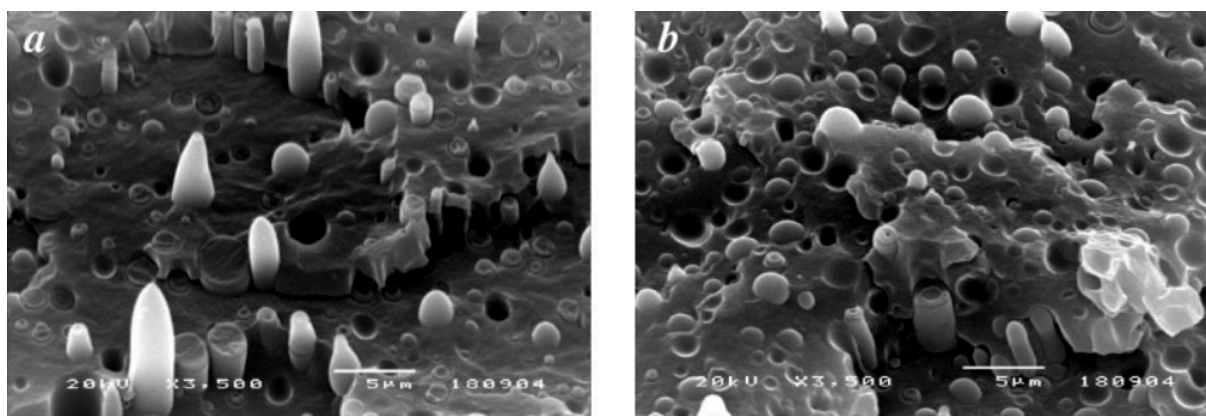


Figure 41. SEM images of the compatibilized samples with 3%wt (left) and 5%wt (right) of PP-g-MA.

**A second study that considers the addition of PP grafted maleic anhydride (PP-g-MA) to a microfibrillar composite made of PP and PET was conducted by Li et al. [8]**

In this case, they investigated the fact that, at high contents of PET (at least 40%) and at a screw speed of 40 rpm there is an inversion of the phases and the PP becomes the reinforcement while the PET the matrix. In these situations, the solution can be either maintaining a composition of 40%wt PET and 60%wt PP but a screw speed of 20 rpm during extrusion or the addition of 1%wt of PP-g-MA, that permits both keeping the same composition and reaching speeds of 80 rpm.

In this study, to obtain a good content of PET fibrils, a high concentration of PET was added to the PP matrix in the extrudate.

To avoid hydrolytic degradation during the extrusion, PET particles were dried at 100°C for 12h and PP-g-MA as well, but at 80°C. The materials mixed together (PP and PET or PP, PET and PP-g-MA) were then extruded using a twin-screw extruder with a temperature profile of 230, 270, 275 and 275 °C. The screw speed was varied, from 20, to 40 to 80 rpm.

Immediately after the extrusion, the obtained material was cooled down to 85°C and drawn by a stretching machine. The draw ratio was maintained constant at 14, the maximum value achievable without breaking the fibrils during stretching. At this point, the drawn filaments were subjected to compression moulding at 200°C for 20 min under a pressure of 3MPa. This pressure was kept until the temperature went back to room T.

As in the previous works, the morphology was investigated by scanning electron microscopy. The surfaces were previously cryo-fractured, then embedded in epoxy resin and etched by hot xylene at 130°C for 4h to remove PP and, finally, covered with a thin film of gold.

Viscosity of the pure polymers PP and PET was tested by a rheometer in frequency mode. Disks of the two polymers were pressed at 275°C, the extrusion temperature.

Thermal properties were tested by DSC at a range of temperatures varying from 50 to 280 °C and the heating and cooling rates were 20°C/min.

Tensile properties were conducted at room temperature with a cross head speed of 5 mm/min. Tensile modulus was measured by an extensometer and the strain was applied along the fibrils' direction.

As shown in Figure 42, where the viscosity versus shear rate at 275°C is reported, pure PP presents a pronounced shear thinning behaviour and a viscosity which is much higher than that of PET.

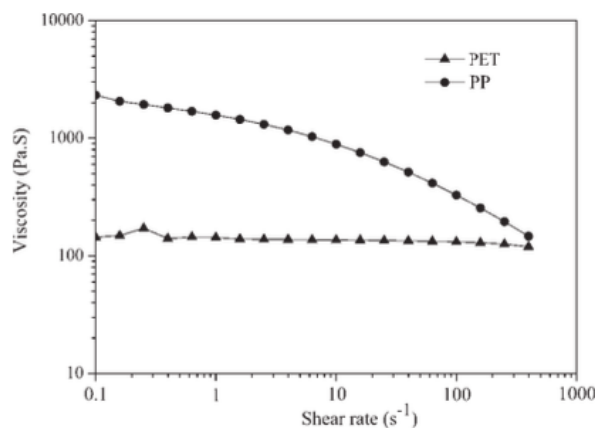


Figure 42. Viscosity as a function of the shear rate for PP and PET at 275°C.

The SEM analysis clearly demonstrated the morphology alterations occurring when the composition of the composite was modified, in particular when the amount of PET was increased. In Figure 43a, the concentration of PET is 30% wt and the extrusion speed is 40 rpm. The PET is the dispersed and spherical phase. Differently, when an amount of 40% PET is reached, two situations were observed. In the first (Figure 43b), the PET drops have coalesced and formed larger domains, while in the second (Figure 43c) there is the formation of the so-called “double emulsion morphology”. Here, PET became the matrix forming the continuous phase. At the same time, both droplets of PET and PP were still present.

Finally, when PET reached a concentration of 50%, it constituted the continuous phase and dispersed domains of PP could be identified.

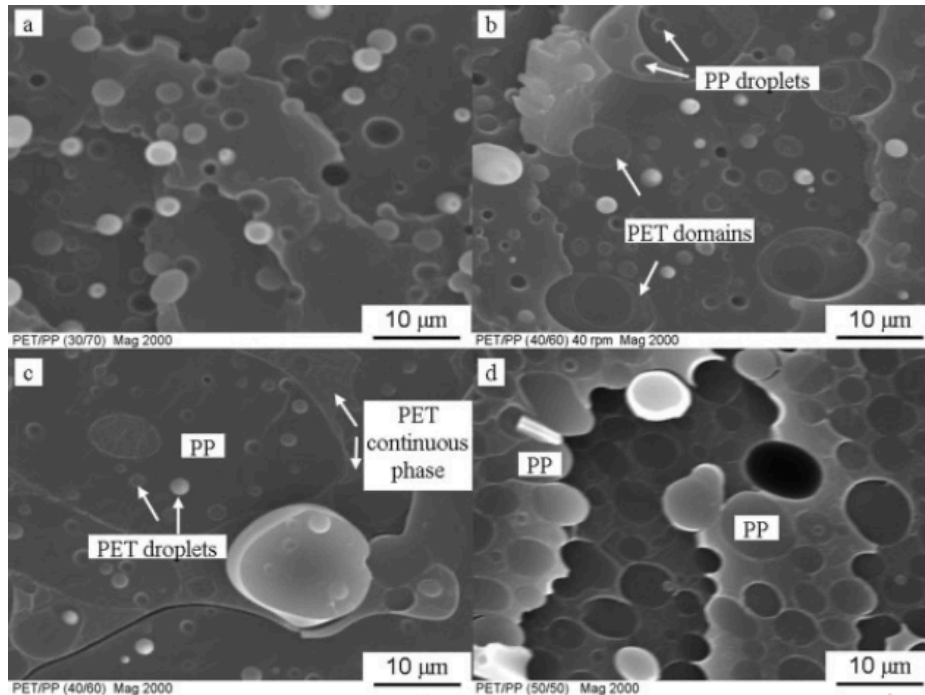


Figure 43. SEM images of PP/PET MFC with PET concentration varying from 30% (a), 40% (b and c), 50% (d)

Another morphological investigation was carried out after removing the PP phase with xylene. As can be seen in Figure 44a, in the case of PP/PET 70/30, the remaining PET phase assumed the shape of fibrils as required to create an MFC. In the other three pictures, instead, where the amount of PET was increased, it is shown the network produced by the PET forming the continuous phase, while the empty spaces are caused by the removal of the PP.

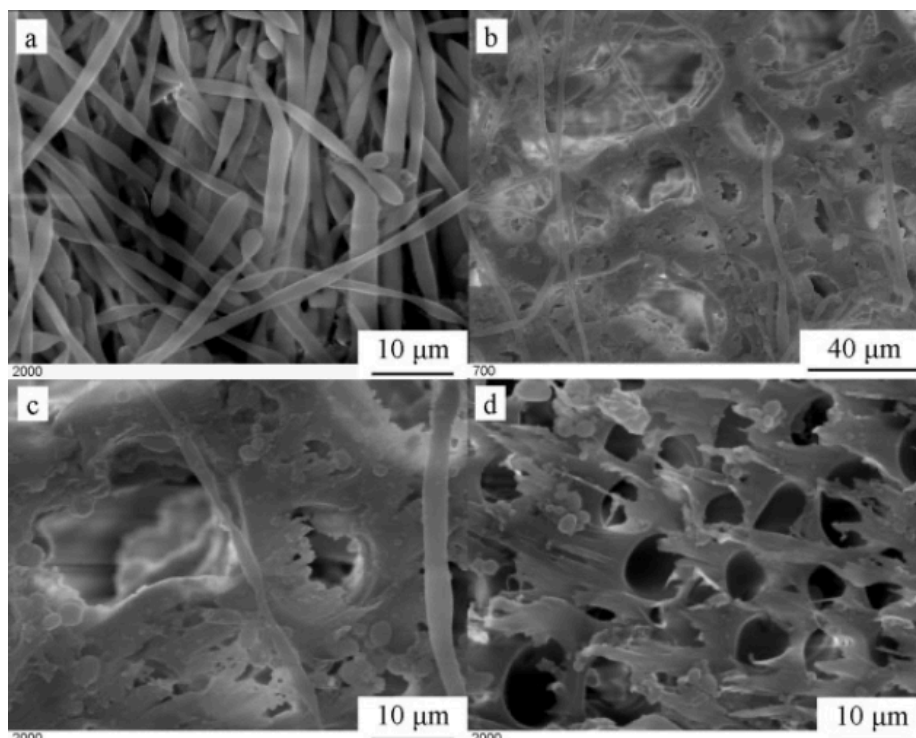


Figure 44. SEM images of the samples after the removal of PP.

To explain the phenomenon of the phase inversion that occurred for high contents of PET, the principle of the minimum energy dissipation must be taken into account. Basically, when two

immiscible polymers are melt-blended, the continuous phase is constituted by the component present in a major quantity, while the other forms the reinforcing dispersed phase. In fact, at a concentration of 30%wt, the PET is the dispersed component. According to the principle mentioned before, during melt blending, the continuous phase is formed by the less viscous material, while the more viscous becomes the dispersed phase. For this reason, when the concentration of PET increases up to 40 or 50%, being the less viscous component of the blend, it becomes the continuous phase.

Moreover, the effect of screw speed on the morphology of the two phases was studied, and PET/PP 40/60 was extruded at three different speeds: 20, 40 and 80 rpm. At 20 rpm, as said before, PET constitutes the dispersed phase and PP the matrix, having an appearance like the one reported in Figure 45.

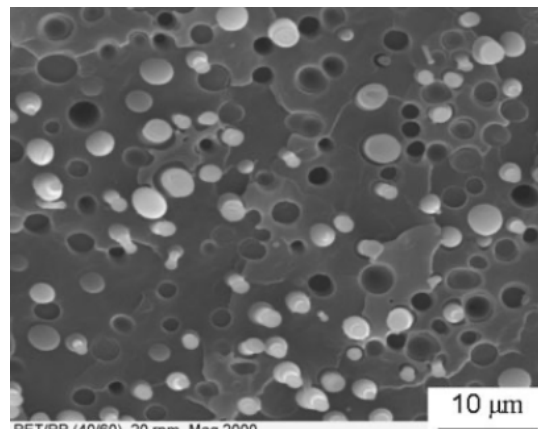


Figure 45. SEM image of PET dispersed in PP at 20rpm.

At higher speeds, the occurring phenomenon is the phase inversion and so at 40 and 80 rpm the PET becomes the matrix phase with the same morphologies as reported in Figure 43 b, c and d. The breakup and coalescence of the droplets are considered to be the main mechanisms governing the phase morphology and so it can be said that an increase of the screw speed brings to a thinner morphology. In fact, the more intensive shear stress caused by the higher speeds favors the breakup of the particles, but this is not the only result because an increased screw velocity also accelerates the coalescence process.

For this reason, during melt blending at low concentrations of PET, the breakup mechanism is predominant with respect to the coalescence one, because the interaction between particles is rarer. Therefore, at higher screw speeds, a finer morphology is generally obtained. When the concentration of PET increases, instead, the coalescence process must be taken into account. At 40 rpm, the reinforcing particles collide to form the matrix phase, and, at 80 rpm, the coalescence was completed, giving rise to the PET continuous phase. So, at high screw speed (and high concentrations of PET), the coalescence mechanism is predominant over the breakup one, first of all because with increased velocities it is more likely that the PET particles collide, and secondly because, being the less viscous material, PET tends to form the continuous phase. A useful scheme of the effects of blend composition, screw speed and different quantities of compatibilizer is shown below (Figure 46).

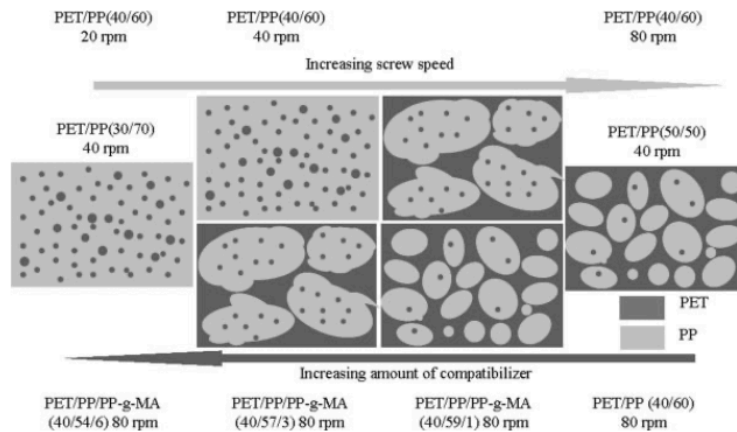


Figure 46. Effects of the described parameters on the phase morphology of PET/PP MFC.

To prevent coalescence and to reduce the interfacial tension, in fact, different amounts of compatibilizer PP-g-MA were added to the PET 40% and PP 60% blend, extruded at 80 rpm. When only the 1% of PP-g-MA is added to the blending materials, a slight change can be seen: the PET is still the continuous phase, but a region of double emulsion morphology typical of 40rpm, can be identified in the central area of the extrudate, which means that the coalescence of PET was reduced (Figure 47).

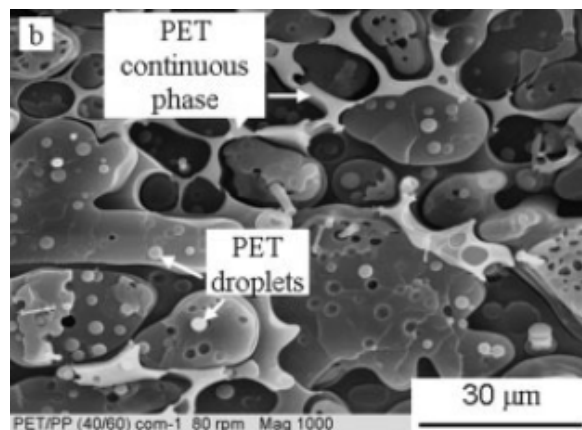


Figure 47. Area of double emulsion morphology with PET as matrix.

Adding the 3% of PP-g-MA, in the central area of the extrudate (Figure 48d) the PET coalescence is totally eliminated. On the edges instead (Figure 48c), where the shear stress is more relevant, the continuous phase is still made of PET and the double emulsion morphology can be distinguished.

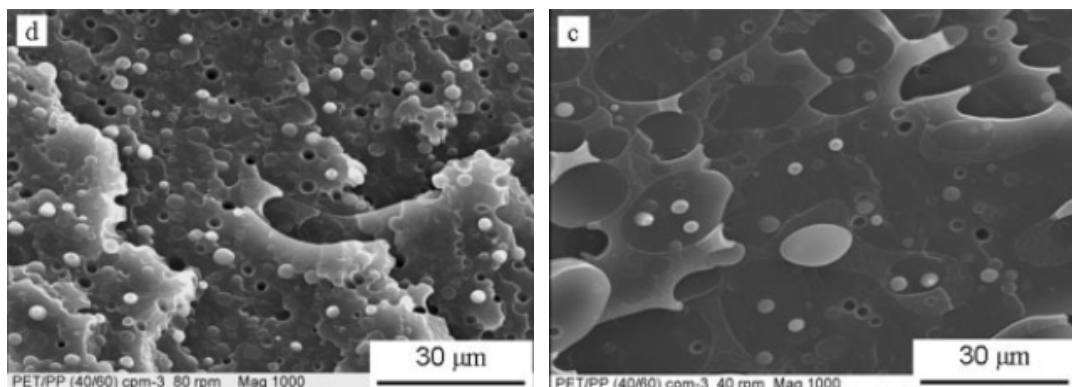


Figure 48. Consequences of addition of 3% PP-g-MA.

Finally, when the blend composition is 40% PET, 54% PP and 6% PP-g-MA, the coalescence of PET was completely eliminated, and PET turned to be the dispersed phase both in the central part and in the edges (Figure 49).

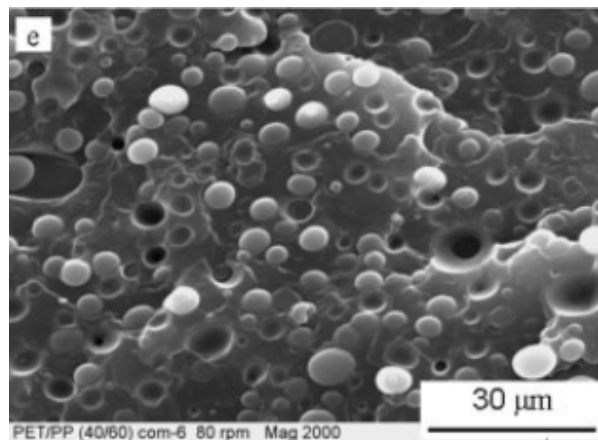


Figure 49. Addition of 6% od PP-g-MA.

Afterall, three different morphologies can be observed for blends extruded at 40 rpm and with the three concentrations:

- PET/PP 30/70 → PET droplets in PP matrix;
- PET/PP 40/60 → Double emulsion morphology;
- PET/PP 50/50 → PP domains in PET matrix.

As a consequence, after drawing, three different phase structures were observed (Figure 50). The samples were treated with hot xylene to remove PP.

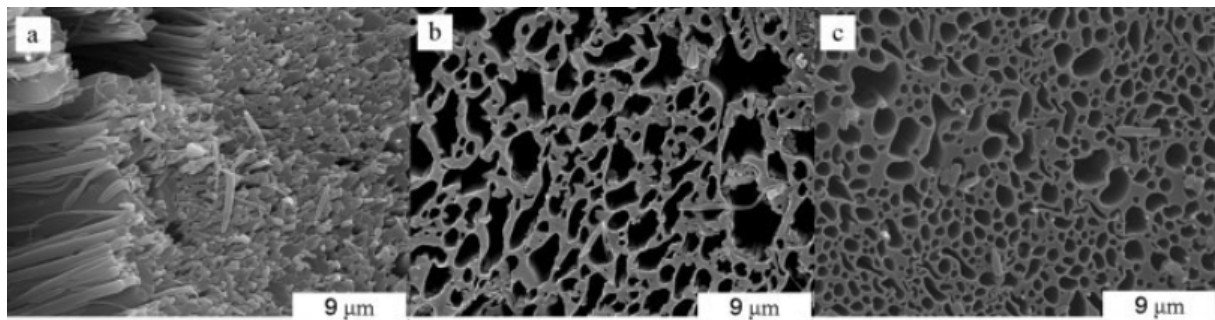


Figure 50. Different phase structures observed: PET/PP 30/70 (a), PET/PP 40/60 (b), PET/PP 50/50 (c).

The dispersed PET drops in the first extrudate (30/70) became long fibrils, the second extrudate (40/60) presented a double emulsion morphology where the holes are created by the removal of PP, and in the third extrudate (50/50), where the PP domains in the PET matrix were much smaller than those in PET/PP (40/60), the dimensions of the cavities left by PP removed had very thinner diameters.

To produce microfibrillar composites, only the first results for concentration PET/PP 30/70 are desired. The situations where the PET became the matrix are a problem if the objective is obtaining this kind of composites. If the concentration of PET exceeds 30%, then either a lower screw speed should be adopted or, to get a higher speed, a compatibilizer must be added.

To conclude, three types of stretched samples were used to get MFC, and then tested to obtain information about their tensile properties:

- PET/PP 30/70 extruded at 40 rpm;
- PET/PP 40/60 extruded at 20 rpm;
- PET/PP/PP-g-MA 40/54/6 extruded at 80 rpm.

As shown in Figure 51, a notable increase in both tensile strength and modulus are obtained, thanks to the presence of uniaxially oriented PET fibrils.

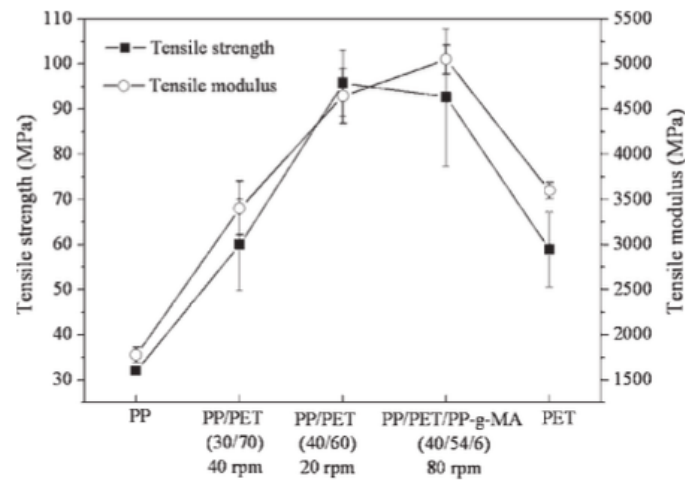


Figure 51. Tensile properties of the obtained MFC.

### 1.3 Fibrils in PTFE

Another material used to produce reinforcing fibrils is polytetrafluoroethylene, PTFE, and it is typically coupled with the molten matrix being kept in the solid phase.

**In a study conducted by Jurkzuk et al. [1],** solid powder particles of PTFE with high crystallinity were added to molten polymers such as isotactic polypropylene, high density polyethylene, low density polyethylene and atactic polystyrene, used as matrices. It has been observed that thinner and more resistant PTFE fibrils were obtained at higher values of deformation ratios and shear rates and at longer times.

Three different types of PTFE particles were coupled with different thermoplastic polymers, in particular three grades of isotactic polypropylene (iPP), high density polyethylene, low density polyethylene and polystyrene. The amount of PTFE used varied from 1 to 3, 5 and 7%wt and the compound was carried out with a co-rotating twin-screw extruder at a temperature between the melting T of the two coupled materials. The different temperature profiles changed on the basis of the matrix used.

As usual, the materials were characterized using a scanning electron microscopy to study the morphology, a wide-angle X-ray scattering (WAXS) to analyze the crystalline structure, Instron 5585 testing machine to assess the uniaxial tensile drawing with a load range of 0-100 kN.

The first type of PTFE, called 7C, is composed of two kinds of particles:

- Flat ellipsoidal particles with length between 20 and 60  $\mu\text{m}$ ;
- Flaky fibrillar particles with length between 90-200  $\mu\text{m}$ .

The second type of PTFE, F4-RB, contains both spherical and flaky particles with lengths in the range of 30-600  $\mu\text{m}$  and the third type, M-200, is composed by particles with a size of 0,2 - 0,3  $\mu\text{m}$  and aggregates smaller than 5  $\mu\text{m}$ . PTFE M-200 is composed of chain-folded crystals, while the other two PTFE form chain-extended crystals without many entanglements. These last two are expected to deform more easily.

The uniaxial compression of these PTFE 7C was tested as well, because it is fundamental in order to study the chain structure of the material and is more useful in this sense than the tensile drawing. PTFE 7C, before testing, underwent sintering at 290°C and melting at 360°C. If, after

sintering, its crystallinity increased from 94,7% to 95,1%, after melting, it drastically decreased from 94,7% to 46,2%, as a consequence of the entanglements created upon macromolecules during melting. After having calculated the compressive yield stress  $\sigma_y$  for sintered and melt-crystallized material at room temperature, the shear stress  $\tau$  acting at  $45^\circ$  can be obtained with the formula

$$\tau = \sigma \cos 45^\circ \cos 45^\circ = \frac{\sigma}{2}$$

To let the plastic deformation of PTFE 7C crystals in the polymeric matrix trough shearing, the stress value  $\frac{\sigma}{2}$  must be reached and overcome.

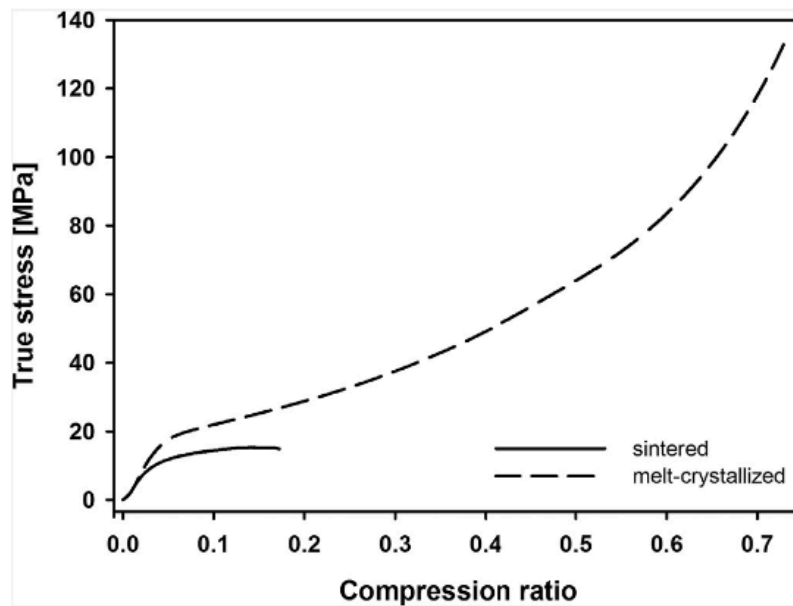


Figure 52. Stress as a function of compression ratio.

In the case presented in Figure 52, as an example, the yield stress for the sintered PTFE 7C is 12,1 MPa, so the shear needed to start the particle deformation is only 6,5 MPa at room temperature. Due to the fact that plastic deformation of crystals is a thermally activated process, the shear stress needed at the higher temperatures is even lower. Considering that, for example, the yield stress of PTFE 7C at  $200^\circ\text{C}$  is 6,18 MPa, the needed  $\tau$  will only be of 3 MPa. Even if sintered PTFE 7C breaks at low compression ratio, it continues to show notable ultra-drawing capability, unlike melt-crystallized PTFE 7C (Figure 53a and b).

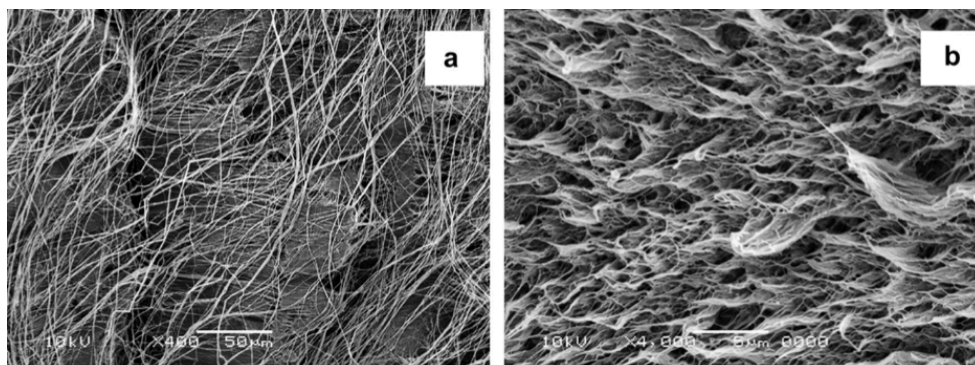


Figure 53. SEM images of sintered PTFE 7C (a) and melt-crystallized PTFE 7C (b)

As it can be seen from Figure 53a where there is a sintered PTFE 7C sample, from a single PTFE grain more than one fiber were drawn, which indicates that a single PTFE particle is composed of many large crystals, each one able to give rise to a single fiber during drawing. Instead, as shown in Figure 53b where the morphology of melt-crystallized PTFE is presented, this treatment causes a strain hardening stage, which indicates that the chain entanglements have formed again. This material, then, will not be adequate to be deformed at the large ratios required to form nanofibrils.

Subsequently, the effect of shearing on PTFE particles that have not undergone any treatment was studied. Samples of one kind of iPP mixed with 3% wt of PTFE 7C underwent shearing process with a rate of  $4 \text{ s}^{-1}$  and in a temperature range of  $200\text{-}230^\circ\text{C}$  until the matrix obtained the requested characteristics of deformation. The SEM images show the morphology of the obtained cryo-fractured samples of 97% PP and 3% PTFE deformed at  $\epsilon = 10$  (Figure 54),  $\epsilon = 1000$  (Figure 55) and  $\epsilon = 5000$  (Figure 56). Already the lowest deformation ( $\epsilon = 10$ ) causes a notable PTFE fibrillation, higher values bring to a higher number of thinner fibrils with a quite uniform thickness in the range of 30-150 nm.

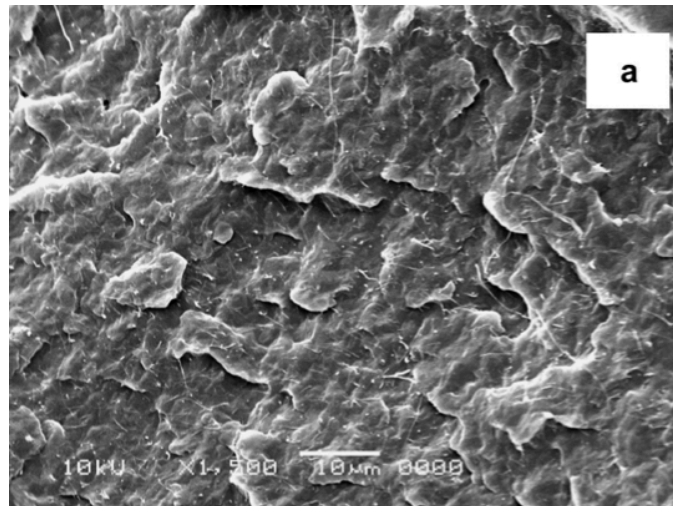


Figure 54. SEM image of cryo-fractured sample deformed at  $\epsilon = 10$ .

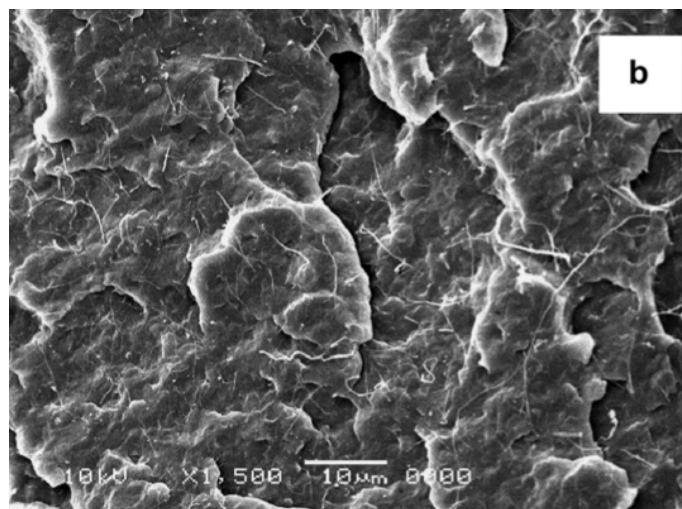


Figure 55. SEM image of cryo-fractured sample deformed at  $\epsilon = 1000$ .

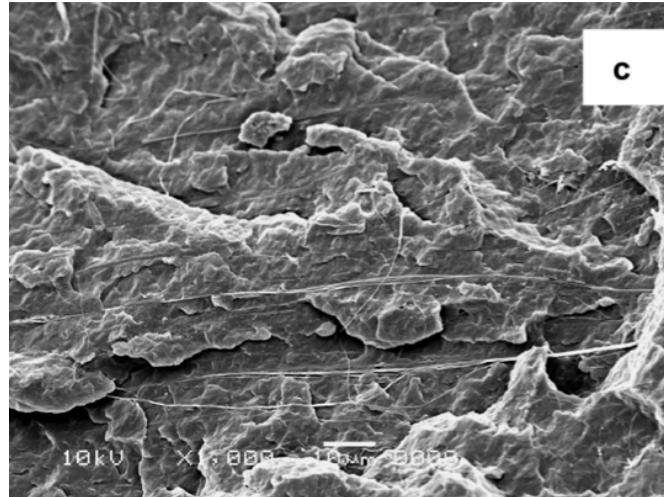


Figure 56. SEM image of cryo-fractured sample deformed at  $\epsilon = 5000$ .

The deformation of the PTFE particles is very similar to that of the matrix, which means that there is a very good transmission of the shear stress from the matrix to the reinforcement.

If this is what happens at shear rates of  $4 \text{ s}^{-1}$ , in a normal extruder where shear rates are of about  $1000 \text{ s}^{-1}$  these results are expected to be seen in a much more remarkable way. The following experiments were conducted on iPP matrix reinforced with the three different types of PTFE particles mentioned above. The PTFE 7C particles deformed very easily (as explained before), without a melting step, and the fibers obtained present a diameter among 30-580 nm (Figure 57). Something similar happens when the reinforcement is constituted by F4-RB PTFE particles (Figure 58), the obtained fibrils have a diameter ranging from 60 to 650 nm, while a different behavior is seen in the case of M-200 PTFE. In this last situation, in the iPP matrix some aggregates with longitudinal size of 3-10  $\mu\text{m}$  can be distinguished (Figure 59). Also the matrix's viscosity was found to have a role on the efficiency of PTFE fibrillation: a lower viscosity of the PP matrix brings to the fibrillation of only a part of the PTFE grains, while a more viscous material (like HDPE) promotes the fibrillation of nearly all the PTFE particles present in the melt.

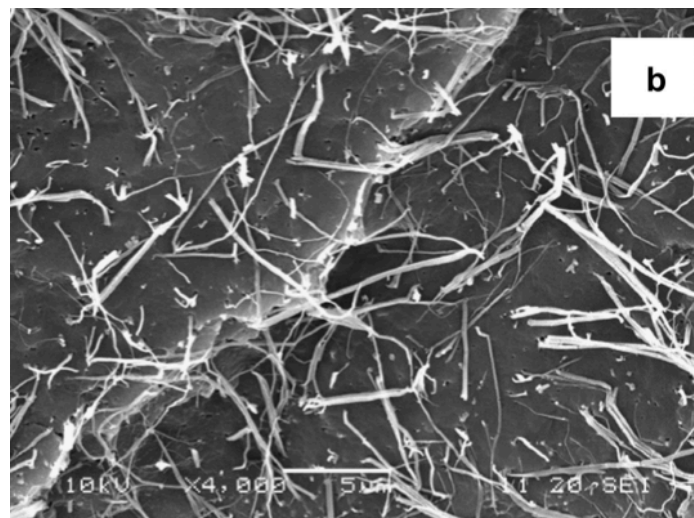


Figure 57. SEM image of deformed PTFE 7C particles.

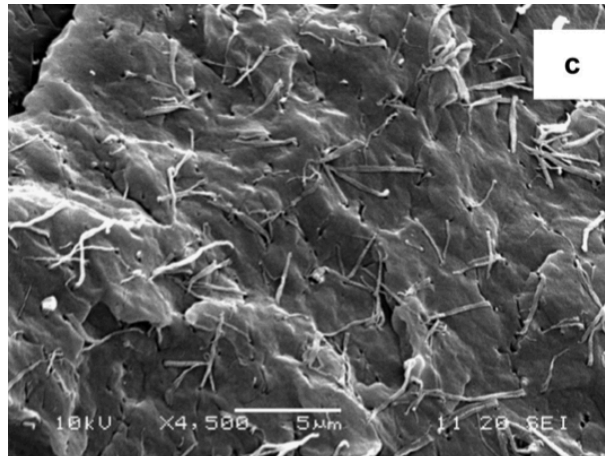


Figure 58. SEM image of deformed F4-RB PTFE particles.

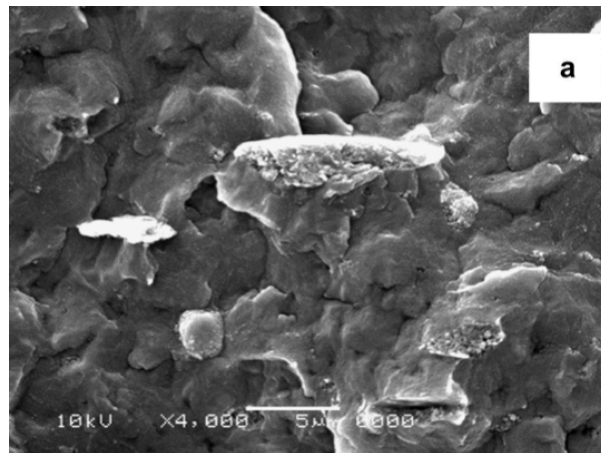


Figure 59. SEM image of deformed M-200 PTFE particles.

The obtained nanocomposites and their properties (like thickness and aspect ratio) strongly depend on the used machines and materials' brands, as well as on the thermoplastic matrix employed, its viscosity, the set parameters such as shear rate and time. In particular, it has been observed that the longer the time spent during the compounding, the more relevant the PTFE 7C particles deformation under a constant shear rate and so, the stronger and thinner the obtained nanofibers.

Using tensile drawing and impact testing, the mechanical properties of the obtained materials were investigated. The most interesting results obtained are those observed in the case of PP matrix containing 3%wt of PTFE 7C nanofibrils. PTFE, especially in the shape of fibrils promote the nucleation of PP crystals and this provoked the increase in the composite's crystallinity of the 5%. This phenomenon caused the increase in the modulus of elasticity of about 35%. The studied nanocomposites present a brittle behavior with low elongation at break, but they are notably stronger and stiffer with respect to the neat materials. In fact, semicrystalline polymers such as HDPE and iPP are quite brittle at low temperatures, easily undergo ductile-to-brittle transition and do not resist so much under high shear strains. The PTFE long and high strength fibers improve considerably these polymers' characteristics. To verify this concept, the influence of reinforcing fibrils was investigated by an impact test using the Izod method.  $U_I$  is the Izod impact strength measured in the different composites (Figure 60).

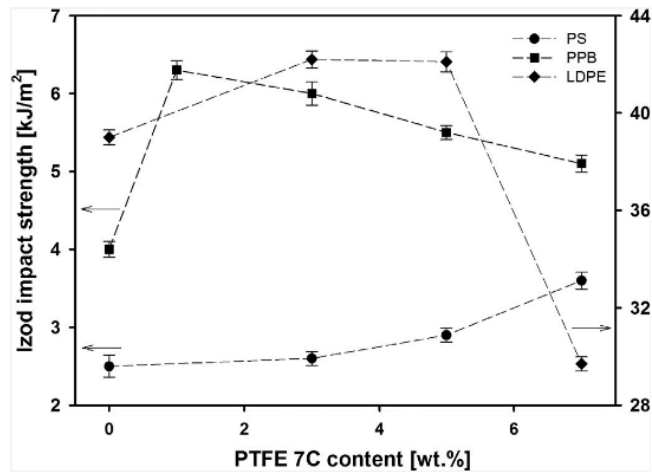


Figure 60. Izod impact strength as a function of PTFE 7C content.

As the graph above shows, when the matrix is PS,  $U_I$  continuously increases with the increase of the amount of PTFE 7C, until it reaches a value that is up to 40% more than that of neat PS when it contains 7% of PTFE fibrils. PP (in the PPB type here), presents a  $U_I$  increased by 50% when only 1%wt of PTFE is introduced. The less marked effect is presented by HDPE, where the addition of 3 or 5% of PTFE only brings to an increase in  $U_I$  of the 8% with respect to the neat one.

Finally, the storage modulus  $G'$  (here called  $E'$ ) has been measured as a function of the temperature to assess the mechanical behavior of PP-based obtained materials. In Figure 61, the storage modulus of neat PP (PPB type) is compared to its nanocomposites containing 3, 5 and 7% wt of PTFE 7C. The greatest increase in  $G'$  is observed when 3% of PTFE is added and all the materials become stiffer when temperature decreases.

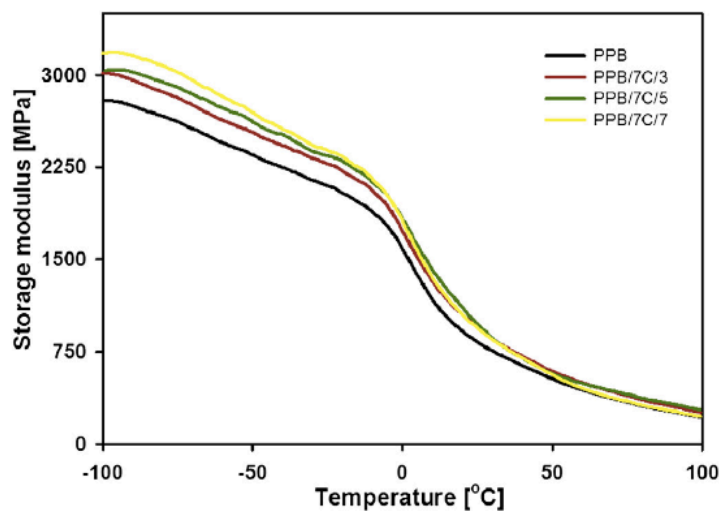


Figure 61. Storage modulus as a function of temperature.

**Another study conducted again by Jurczuk et al. [7]** investigates the effect that PTFE nanofibrils provoked on rheological and mechanical properties of a blend composed of a thermoplastic elastomer and LDPE. This blend was used as a matrix. Also in this case, solid PTFE particles were added to the melt. The PTFE fibrils produced an entangled network that improved a lot the blend's mechanical and rheological properties. In particular, the strain hardening coefficient of the PTFE reinforced blend, and its mechanical properties, were found to have notably improved depending on the amount of PTFE fibrils contained.

The used materials were PTFE 7C with a melting temperature of 346°C as the reinforcement while, to produce the matrix, LDPE and two types of TPE were used:

- Ethylene-octene copolymer (called Infuse);
- Ethylene-butene copolymer (Koattro).

The composite material was produced using an internal batch mixer at 170°C for 10 min with a rotor speed of 100 rpm. The chosen temperature is higher than TPE and LDPE melting T but much lower than that of PTFE. Initially, 20%wt of PTFE and 80%wt of LDPE were mixed together. Afterwards, the obtained material was diluted in a TPE matrix to obtain a final composite with a content of 3, 5 and 8%wt PTFE. The obtained films were compression molded at 140°C and then cooled down to room temperature.

The composites' morphology was studied using the scanning electron microscopy and following two different methods:

- Fracture of the specimens at the temperature of the liquid nitrogen;
- Etching of polymeric matrix with permanganic etchant (only polyolefins are susceptible to this substance).

The thermal properties were investigated by differential scanning calorimetry while the crystalline structure by WAXS analysis. Thanks to a strain-controlled rheometer the rheological behavior of the samples was investigated. Tensile properties were tested at room temperature and with the tensile testing machine Instron 5582.

As already mentioned above, PTFE is composed by large crystals with a low degree of chain entanglements in its amorphous phase: this factor promotes its ability to deform into fibrils. The fibrillation process depends on several factor, among which one the most important is the interfacial tension measured between solid PTFE particles and the molten matrix. In fact, the interfacial tension influences the stress transfer that passes from the matrix to the reinforcing particles and, in order to obtain the highest stress transfer, the interfacial tension should be the lowest possible. If this stress transfer is effective, higher deformation ratios can be reached.

The calculated interfacial tension between matrix and reinforce at 170°C (compounding temperature) was 8,8 mN/m which is not so low, but low enough to permit and effective shear stress transfer from LDPE to PTFE and let the transformation into nanofibers begin in the reinforcing phase. To investigate the diameter of obtained fibrils, the etching of TPE/LDPE was applied (Figure 62). The diameters of PTFE nanofibrils obtained range from 30 x to hundreds of  $\mu\text{m}$ .

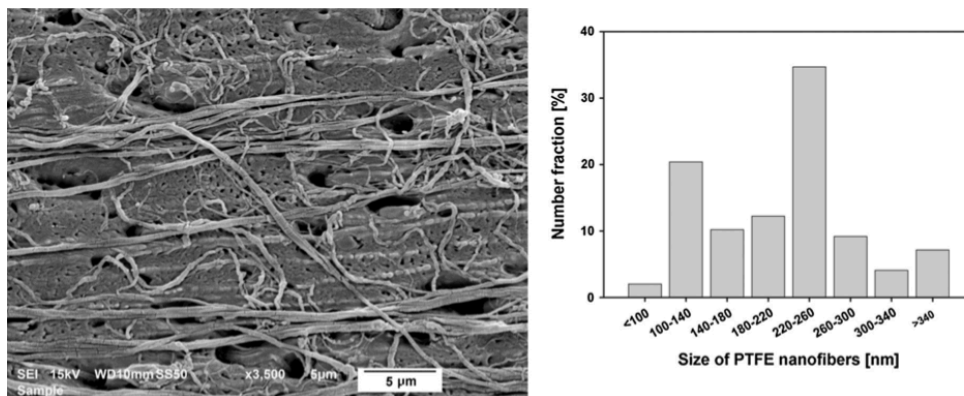


Figure 62. Etching applied to investigate the diameter of the obtained fibrils.

The results obtained from the rheological properties showed the result of PTFE nanofibers on the final viscoelastic behavior of TPE/LDPE blends. Storage modulus  $G'$  and loss modulus  $G''$  were evaluated (Figure 63a and 46b) as a function of angular frequency  $\omega$  in the cases of neat TPE (Infuse), TPE/LDPE and TPE/LDPE/3%PTFE.

Concerning the neat TPE Infuse, both  $G'$  and  $G''$  increase with the increase of the angular velocity and, for low values of  $\omega$ ,  $G'$  is smaller than  $G''$ , which confirms the viscous behavior of the material. The same kind of behavior was observed for the TPE/LDPE blend, while a different one characterizes the TPE/LDPE/PTFE material. The last one, in fact, presents a viscoelastic behavior as demonstrates the increase of both  $G'$  and  $G''$  in the low frequencies range. In particular,  $G'$  tends to reach a sort of plateau at low  $\omega$ , which represents the solid-like response and is due to the presence of PTFE entangled network that makes more difficult the relaxation of the matrix's molecules.

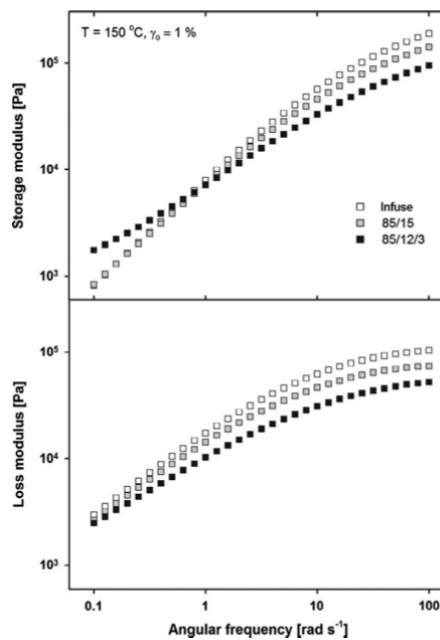


Figure 63. Storage modulus (upper) and Loss modulus (lower) as a function of angular frequency.

Finally, the mechanical properties were investigated by tensile drawing. In composite materials containing PTFE, properties like the modulus of elasticity  $E$  and yield stress  $\sigma_s$  are proved to notably increase, while others like stress at break  $\sigma_b$  and elongation at break  $\varepsilon_b$  decrease with respect to those measured for TPE/LDPE blends. The highest value obtained of elasticity modulus, by the way, was the one obtained from the addition of 8% of PTFE to the TPE/LDPE matrix (Figure 64).

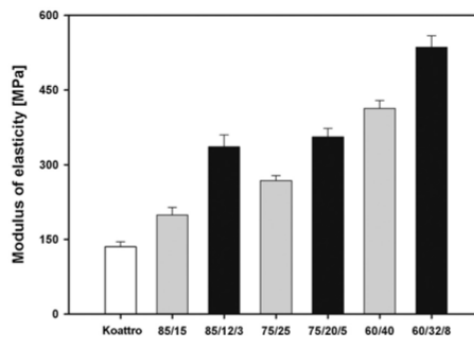


Figure 64. Elasticity modulus with different contents of PTFE.

**In situ fibrillated PTFE was also studied by Huang et al. that coupled it with a thermoplastic polyurethane (TPU) matrix.** [10] PTFE effects on the rheological behaviour, mechanical properties and foamability of TPU/PTFE composites were investigated. The presence of PTFE was found to significantly improve mechanical properties, the foamed structure and the hydrophobicity of the composite material.

The all-polymer composites were prepared using a co-rotating twin-screw extruder with 1, 3 and 5% wt of PTFE as the reinforcing phase in a TPU matrix. Rotation speed was kept at 80 rpm and the extruder temperature profile set went from 165 to 185°C. an injection molding machine able to prepare microcellular and solid tensile bar was used.

The thermal properties were characterized by DSC and TGA, under nitrogen atmosphere. To evaluate mechanical properties an Instron 5967 was employed while SEM was used to study morphological properties. In particular, the diameter of the pores was calculated thanks to the SEM images using a specific software called Image-Pro Plus. Dimethylformamide (DMF) was chosen as an etchant to better see the PTFE fibrils' configuration in the obtained composites. Dynamic mechanical analyses (DMA) were conducted in compression mode and rheological properties were measured by a TA rheometer with parallel plates. The surface wettability of neat TPU and TPU/PTFE was investigated with a Dataphysics OCA 15 instrument.

The chosen PTFE has a melting temperature of 328°C, therefore it can't melt when it undergoes the extrusion process. The way in which the fibrils are originated is simplified in Figure 65.

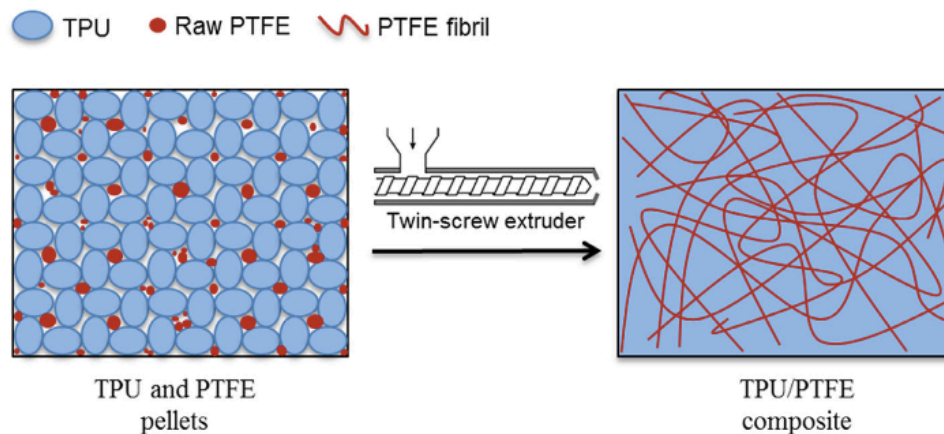


Figure 65. Mechanism of fibrils formation.

The morphologies of DMF etched samples are presented in Figure 66, in order to show the conformation of the PTFE fibrils without the TPU matrix. The mean diameter of the fibres was about 1  $\mu\text{m}$  but it increased, together the length and the number of fibers, with increasing PTFE content. The higher the fibrils' length, the higher the aspect ratio and, furthermore, several fibers were found to be disposed in an entangled network. PTFE deformed into fibrils during the compounding process because of its low yield strength at high temperatures and its plastic deformation. After PTFE underwent the process, it could not return in its original oval or spherical shape, that means that the new shape can be preserved under its  $T_m$ .

Mechanical properties showed that the obtained composites have an incredible tensile strain and none of the samples could be broken during the test. The slope of the linear region shown in Figure 67 increased with the increase in the amount of PTFE, which confirms that the PTFE has a reinforcing effect on the TPU matrix. This is due to the fact that PTFE has a high modulus

with respect to that of TPU. As it can be seen from the image, TPU/PTFE composites show a lower tensile stress if compared to the neat TPU when vary high strains are reached. This can be a cause of the sliding that occurs between the matrix and the dispersed phase because of PTFE's low friction coefficient.

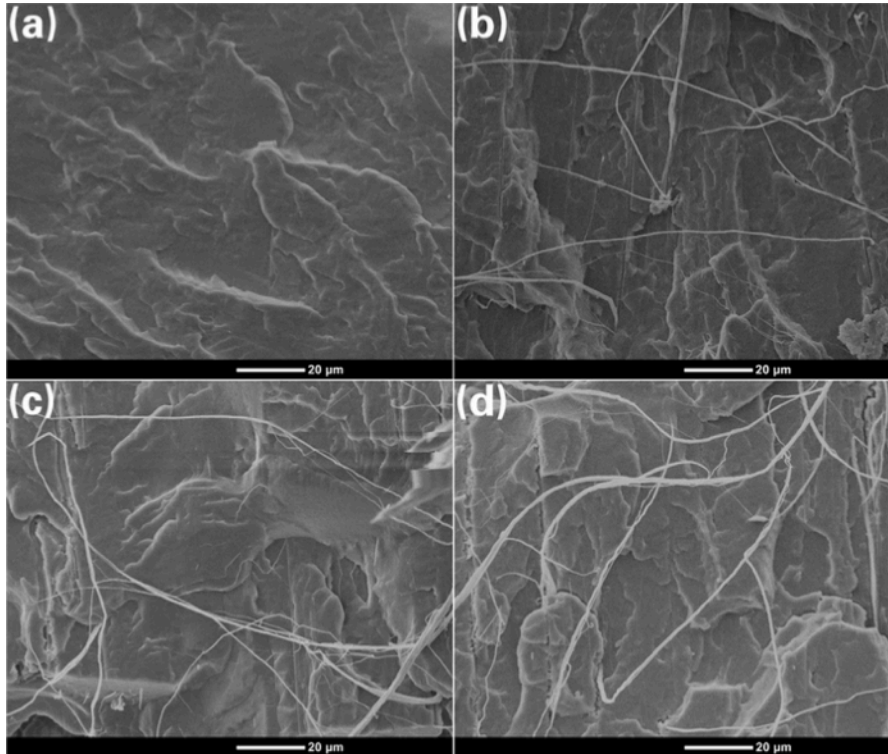


Figure 66. Morphology of etched PTFE samples without the TPU matrix.

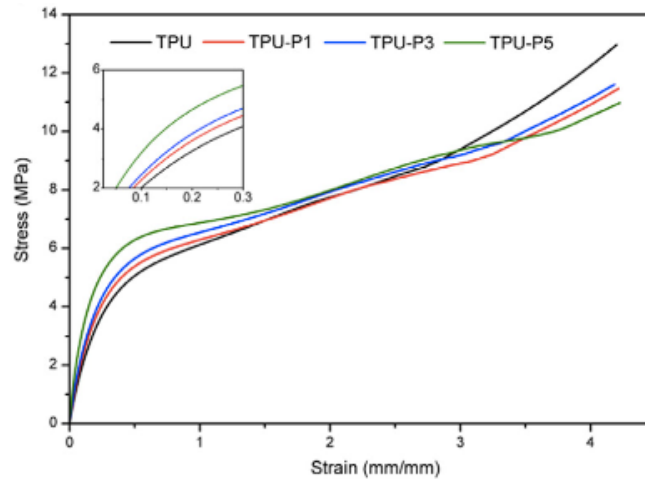


Figure 67. Stress as a function of strain.

Furthermore, the storage modulus  $G'$  (also in this case called  $E'$ ) as a function of temperature was investigated. As Figure 68 presents, PTFE presence notably modified the storage modulus behavior of the final composite, with respect to the neat TPU. In particular it enhanced the elastic properties of the final materials and, furthermore, it has been observed that the storage modulus increased with the increasing amount of PTFE content and this can be due to the fact that the formation of a great quantity of fibrils inhibits the deformation of the composite while

it promotes the storage of a larger amount of deformation energy. The increase in temperature provokes the sharp drop of the storage modulus in every sample.

Figure 69a confirms the liquid-like behavior of the TPU matrix with a storage modulus' slope of 2. TPU, in fact, has a homogeneous isotropic melt with the typical behavior of the homopolymers at low frequency values. Its chains are completely relaxed. Things are different, instead, for the composite materials, where the addition of PTFE lowers the dependence of  $G'$  from the angular frequency at low values of  $\omega$ . The plateau that appears at low frequencies in all the composite materials underlines the viscoelastic behavior obtained in these three cases in comparison to the neat TPU, and it means that there is the transition from a liquid-like behavior to a solid-like one. The solid-like behavior at low  $\omega$  confirms the presence of an entangled network that inhibits the matrix's relaxation. The fact that, at high frequencies, the value of  $G'$  for all the three composites is slightly lower than the neat TPU can be due to the fact that PTFE has an incredibly low friction coefficient and, at higher values of  $\omega$ , its fibrils disentangled. Also the complex viscosity was measured, as a function of  $\omega$ , at 180°C (Figure 69b). The neat TPU melt shows a Newtonian plateau at low angular frequencies and a shear thinning behavior at high  $\omega$ . The composite materials, instead, present a non-linear behavior along the frequency range: the increase in the complex viscosity at low frequencies underlines the strong interactions between the matrix and the reinforcing fibrils.

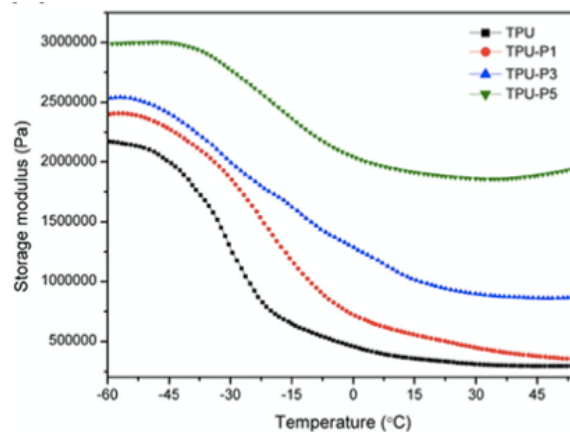


Figure 68. Storage modulus as a function of Temperature.

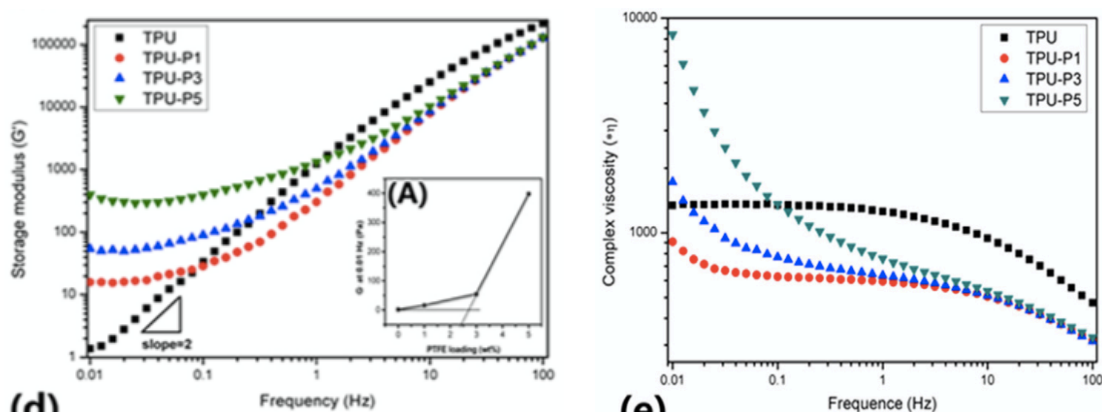


Figure 69. Storage modulus and complex viscosity as a function of frequency.

Microcellular injection foaming (MIF) was then conducted on these materials, and the resulting systems were investigated through a micro-CT machine, SEM and contact angle analysis. Very important improvements were observed after the addition of in-situ fibrillated PTFE, there is in

fact a linear relationship between pore size and PTFE content and the pore morphology has proven to be more uniform when this reinforcement is present. The comparison between the neat TPU pore dispersion and the TPU/PTFE 5% (the maximum amount of PTFE ever added in this article) is shown in Figure 70.

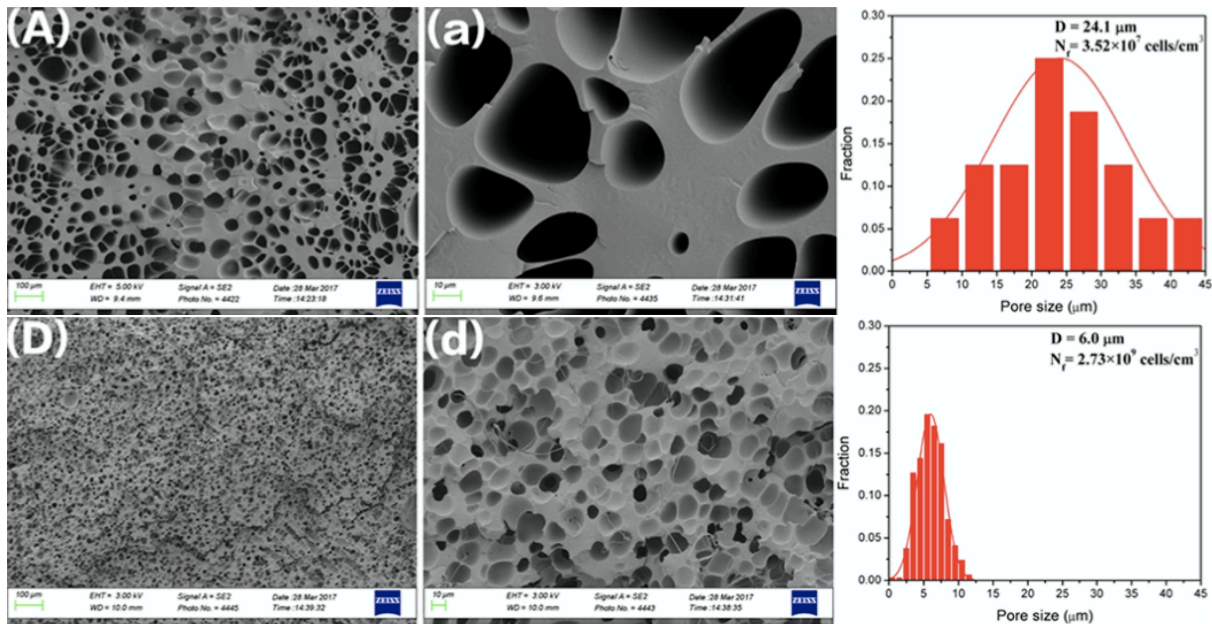


Figure 70. Neat TPU vs. TPU/PTFE 5% pore dispersion.

As expected, the pore morphology in the composite materials is much more uniform with respect to the neat TPU. The pore size decreased, and their density increased with the addition of PTFE and this is due to its pore nucleation effect. The composite material containing 5%wt of PTFE more than the others improved pore density and mechanical properties because PTFE fibrils also induce crystalline heterogeneities that promote pore nucleation and the entangled network constitutes a topological limit to the pore growth, fact that improved the material's melt strength (Figure 71).

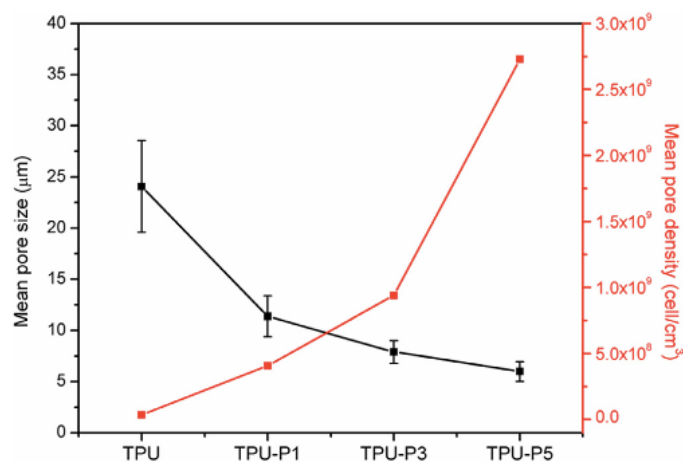


Figure 71. Mean pore size and mean pore density as a function of PTFE content.

Finally, the last property investigated was the wettability of the obtained composites: an increased hydrophobicity in fact, is very useful to introduce TPU-based materials in new fields of the industry such as automotive and food packaging. Also in this case, the PTFE fibrils were proven to improve the final material's properties (Figure 72).

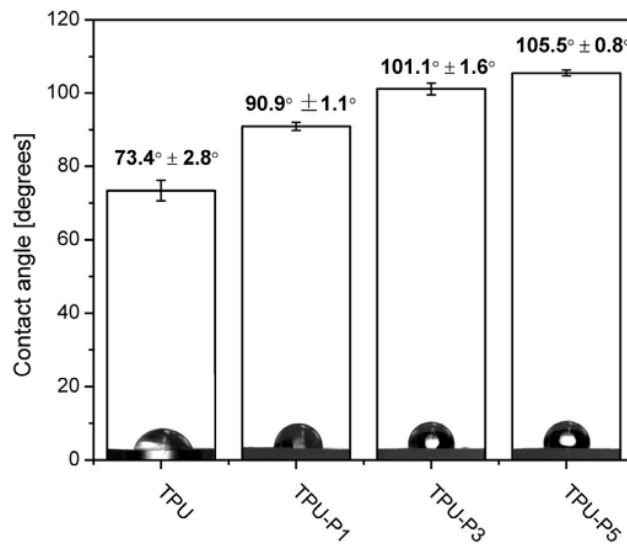


Figure 72. Contact angle as a function of PTFE content.

#### 1.4 Fibrils in PA6

Polyamide (PA6) fibrils are usually coupled with polylactic acid (PLA) matrices. PLA is an important biodegradable and biobased material that can be produced from renewable resources. Some of its drawbacks can be improved by adding a small quantity of PA6 in order not to vanish the ecofriendly nature of PLA but improve some of its properties. [6]

**Ramezani Kakrodi et al.** [6], obtained the first microfibrillar composite made with these two materials.

After drying, the two materials were coupled in a Leistritz co-rotating twin screw extruder with a rotation speed of 100 rpm and a temperature profile of 160, 180, 205, 210, 220, 220, 230, 230, 230 and 230°C. The amount of PA6 added varied from 3 to 7, 15 and 25% wt.

After the extrusion, the obtained materials with a melt temperature of about 235°C were hot stretched using a take up roller at high draw ratios (the ratio between the transverse section of unstretched extrudate and the that of the stretched one). After the take-up roller, all the samples compression-molded at 180°C for 5 minutes and then cooled down at a rate of 40°C/min to obtain isotropic microfibrillar composites.

The characterization was conducted using the scanning electron microscopy to study the materials' morphology, DSC to analyze their thermal characteristics. As usual, also wide-angle X-ray scattering was employed to study the effects of isothermal crystallization, tensile tests were conducted to investigate the tensile properties of compression-molded specimens, both before and after isothermal crystallization. Using a parallel-plate geometry rheometer, the linear viscoelastic behavior of the samples was tested at 180°C, an intermediate temperature between the two  $T_m$  of PLA and PA6. Finally, a batch foaming process was applied to evaluate the effects of this process on the microfibrillar composites.

After extrusion, the unstretched blends presented a PA6 reinforcing phase with a spherical shape and a diameter ranging from the submicronic (if the content of PA6 was of 3 or 7%wt) to micronic sizes (for PA6 contents from 15 to 25%wt). The PA6 assumed the shape of microfibrillar structures after the hot-stretching process with the average diameters shown in Figure 73 and depending on the amount of PA6 contained in the composite. The increase in the amount of PA6 brought to an increase in the average diameter, that passed from 198 nm with the concentration of 3%wt of PA6 to 233 nm with 25%wt of PA6.

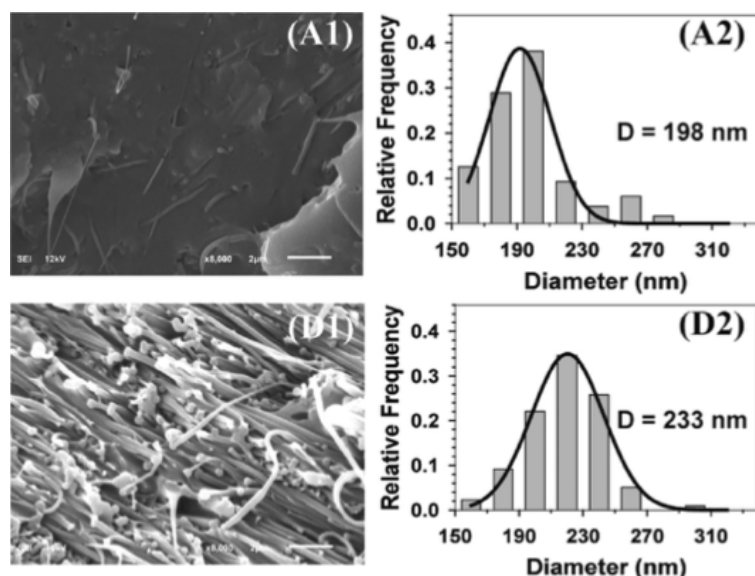


Figure 73. Increase in the average diameter due to the increase in PA6 amount.

The total absence of debonding between the matrix and the reinforcement indicates an effective load transfer from PLA to PA6 phases during the stretching process. Furthermore, the microfibrils appeared to have very high aspect ratios and an excellent dispersion in the PLA matrix without the presence of any agglomeration, event at higher PA6 concentrations.

To better analyze their aspect ratio, a sample containing 3%wt of PA6 underwent the etching process (Figure 74). The SEM image of its surface evidenced a highly entangled network of PA6 microfibrils, that confirmed their high aspect ratios and flexibility.

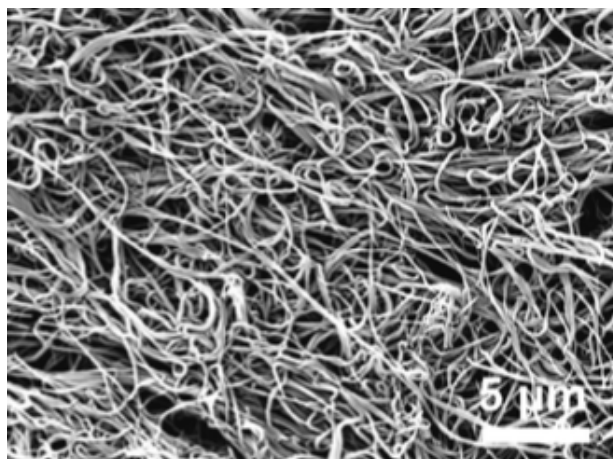


Figure 74. PA6 fibrils after the etching process to better analyze their aspect ratio.

Another interesting thing that has been observed is that, for high PA6 contents (25%wt), the fibrils result to be highly oriented, while in the other cases, for lower PA6 concentrations, they result to be randomly oriented, giving the composite an isotropic behavior. The different disposition of the fibrils at higher PA6 concentrations is due to the fact that, in this last case, there is a notable increase in the material viscosity and the PLA molecules have a reduced mobility. During compression molding, then, PA6 microfibrils are inhibited from reorienting, as the scheme in Figure 75 clearly explains.

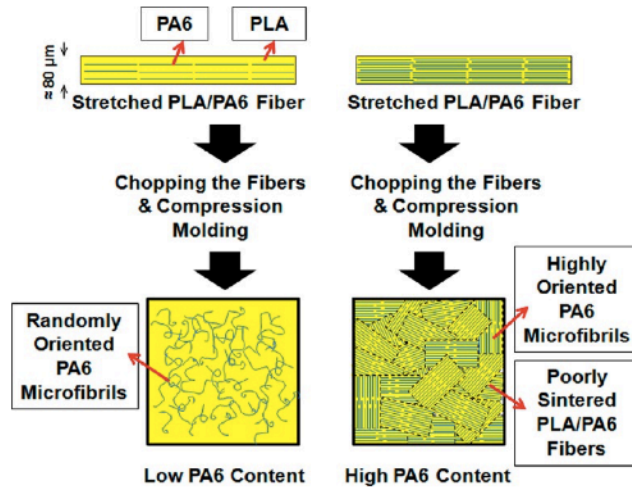


Figure 75. Different disposition of the fibrils depending on the PA6 concentration.

As far as the tensile properties are concerned, it has been observed that the reinforcing phase with a spherical shape does not improve neat PLA's tensile properties and this is confirmed by the DSC and WAXS analysis that state the slow crystallization kinetics of these materials. When the reinforcing phase has a fibrillar shape, instead, the tensile properties of the MFC are significantly improved with respect to the PLA's. For example, only with the addition of 3%wt of PA6, PLA's tensile modulus increased by 38%. The most satisfying behavior was observed with the 15% wt of PA6 but it must be noted that the addition of PA6 25%wt causes a big drop in the composite's modulus (Figure 76) and this is due to the structure of such composites described above and in Figure 75.

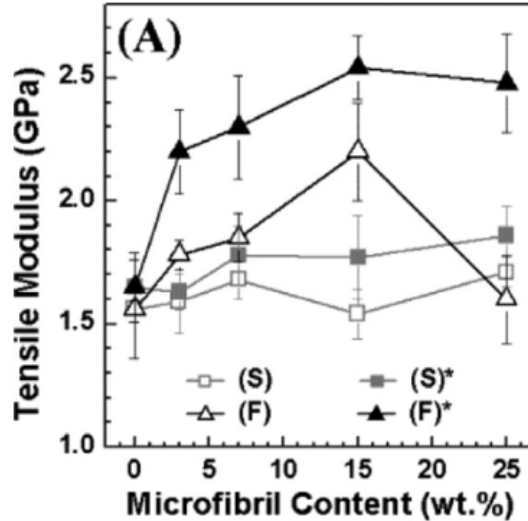


Figure 76. tensile modulus as a function of PA6 concentration.

Finally, to have an idea of the microstructure of the composites, the analysis of the viscoelastic behavior is very useful. As Figure 77 shows, the addition of 3%wt of fibrillar PA6 to the matrix is responsible of an increase in the storage modulus  $G'$  of three orders of magnitude. This indicates the notably improved elastic behavior of the composite once that even a very small amount of PA6 is added. Such an increase confirms the presence of a physically entangled network formed by the interactions of PA6 fibrils and this phenomenon is called rheological percolation.

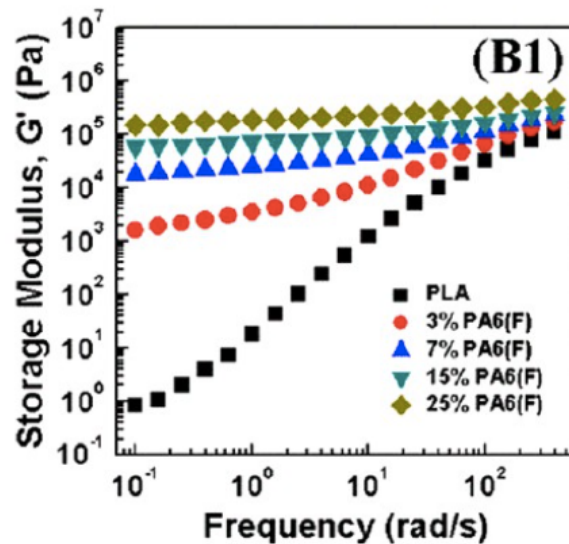


Figure 77. Storage modulus as a function of angular frequency.

Another study that analyzed the PLA/PA microfibrillar composites was conducted by García-Masabet et al. [11]. In particular, they investigated the effect that processing conditions have on the morphology of a composite material composed by 70% of PLA and 30% PA6. The screw rotation speed and the take-up velocity responsible of the different draw ratios were varied in order to analyze the efficiency of micro-fibrillation of PA.

To conduct this study, two different PLA were used:

- Neat PLA;
- Rheologically modified PLA produced by reactive extrusion with a higher melt elasticity.

while the dispersed phase used was constituted by bio-based PA10.10

The blends with two different matrices were produced by a melt mixing in an intermeshing co-rotating twin-screw extruder with a temperature profile of 145, 160, 180, 190, 200, 205 and 215°C. Two different speeds were adopted in order to study the effect that the shear rate had on the final morphology, and they were 30 and 100 rpm. Then, three different draw ratios were searched, and their values were 0 (no stretch), 1 and 3. In order to obtain them, three different take-up velocities were applied.

The characterization was conducted using a rheometer, a scanning electron microscopy, and a thermo-mechanical analysis.

As it can be seen from the SEM analysis (Figure 78), the modified PLA facilitates the creation of PA microfibrils even without hot stretching, which means with a draw ratio of 0. This means that the elasticity of the modified PLA was high enough to transmit the stresses generated during the flow to the PA dispersed phase and to deform it into fibrils. In the case of a matrix composed by neat PLA, instead, its elasticity is not able to transmit a stress that is bigger enough to deform the reinforcing particles.

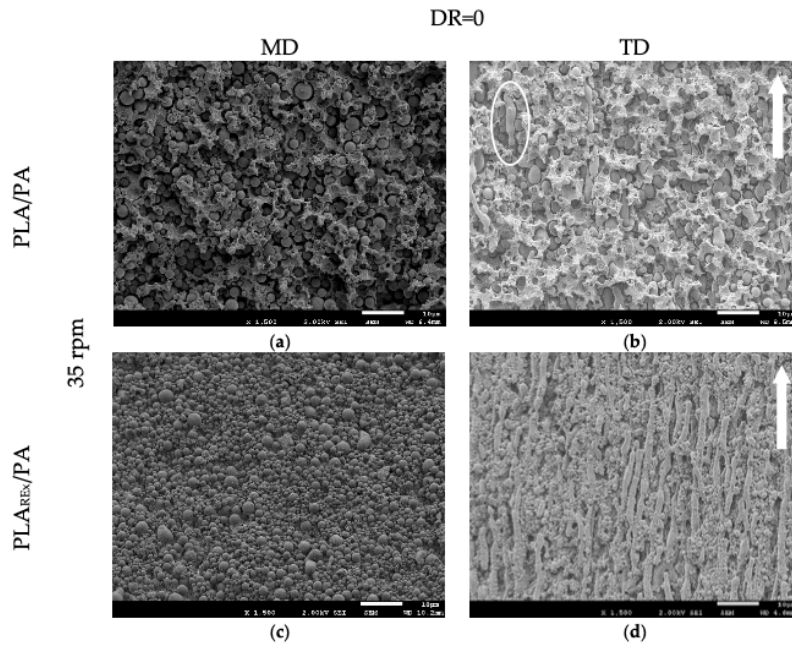


Figure 78. SEM images that prove how the modified PLA facilitates fibrils formation.

Concerning the PLA/PA composites, the aspect ratio of the fibrils created at low draw ratio (for example, DR=1), decreased with the increasing of the screw rotation speed as shown in Figure 79. This can be due to the fact that, in these extrusion conditions, it is more likely that PA particles coalesce in the die region and form bigger droplets. This provokes the formation of fibrils with a larger diameter under the same stresses generated by the take-up speed applied. The increase of the draw ratio up to 3, causes the increase in the aspect ratio of the fibrils in all the composites and the narrowing of the diameters' distributions. This effect is more remarkable in the modified PLA matrices.

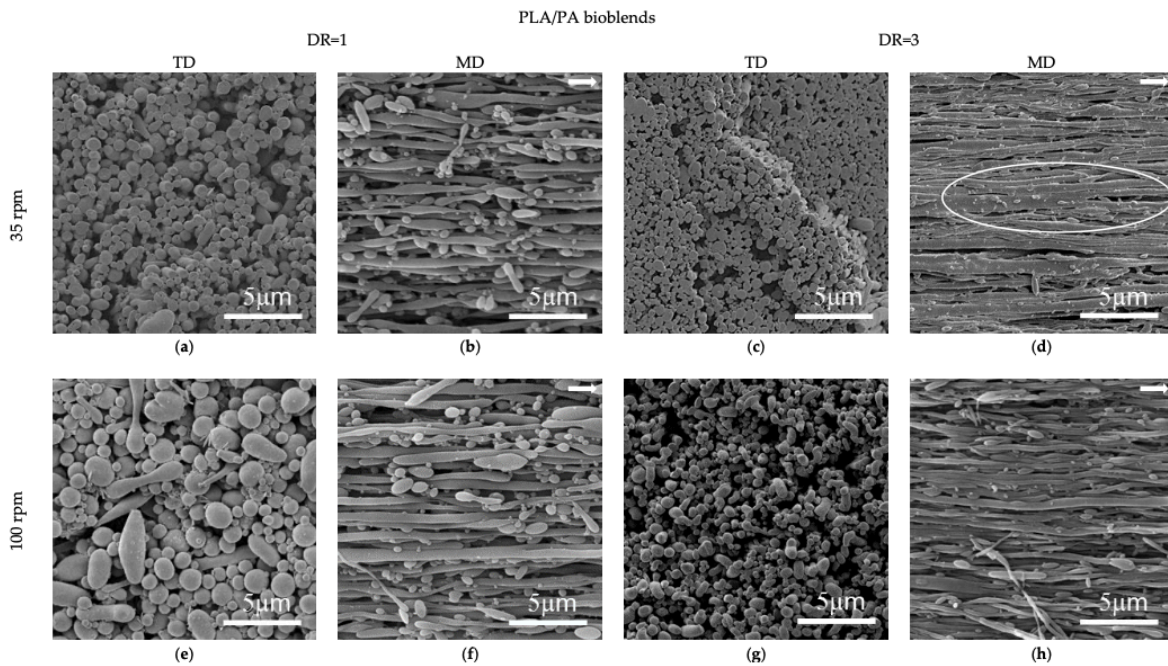


Figure 79. Decrease in the fibrils' aspect ratio due to high screw speed rotation.

The dynamic thermal-mechanical analysis, finally, demonstrated that the addition of PA microfibrils to the neat PLA matrix provoked an increase in the composite's storage modulus  $G'$  (also called  $E'$ ) between 500% and 1300% with respect to PLA alone, and between 1300% and 1600% in the case of modified PLA.

### 1.5 Fibrils in PC

The last material used to produce fibrils that has been analysed in the present work is polycarbonate PC. In particular, two scientific papers were taken into consideration and both of them coupled PC with high density polyethylene HDPE. Both of them were written by Xu et al.

In the first one [2], the composite obtained from the coupling of PC and HDPE was studied in order to understand the effective properties of this new material. PC and HDPE have two different viscosities, fact that leads to high values of viscosity ratio, which is not recommended when the expected result is fibrillation. Nonetheless, the morphological observations carried out have shown well-defined PC in the matrix. These fibrils had different diameters and were coarser and denser in the core material and thinner while moving towards the surface.

The composite materials were produced by a single screw extruder, with a rotation speed of 65 rpm and a temperature profile ranging from 190 to 280°C. Then, the extrudate underwent hot stretching with a take-up device made of two pinching rolls to promote the fibrils formation. Different hot-stretching ratios were adopted by varying the speed of the take-up device. The hot-stretching ratio (HSR) is defined as the ratio between the transverse section of the die and the transverse section of the extrudate. Quenching was applied as a final step.

The melt flow rate (MFR) of the obtained materials was widely employed to study the rheological properties of the polymer. To determine the MFR of the materials MFR-400 machine was used with a range of temperatures from 170 to 270°C and a constant load of 98 N. After reaching the steady flow, five samples were cut to obtain an average value. Also, the relationship between viscosity and shear rate was calculated using a high-pressure capillary rheometer. Furthermore, after the production process the specimens were frozen in liquid nitrogen for 10 minutes, broken by impact and then studied by scanning electron microscope.

Due to the fact that PC has viscosity much higher than that of HDPE, after the only extrusion PC particles still maintain a spherical morphology, especially in the bulk material. That is the reason why a hot stretching step is applied. As shown in Figure 80 after this last step, the blended material clearly shows microfibrils.

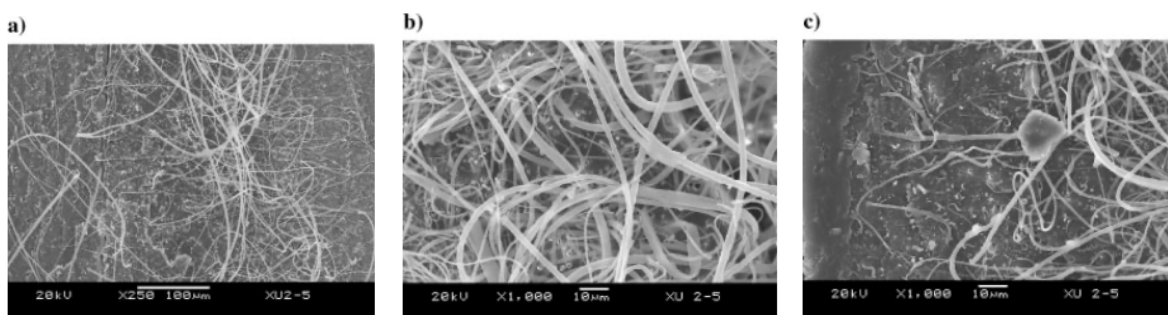


Figure 80. Fibrils formed after hot stretching in PC dispersed phase.

From these images, also the gradient of fibrils' concentration can be seen: Figure 80a shows the whole aspect of the sample, while Figure 80b presents a zoom on the core layer and Figure

80c the surface layer. It is evident that in the core zone the amount and thickness of the fibrils is much higher than in the surface area. This gradient is mainly due to the initial non-uniform distribution of the PC particles after extrusion.

Furthermore, HSR is another important factor that controls the fibrils' morphology. The higher the hot stretch ratio, the finer and denser the microfibrils, the higher the plastic deformation of the PC particles. HSR=1 (that is absence of hot stretch) corresponds to a spherical morphology of PC particles. So, the HSR must be high but not too much in order not to provoke the fibrils breakup. The example of HSR=6, that is a reasonable value in order to obtain fibrils, is reported in Figure 81.

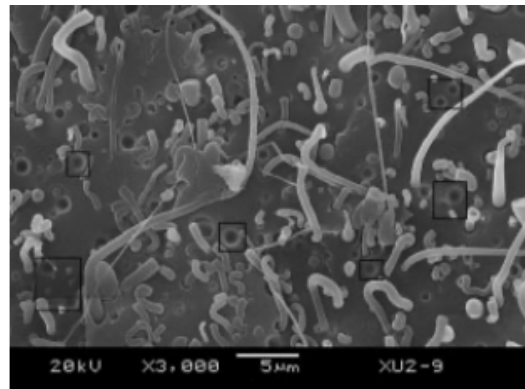


Figure 81. SEM image of the effect of HSR=6.

Concerning the MFR of these composites, it has been observed that this parameter decreases linearly with the increase of PC concentration, until it reaches a constant value when the PC concentration exceeds 20%wt (Figure 60). This is due to the fact that PC does not plastically flow but can only be deformed into fibrils. The increase in its concentration leads to the inhibition of the blend's flowability.

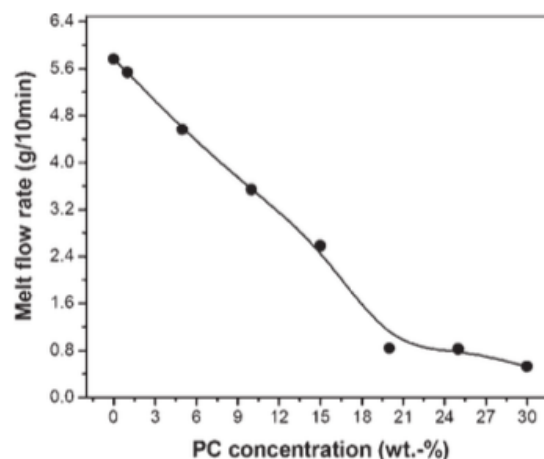


Figure 82. Melt flow rate as a function of PC concentration.

Finally, the effect of shear rate on the microfibrillar composites was investigated with different concentrations of PC at 170°C. The obtained curves reported in Figure 82 confirms the pseudoplastic behavior of the materials, with a decrease in the viscosity when the shear rate increases. The apparent viscosity of microfibrillar blends increased with the increased amount of PC for a same shear rate. The viscosity is higher for lower shear rates (Figure 83).

Microfibrils and HDPE molecules here, in fact, are not completely oriented in the flow direction. For higher shear rate values, the PC microfibrils, that are flexible, are found to be in the flow direction and so their effect on the viscosity becomes weaker. This is the reason why high shear rates are suitable for this kind of blends.

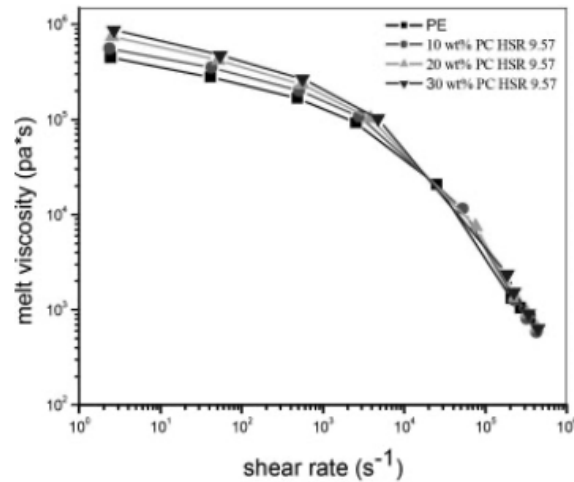


Figure 83. Melt viscosity as a function of shear rate.

The last article analyzed, instead, compares the effect of the addition of PC and PET fibrils to a HDPE matrix. The main difference is that while PET is a semicrystalline polymer, PC is an amorphous one. These two materials, then, exhibit different influences on the rheological behaviors of the blends. What is unexpected is the fact that the length/diameter ratio of the obtained microfibrils after the hot stretch ratio has an opposite effect on the rheological behavior of the two blends. In fact, the stretched PET/HDPE presents higher viscosity with respect to the unstretched blend and the opposite situation is verified with the PC/HDPE composite.

The blends were produced using a single screw extruder with the same temperature profile, that was 190, 250, 275 and 280°C, from the hopper towards the die, the rotation speed was kept at 65 rpm. The extrudate, as before, was stretched by a take-up device with two pinching rolls to promote the fibrils formation.

To observe the PET/HDPE samples obtained, the HDPE was removed using hot xylene at 130°C as an etchant, while the PC/HDPE composites were fractured as mentioned in the previous article. The surfaces were then analyzed using a scanning electron microscopy.

As Figure 84 demonstrates, both the SEM images of the blends present well-formed fibrils with diameters that vary from less than 0,5 to several  $\mu\text{m}$ .

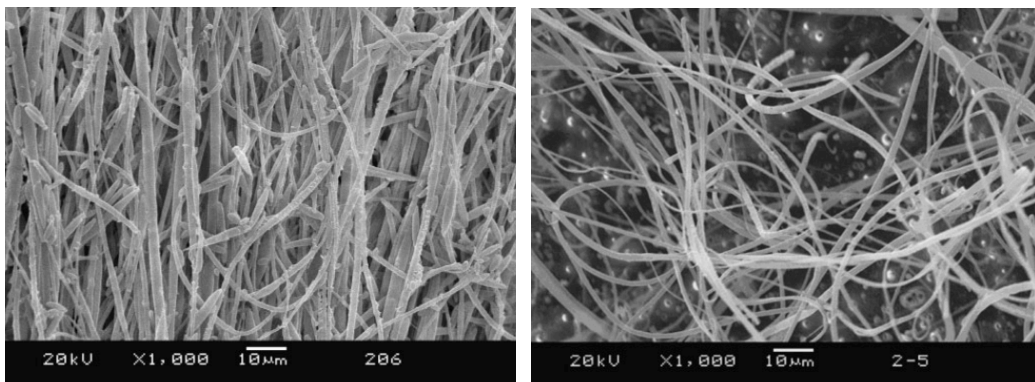


Figure 84. SEM images of the PC/HDPE and PET/HDPE blends.

As the graph in Figure 63 presents, both the microfibrillar blends have a pseudoplastic behavior, and this is confirmed from the fact that the viscosity decreases with the increase in the shear rate. What can be said, in any case, is that for PET/HDPE composites, the apparent viscosity increased in a more remarkable way with the increase of the reinforcement concentration with respect to the PC/HDPE composites. This phenomenon can be explained considering that PC fibrils are more flexible than the PET ones, and this leads to an easier deformation and orientation during melt flowing.

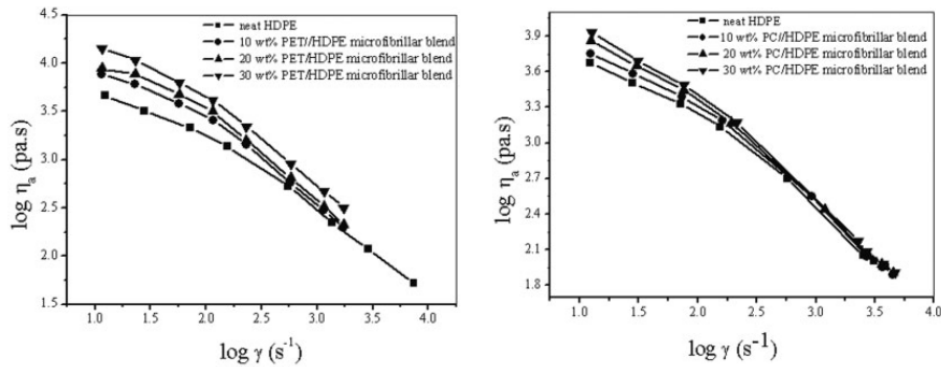


Figure 85. Variation of viscosity as a function of shear rate with the increasing concentrations of PC and PET.

This phenomenon can be due to the different stiffness values of PET and PC at the temperature used during the tests (170°C). Being a semicrystalline polymer, PET has a higher melting temperature (265°C) and, therefore, PET fibrils are still solid at the processing temperature and still have a high mechanical strength. PC instead, is an amorphous polymer, and is in an elastomeric state at 170°C. That is why PC microfibrils are more flexible than PET ones and this leads to the fact that PC fibrils have a weaker resistant effect on the flow melt. As it can be seen from Figure 85, PET and PC concentrations have an effect on the viscosity that is more remarkable at low shear rates. In this case, in fact, microfibrils are not oriented and the probability that the collision and entanglement between fibrils happens is much higher that at low shear rates.

Considering the effect of stretching on microfibrillar blends viscosity, it is interesting to note that it has an opposite effect in the case of PET/HDPE and PC/HDPE blends. In fact, while after stretching, PET/HDPE presents a higher viscosity with respect to unstretched composite, the opposite situation is verified for PC/HDPE blends. Again, this is probably due to the different stiffness possessed by the two materials. PC fibrils, in fact, at 170°C, are in a highly elastomeric state and are much more flexible that the PET ones, that have a very high modulus because of the greater number of crystalline domains.

Regarding the effect of the stretching ratio on the melt flow rate of the two materials, it has been observed that, increasing the HSR, the MFR for PET/HDPE composites decreases while the one for PC/HDPE materials increased (Figure 86).

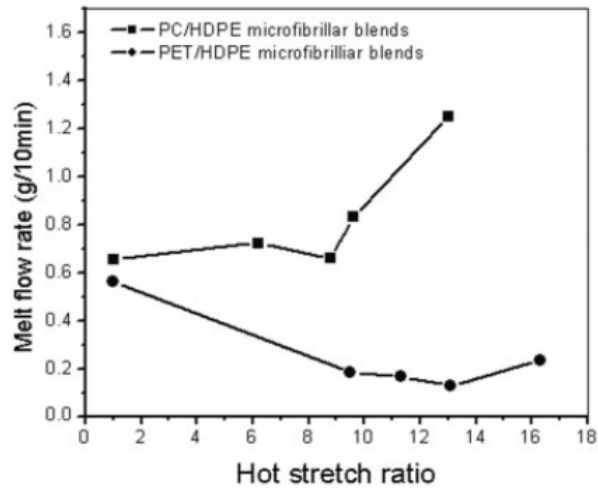


Figure 86. Melt flow rate as a function of hot stretch ratio.

The higher the hot stretch ratio, the bigger the ratio between the fibril's length and its diameter. But the thinner and longer microfibrils have opposite effects on the melt flow rate. In fact, if the longer fibrils have a notable entanglement density that inhibits flowing, the thinner ones are simpler to disentangle and orient, because of a lower stiffness. This last case promotes the flowing. These two behaviours counterbalance each other in the PET/HDPE blends, while in the PC/HDPE ones the second effect is the dominant one.

## 2. Extruders and Ludovic Software

### 2.1 Description of an extruder

To create all-composite materials, as previously explained, an extruder is needed during the mixing step, the first one of the process. Before describing how Ludovic Software operates, it is useful to remind the working principles of an extruder machine.

It is composed by (Figure 87):

- a) Extruder
- b) Die

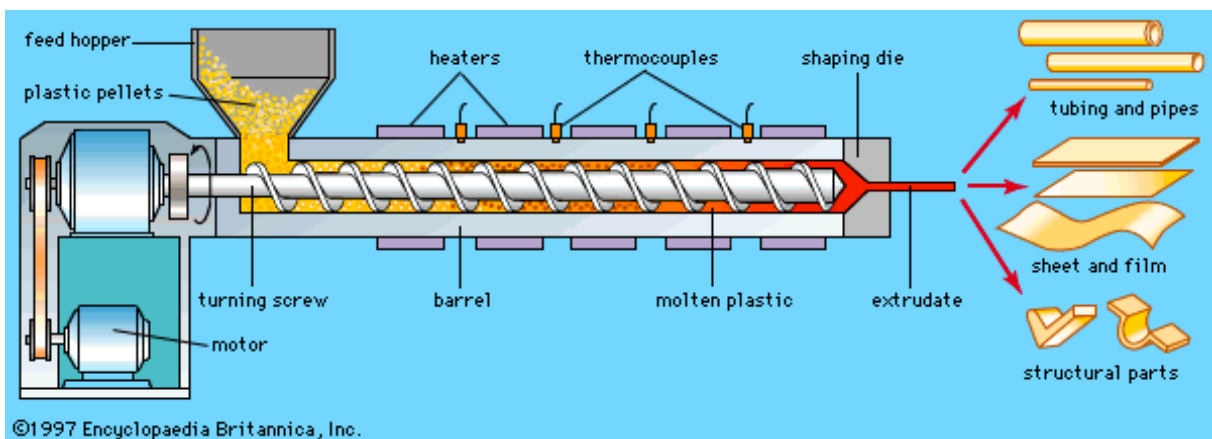


Figure 87. Scheme of an extrusion machine

The extruder is composed by a hopper, that contains the granules and powders of the materials to transform, and by a thermoregulated barrel (Figure 88).

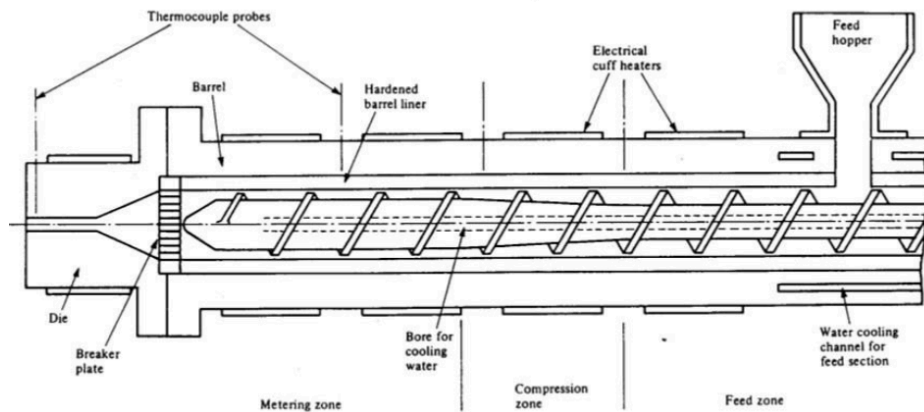


Figure 88. More detailed scheme of an extruder.

Inside the barrel there is the extrusion screw which plays a crucial role in:

- Transporting the solid polymers;
- Melting of the materials;
- Degassing;
- Mixing;
- Pumping of the obtained blend through the die.

In fact, the screw is composed by different kinds of elements, each one playing one of these roles.

Usually, to carry out the production of microfibrillar composites, a twin-screw extruder is employed,

Twin-screw extruders are used when the processes need higher performances compared to those obtained with the single screw ones. They are constituted by two open cylinders with an 8-shape in which the screws are located. The combination of two screws provides a multiplication of the shear stresses on the polymers inserted, ensuring an increased mixing of the chosen materials. Moreover, the twin screws can rotate in the same direction (co-rotating) or in the opposite one (counter-rotating) and a twin-screw extruder can be intermeshing or tangential, as shown in Figure 89.

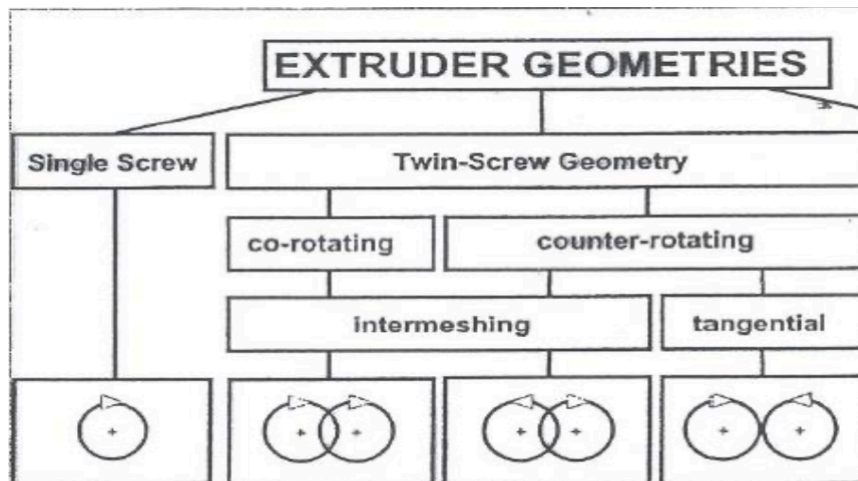


Figure 89. Possible properties of a twin-screw extruder.

The screw configuration that imparts the greatest shear stress is the intermeshing co-rotating one.

The screw profile can be modified according to the studied system and, in particular, it can be changed rearranging conveying elements, kneading elements and mixing elements. Their functions are those reported in the table in Figure 90.

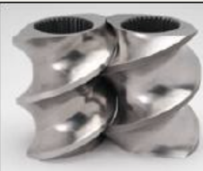
| Conveying Elements  | Kneading Elements   | Mixing Elements   |
|---|---|---|
| Conveying<br>Devolatilization<br>Metering   | Melting<br>Dispersive Mixing<br>Distributive Mixing   | Distributive Mixing   |
|     |     |  |

Figure 90. Functions of the different elements of a screw. [appunti TMP]

As far as the conveying elements are concerned, they are characterized by length and pitch and the bigger the pitch, the less efficient is the elements transport.

The kneading elements are characterized by the number of disks, the length, the leakage and the staggering angle. On the basis of the latter, these elements can be subdivided into three

classes: those with an angle of 30, 60 or 90°. The bigger the staggering angle, the smaller the conveying capabilities of the element and the greater the shear stress acting on the materials, which improves the mixing efficiency.

In both the cases of conveying and kneading elements, there can be backflow elements that hinder the material's flow and thus increase the residence time.

Once the screw profile has been defined, other parameters that can be set are:

- Screw speed rotation;
- Temperature profile;
- Flow rate;
- Barrel configuration (degassing elements, position of the feeding zone, etc).

## 2.2 Ludovic Software

Ludovic Software 7.0 has been created and improved by SC-Consultants and simulates a co-rotating twin-screw extruder. Although to perform its calculations several assumptions and simplifications must be done, it is quite precise as far as the results are concerned. Most of all, its velocity in concluding the simulations (only a few seconds) makes Ludovic a very useful tool in order to get an idea of what happens inside an extruder and of which are the suitable characteristics of the machine for a chosen product or recipe. All of it, in fact, can be done only with a personal computer, without any physical experiment and, therefore, with great time and cost saving.

As it will be further examined in the following pages, several parameters are required in order to allow the software to perform the simulations and, at the end, information about dissipated energy, torque, resident time distribution and several other quantities as a function of time or of axial coordinate  $x$  is returned.

In the following paragraphs, the models used by Ludovic to provide all the results are analyzed. All the formulas and information are taken from Ludovic User's Manual, provided by SC-Consultants. [12]

### 2.2.1 Molten polymers' behavior

Usually, molten polymers are described by a pseudo-plastic behavior, which means that the viscosity decreases with the increase of the shear rate, as shown by the following graph (Figure 91).

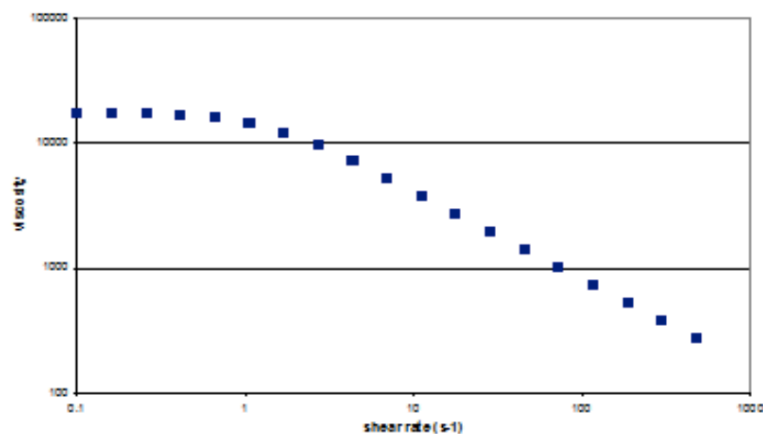


Figure 91. Viscosity as a function of the shear rate.

In fact, the viscosity is expressed by the formula

$$\eta = \frac{\tau}{\dot{\gamma}}$$

where  $\tau$  is the shear stress and  $\dot{\gamma}$  the shear rate.

An interesting aspect to note from the graph above (Figure 91) is that, for low values of the shear rate, the viscosity assumes a nearly constant value, which means that the melt has a Newtonian behavior. For this reason, the region in the graph at low shear rates is called Newtonian plateau.

In order to use the viscosity parameter during the simulations, two expressions that describe it are presented.

The first one is the Power Law. Its expression is

$$\eta = K\dot{\gamma}^{m-1}$$

in which  $m$  is the pseudo-plasticity index,  $K$  represents the consistency of the material and decreases when the temperature increases.

The second analytical description of viscosity is given by the Carreau-Yasuda law, written as

$$\eta = \frac{\tau_0}{\dot{\gamma}} + \eta_0(T)[1 + (\lambda(T)\dot{\gamma})^a]^{\frac{m-1}{a}}$$

Here,  $\tau_0$  is a yield response,  $\lambda$  is a typical time,  $\eta_0$  is the zero-shear viscosity,  $a$  represents the transition between the Newtonian zone to the power law one.  $\lambda$  and  $\eta_0$  are temperature-dependent parameters.

Another possibility a user has to describe his material's viscosity is the so-called Set of Points (SoP) rheological law. In this case, the general formula is

$$\eta = \eta(T, \dot{\gamma}, X)$$

but the user also has the chance to insert temperature, shear rate and viscosity data that he calculated himself, which is the approach used in this work.

### 2.2.2 Geometrical description of Ludovic's elements

The first important thing to underline when speaking about the software's geometry approximation is that, in this case, the two screws are considered fixed and it is the barrel that moves around them. The flow around the screws is assumed to be Newtonian, isothermal, incompressible and without gravity. To easily describe the flow equations, cylindrical coordinates are used in the screw, while, in the die, simple models are employed, depending on the die geometry.

To realize one whole simulation, Ludovic software proceeds discretizing the geometric model of the free volume in every element, from the screw to the die, and computing the thermo-mechanical flow.

To characterize the geometry of the screw-barrel system, three parameters are mainly considered:

- $R$ , the inner radius of the barrel;
- $C_L$ , distance between the screw axes (or centerline distance);

-  $\delta$ , leakage between screw and barrel.

Starting from these, the others can be easily calculated, in order to obtain the free volume on a transverse section  $S_F$  where the flow passes, and are:

$$R_1 = \text{screw internal radius} = C_L - R_2$$

$$R_2 = \text{screw external radius} = R - \delta$$

$$\psi = \text{intermeshing angle} = \cos^{-1} \left( \frac{C_L}{2 * R_2} \right)$$

$$S_B = \text{transverse section of the barrel} = 2(\pi - \psi)R^2 + C_L R \sin \psi$$

The free volume on a transverse section depends on the local screw elements and can be written as

$$S_F = \text{free volume on tranverse section} = S_B - 2S_S$$

in which  $S_S$  is the transverse section of the screw.

The simulation is carried out subdividing the channels where the molten polymers flow into a finite number of C-shaped chambers.

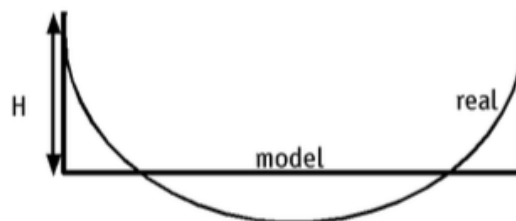


Figure 92. Model vs real chamber shape.

As shown in Figure 92, these chambers have a semi-circular aspect but, in order to simplify the equations, they are approximated with a rectangular shape so that their height can be calculated with the equation

$$H = R_2 - R_1$$

At this point, what occurs is an iterative process based on the evolution of the temperature inside the extruder.

Because of the fact that geometry plays a leading role in the mechanisms governing Ludovic's operations, it is interesting to analyze the features of the available screw elements, reported in Figure 93.



Figure 93. Screw elements available in Ludovic software.

- Right-handed and left-handed elements (screw elements in the image above)

They correspond to the conveying elements mentioned for real extruders and are characterized by length  $L$  and pitch  $B$ . They can have 1, 2 or 3 transport principles (Figure 94).

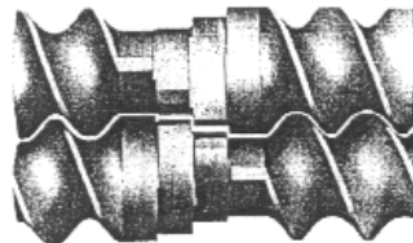


Figure 94. Right-handed screw element with some kneading disks (in the middle).

Once that the measures of these elements ( $L$  and  $B$ ) are known, it is possible to define:

- $W$  = width of a channel =  $\left(\frac{1}{n} - \frac{\alpha}{2\pi}\right) * B \cos \varphi$ 
  - where  $n$  is the number of flights,  $\alpha$  is the flight angle and  $\varphi$  is the angle between a pitch and a plan that is perpendicular to the screw axes.
- $n_C$  = number of C – chambers in an element =  $\frac{2n}{2n-1} * \frac{L}{B}$
- $L_C$  = Length of a C – chamber =  $\frac{2n-1}{n} * B$ .

- Kneading disks and Twisted Kneading disks (TKD)

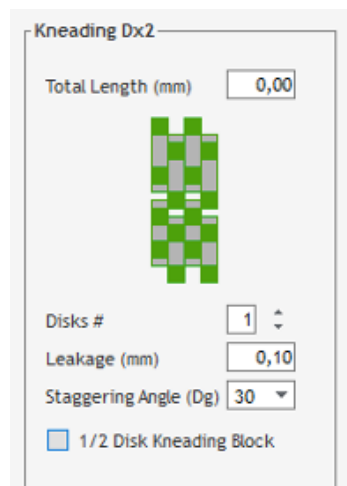


Figure 95. Parameters needed to define kneading elements.

To define these elements, the following data are needed (Figure 95):

- $m$ , number of disks;
  - $L_m$ , total length of one block;
  - Length of the leakage;
  - $\alpha_d$ , staggering angle;
  - Twist angle, for TKD only.
- Ring element  
It is used just to adjust the others along the screw and is defined by its radius  $R$  and its length.
  - TME element (Figure 96)

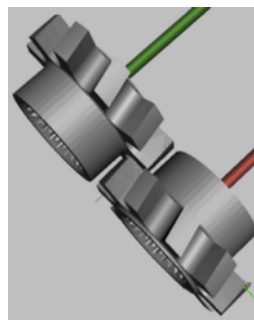


Figure 96. TME element

Composed by a set of rings and slits, it is mainly used to improve mixing distribution and dispersion ability during extrusion.

As far as the die is concerned, there are eight possible configurations, and these are subdivided into two classes:

- 1) “Tube shaped family”, where the geometry is defined by one radius  $R_H$ , like pipe (or tube), converging pipe, 8/0 element;
- 2) “Plate shaped family”, where the geometry is defined by half-height  $h$ , like slit, converging slit and fish tail.

The eight possible shapes for the dies are those reported below (Figure 97).

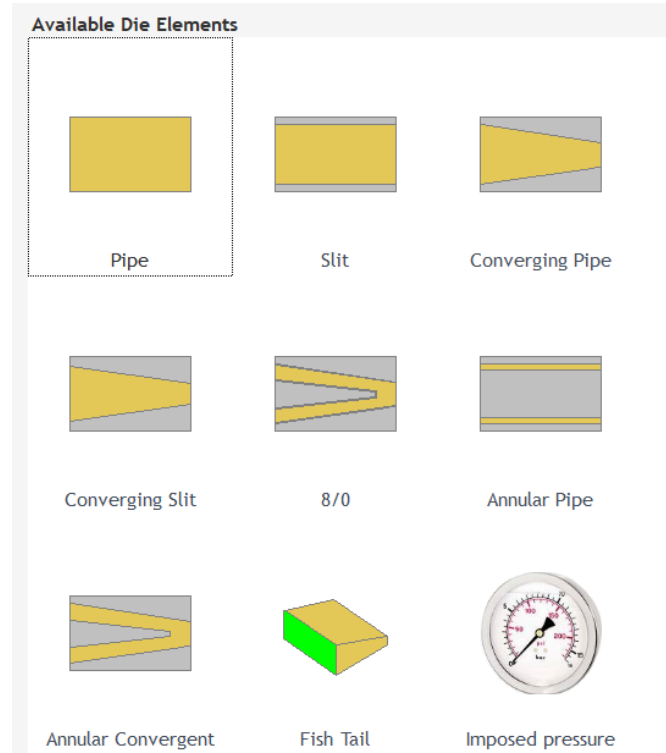


Figure 97. Possible die configurations.

### 2.2.3 Ludovic’s mechanical model for screw and die elements

It is important to underline the fact that, inside the C-chambers, Ludovic considers the axial coordinate  $x$  coincident with the screw axis and uses a cylindrical coordinates system. The velocity components are assumed independent from the axial coordinate and the flow along the radial direction is neglected. These approximations can be written as:

$$V_x = V_x(r, \theta)$$

$$V_r = 0$$

$$V_\theta = V_\theta(r, \theta)$$

$$p = p(x, r, \theta)$$

Now, the boundary conditions are defined, taking into account the fact that the viscous fluid generates a sticky condition at the wall, which implies that in correspondence to the internal radius of the screw  $R_1$  the velocity is zero. In any case, to take into account the sliding phenomenon, two factors are defined:  $\alpha$  and  $\beta$ . The first one is the sliding factor referred to the barrel, while the second is the sliding factor referred to the screw.

Regarding the right-handed and left-handed elements, the flow in these cases is analyzed using a 2D model where the channel section is considered to be perpendicular to the screw axis (Figure 98) and cylindrical coordinates are used.

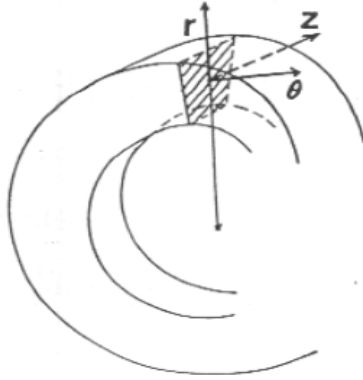


Figure 98. Geometry scheme for screw elements.

To evaluate the shear rate, an initialization of  $\dot{\gamma}$  and the combination of radial and angular velocity gradients,  $v_x(r)$  and  $v_\theta(r)$ , have been used. The exploited formula, written below, can be applied if the viscosity is fully determined and is assumed to be constant in each C-chamber (Newtonian approach).

$$\dot{\gamma}_0 = \omega \frac{R_2}{H}$$

So, it depends on the angular velocity  $\omega$ , external radius  $R_2$  and on the transverse section  $a$  of a channel,  $H$ . At this point, an iterative computation is carried out, with the viscosity continuously updated exploiting analytical laws or the Set of Points uploaded by the user. To evaluate the mean residence time, the following equation has been applied

$$RT = \frac{V_{free} * F_r}{Q}$$

in which  $Q$  is the volumic flow rate,  $V_{free}$  is the free volume in the screw-barrel system and  $F_r$  is a parameter called local filling ratio whose value is 1 for the kneading elements and lower than 1 for the screw ones, it depends on how filled an element is.

Things change when the intermeshing zone is considered. In this situation, in fact, the shear rate fully depends on the relative displacement of the twin screws and not on the screw-barrel's wall system. The geometry of this section is approximated using a portion of a tube and the velocity field is described as follows:

$$\begin{aligned} v_x &= 0 \\ v_r &= 0 \\ v_\theta &= v_\theta(r) \end{aligned}$$

As far as the kneading elements are concerned, the mechanical model is based on some assumptions:

- The free volume of the mixing element is completely filled with the molten polymer;
- The flow on the x-axis is due to the pressure drop on the same axes,  $\frac{dP}{dx}$  ;
- The mixing element is characterized by a notable width,  $\frac{dH(\theta)}{d\theta} \ll 1$ ;
- The velocity field is expressed by  $u = v_x, 0, v_\theta(r)$ .

The tangential velocity is calculated by the Navier-Stokes equation with four boundary conditions

$$\begin{aligned} v_x(R_1) &= 0 \\ v_\theta(R_1) &= 0 \\ v_x(R_2) &= 0 \\ v_\theta(R_2) &= R_2\omega \end{aligned}$$

and does not depend on  $\theta$ .

The peripheral pressure profile, instead, is evaluated providing a numerical iterative integration on a single channel.

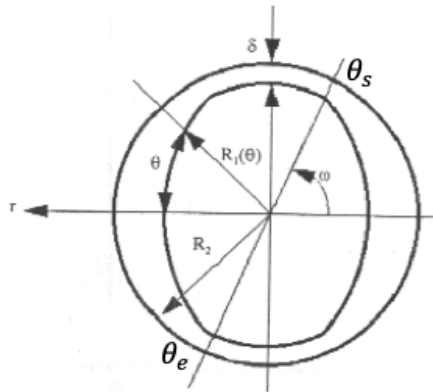


Figure 99. Kneading element's cross section.

The convergence is obtained when the condition  $p(\theta_e) - p(\theta_s)$  is reached. In Figure 99, a kneading element's cross section is shown and  $\theta_e$  and  $\theta_s$  can be distinguished.

According to this condition, the pressure that characterizes two symmetrical points of the element must be equal.

An approximate value of flow rate  $Q_\theta$ , permits to calculate the circumferential pressure gradient  $\frac{dp}{d\theta}$ . The obtained value of  $p(\theta_e)$  is then compared to  $p(\theta_s)$  and, if they do not coincide, the flow rate  $Q_\theta$  continues to be modified until this condition is satisfied.

One kneading element alone is not able to perform an axial flow, so, in order to obtain the conveying of the melt, several elements with a staggering angle  $\alpha_m$  are put together. An axial flow rate balance is performed applying the Stokes equation on all the kneading elements, in order to obtain the computation.

The last case of mechanical model application for a screw element is the TME. Ludovic subdivides it into two different parts: a slit element, governed by the Stokes equation, and a one-ring element with radius  $R_1$ . The result obtained from each one of these two components is divided by 2.

Proceeding with the description of the mechanical model in the die, it must be said that, in this case, only the axial velocity is considered. As mentioned before, there are two groups of flow and each one has its own boundary conditions, written below.

In particular:

Tube shaped group  $\rightarrow v_x(r) = 0$

Plate shaped group  $\rightarrow u(-h) = 0$  and  $u(h) = 0$ .

To properly estimate the flow inside the die, the resolution of partial derivative equations is needed, even if the geometry is simple. Ludovic adopts a simplified method that calculates global values and considers the system as a 1D section. Inside each section, the fluid is considered Newtonian, isothermal, incompressible and with an equivalent viscosity. Thanks to a Newtonian model the mean shear rate can be calculated, and the temperature is evaluated at the die exit.

To evaluate the pressure jump, two relationships are used according to the distinction on the basis of the shape elements mentioned above.

For the tube-shaped elements, the pressure drop has the formula

$$\Delta P = \frac{8\eta L Q}{\pi R_{eq}^4}$$

in which  $R_{eq}$  is the equivalent radius of the considered element, L is its length and Q the flow rate.

For the plate-shaped elements, instead, the pressure drop is given by

$$\Delta P = \frac{12\eta L Q}{W_{eq} (2h_{eq})^3}$$

in which  $W_{eq}$  and  $h_{eq}$  are, respectively, the equivalent width and the equivalent half-height of the considered element.

To evaluate the shear rate in the die and, in particular, to consider the pseudo-plasticity of the product, a correct equation is used in the case of simple elements (which means, no ring-shaped cone, 8/0 element and fish tail). So, if the viscosity is not determined by the user, the pseudo-plasticity coefficient m is calculated by Ludovic and is different from 1.

So, the shear rate for tubes and converging tubes is

$$\dot{\gamma} = 2 \frac{1 + 3m}{1 + 2m} * \frac{Q}{\pi R_{eq}^3}$$

and for plates and converging plates is

$$\dot{\gamma} = 2 \frac{1 + 2m}{1 + m} * \frac{Q}{W_{eq} h_{eq}^2}$$

In the other cases  $m=1$  and the above equation are consequently modified.

## 2.2.4 Ludovic's thermal model for screw and die elements

Ludovic's thermal model is based on the equilibrium between lost and generated energy. Because of the conduction that occurs in the barrels, in the die and (not always) in the screw, in fact, a certain amount of energy is lost, but, on the other hand, there is a transformation of mechanical energy into the thermal one due to viscous dissipation.

The applied principle to execute the calculation is the same for every screw and die element and combines four phenomena, among which two have already been mentioned. They are:

- 1) Mechanical dissipation  $\Delta T_{mec}$ ;
- 2) Conduction term  $\Delta T_{cond}$ ;

3) Kinetics drop of temperature  $\Delta T_{cinet}$ ;

4) Increase of temperature due to the presence of microwaves  $\Delta T_{micro}$ ;

If necessary, also the melting model of a very specific part of the extruder can be added,  $\Delta T_{melt}$ . So, the obtained equation is

$$\Delta T = \Delta T_{mec} + \Delta T_{cond} + \Delta T_{cinet} + \Delta T_{micro} + \Delta T_{melt}$$

and its application permits to calculate the temperature jump between an element and the one next to it.

Depending on which element is considered, if belonging to the die or to the screw, each  $\Delta T$  element is expressed by a different equation. The most useful ones are described.

The mechanical dissipation term for a screw element is expressed by the formula

$$\Delta T_{mec} = \frac{\dot{W}}{\rho C_p Q_v}$$

in which  $\rho$  is material's density,  $C_p$  is its heat capacity and  $Q_v$  the volumetric throughput.

$\dot{W}$  is the thermal power due to the dissipation of mechanical energy and depends on material's viscosity and shear rate. Its formula is

$$\dot{W} = \eta \dot{\gamma}^2$$

To evaluate the conduction temperature drop,  $\Delta T_{cond}$ , it is necessary to make a few premises. Screw and barrels have a constant temperature along the C-chambers. In order to properly calculate the temperature jump between two adjacent elements, the heat transfer flux is needed and it can be expressed in two different ways: either directly, using the heat transfer coefficients  $h_s$  for the screw and  $h_b$  for the barrel, or on the basis of the so called Nusselt number  $Nu$ , again for the screw or for the barrel. Their equations are reported below.

$$Nu_s = h_s \frac{(R_2 - R_1)}{k}$$

$$Nu_b = h_b \frac{(R_2 - R_1)}{k}$$

$k$  is the material's thermal conductivity, and the two  $h$  are the local transfer coefficients previously mentioned. Once that the heat transfer flux is defined, it is possible to calculate the power exchanged with the regulation system,  $\dot{Q}$ . It is expressed as follows:

$$\dot{Q} = h_s (T_s - \bar{T}) S_s + h_b (T_b - \bar{T}) S_b$$

where  $S_s$  and  $S_b$  are the transfer surfaces between material-barrel and between material-screw,  $\bar{T}$  is the material's mean temperature and  $T_s$  and  $T_b$  are the thermal regulation temperatures corresponding to a specific C-chamber.

Now, the conduction term can easily be written:

$$\Delta T_{cond} = \frac{\dot{Q}}{\rho C_p Q_v}$$

Concerning the melting term, it describes the heat transfer needed to pass from the solid to the liquid state, and is given by the formula

$$\Delta T_{melt} = \frac{\Delta t}{\rho_l C_{pl}} \left( \frac{3\varphi}{R} h_s (T_{sol} - T_{liq}) \right)$$

in which  $\varphi$  is the solid phase fraction,  $R$  is the size of the solid phase,  $h_s$  is the solid-liquid transfer coefficient,  $T_{sol}$  is the solid temperature and  $T_{liq}$  is the mean liquid temperature.

The last two terms,  $\Delta T_{micro}$  and  $\Delta T_{cinet}$ , will not be further analyzed because of the fact that, in the present work, there is no heat is provided by microwaves energy and there are not chemical reactions that occur during the extrusion process.

Finally, a few words must be spent on the die thermal model but there is not a specific discussion for die elements' thermal balance. The only important thing to note is that, for each element, the dissipated energy deriving from the viscous flow is given by the formula

$$\dot{W} = \eta \dot{\gamma}^2 * V$$

where  $V$  is the volume of the considered element and depends on its family.

In fact, for the tube-shaped group

$$V = \pi R_{eq}^2 L$$

while for the plate-shaped family

$$V = 2h_{eq} W_{eq} L$$

## 2.2.5 How to set a simulation with Ludovic software

A description of how to start and create a simulation is provided in this paragraph.

The first thing to do is the creation of a database once that Ludovic software has been opened. A database is composed by projects that, in their turn, contain all the simulations.

When a new simulation is created, it is necessary to set all the parameters needed in order to emulate the extrusion process and, to do this, the “Extruder” window must be opened, as shown in Figure 100.

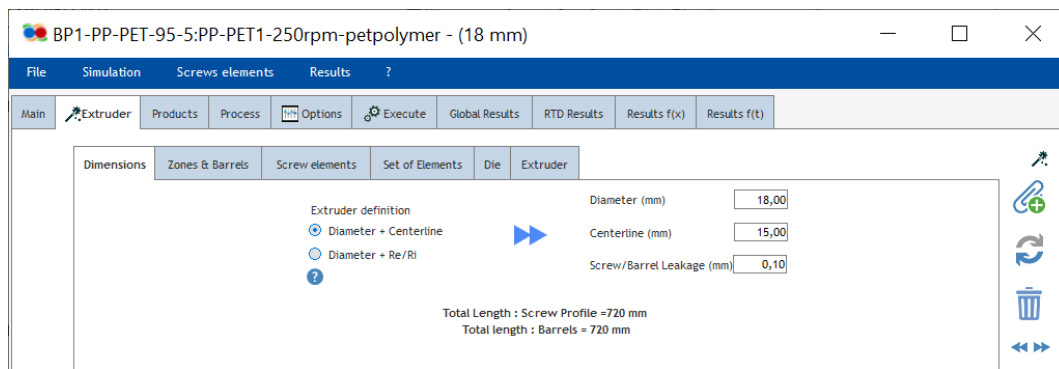


Figure 100. Extruder window in Ludovic software

As the image above displays, in this section the extruder's characteristics must be defined starting from the dimensions to zones&barrels, screw and die elements. Here, the user must build the machine selecting all the conveying/mixing/kneading/pipe/plate/etc elements that compose the screw and the die. "Set of elements" indicates a combination of elements that can be inserted all together to save time, while "Extruder" permits the upload of a pre-defined extruder, if available.

The following step is the definition of the products that the user intends to virtually insert into the extruder. To complete this procedure, the required data are those reported in Figure 101.

The screenshot shows a 'Product' configuration window with a 'Viscosity' tab selected. It contains input fields for the following parameters:

- Solid Phase:**
  - Heat Capacity (J/Kg/°C)
  - Density (kg/m3)
  - Thermal Conductivity (W/m.K)
- Liquid Phase:**
  - Heat Capacity (J/Kg/°C)
  - Density (Kg/m3)
  - Thermal Conductivity (W/m.K)
- Other Parameters:**
  - Melting Temperature (°C)
  - Melting Enthalpy (KJ/Kg)

Figure 101. Required parameters to define a product.

The viscosity can be defined either by choosing one of the laws already available in Ludovic software, or uploading the user's own data for temperature, viscosity and shear rate.

Now the process form must be filled in. Among the other data, it requires the thermal transfer coefficient between material and die, material and barrel, material and screw (Figure 102, thermal exchange box).

The screenshot shows the 'Extruder Settings' window with the following sections:

- Extruder Settings:**
  - Rotation Speed (Rpm): 120
  - Screw Temperature (°C): [input field]
- Thermal Exchange:**
  - Thermal Exchanges Coefficients
  - Thermal Exchange / Die (W/m2.K): 500,0
  - Thermal Exchange / Barrel (W/m2.K): 1.000,0
  - Thermal Exchange / Screw (W/m2.K): 0,0
- Zones Settings Table:**

| Position (n° Screw elt) | Added products Temp (°C) | Total F Rate (kg/h) | Product / Recipe in extruder |
|-------------------------|--------------------------|---------------------|------------------------------|
| 1                       | 25                       | 3,00                | PP70-PET30_ARTICOLO          |
| 20                      | 0                        | 2,98                | PP70-PET30_ARTICOLO          |
| 11                      | 0                        | 2,95                | PP70-PET30_ARTICOLO          |
- Dies Temperature Table:**

| n° | Temp (°C) |
|----|-----------|
| 1  | 280       |
| 2  | 280       |
| 3  | 280       |
| 4  | 280       |
| 5  | 280       |
- Barrels Table:**

| n° | Temp (°C) | Thermal Exchange |
|----|-----------|------------------|
| 1  | 255       | 1.394,38         |
| 2  | 260       | 1.394,38         |
| 3  | 265       | 2.015,68         |
| 4  | 270       | 2.015,68         |
| 5  | 270       | 2.015,68         |
| 6  | 270       | 2.015,68         |
| 7  | 270       | 2.015,68         |
| 8  | 280       | 2.015,68         |

Figure 102. Information needed to fill in the process window.

As mentioned before, the thermal exchange can be described either by the thermal exchange coefficients (like in the example above) or by the Nusselt coefficients.

Furthermore, in this step the user must define the temperature profile both in the barrel and in the die.

Once that all the needed parameters have been inserted, the simulation can be executed. Due to the fact that in the feeding zone the screws are not totally filled, it is impossible to calculate the pressure here. That is the reason why Ludovic software starts the computation from the die and proceeds towards the hopper. A die exit temperature is set, and, from it, the computation of the whole pressure and temperature profiles take place, until the melting point is reached. Unless the user imposes a melting point, Ludovic estimates it in correspondence to the first restrictive and totally filled element, such as left-handed elements, kneading disks and reverse screw. The temperature that Ludovic reaches at this point is compared to the product's melting temperature and, if they do not coincide, the simulation is launched again until convergence is reached.

The obtained results are subdivided into four categories:

- Global results, where a pie chart shows the amount of energy dissipated by viscous phenomena and by the processing of the material.
- Residential Time Distribution (RTD) results, with the possibility of seeing the integrated RTD curve as well.
- Results  $f(x)$ , where all the different parameters can be displayed as a function of the  $x$  coordinate, that represents the direction of the screw profile.
- Results  $f(t)$ , where temperature, pressure, shear rate and free volume can be plotted as a function of time.

### 3. Materials and methods

In the present chapter, the characterization methods, the used materials and the selected Ludovic software settings are presented. In order to obtain all the information required by the software to launch the simulation, the chosen polymers, PP and PET, underwent two kinds of characterization:

- 1) Differential scanning calorimeter (DSC) analysis to obtain polymers' melting temperatures and melting enthalpies. The obtained results were extrapolated thanks to the TA Universal Analysis software.
- 2) Rheometer analysis in order to evaluate the trend of the material viscosity as a function of the shear rate, at different temperature values to create the so-called Set of Points, one of the methods accepted by Ludovic to characterize materials' viscosity.

First of all, the used materials will be presented, then the characterization methods and, finally, the input settings to launch the simulation.

#### 3.1 Materials

The polypropylene (PP) used as the matrix, Moplen HP500N, was provided by LyondellBasell Industries and is a homopolymer generally used for injection molding applications, with considerable flow and stiffness. Its main properties are reported in the following table (Table 1).

| Physical Properties         | Nominal Values         | Test Methods  |
|-----------------------------|------------------------|---------------|
| Melt Flow Rate              | 12 g/10min             | ISO 1133-1    |
| Density                     | 0.90 g/cm <sup>3</sup> | ISO 1183-1    |
| Mechanical Properties       |                        |               |
| Tensile Modulus             | 1400 MPa               | ISO 527-1, -2 |
| Tensile Stress at Yield     | 35 MPa                 | ISO 527-1, -2 |
| Tensile Strain at Yield     | 10%                    | ISO 527-1, -2 |
| Impact Property             |                        |               |
| Charpy Impact Strength      | 4 kJ/m <sup>2</sup>    | ISO 179       |
| Thermal Properties          |                        |               |
| Heat Deflection Temperature | 95°C                   | ISO 75B-1, -2 |

Table 1. Polypropylene properties

By DSC analysis, PP melting temperature and melting enthalpy were calculated. Differential scanning calorimetry analyses were performed using a QA1000 TA Instrument apparatus (TA Instrument Inc., Waters LLC, USA). All the experiments were performed under dry N<sub>2</sub> gas (flow: 50 mL/min) using samples of about 10 mg in sealed aluminum pans.

In particular, PP underwent the following cycle:

- 1) heating from -50 °C to 220 °C at 10 °C/min;
- 2) cooling down to -50 °C at 10 °C/min;
- 3) heating from -50 °C to 220 °C at 10 °C/min.

Using TA Universal Analysis software, the curve obtained during the third cycle (i.e the second heating scan) was selected and, thanks to an integration tool, the two parameters were calculated (Figure 103).

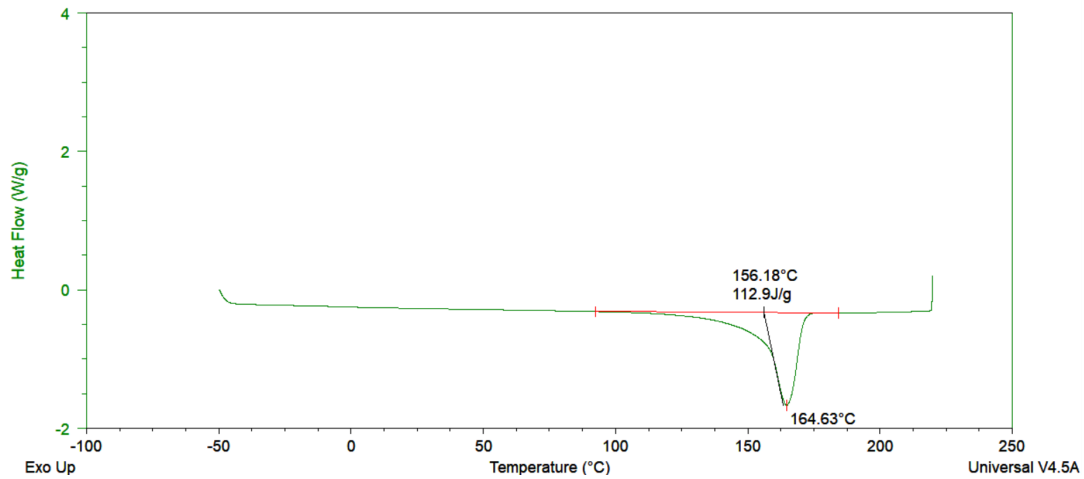


Figure 103. DSC analysis of PP Moplen HP500N

By rheometric measurement, instead, the set of data regarding PP shear rate and viscosity were obtained (Figure 104). The instrument used was ARES (TA Instrument, USA) strain-controlled rheometer in parallel plate geometry (plate diameter: 25 mm). The complex viscosity was measured performing frequency scans from  $10^{-1}$  to  $10^2$  rad/s at different temperature values (namely, 190, 210 and 230 °C for PP), under nitrogen atmosphere to avoid polymer degradation. The strain amplitude was selected for the sample in order to fall in the linear viscoelastic region, assessed for this material from preliminary strain sweep measurements. It is important to highlight that, both the polymers selected for this study, being linear homopolymers with simple macromolecular architecture, follow the Cox-Merz rule. This empirical rule predicts the correspondence between the shear rate dependence of the shear viscosity and the frequency dependence of the complex viscosity; for this reason, complex viscosity values coming from oscillatory dynamic tests can be used for the characterization requested by Ludovic.

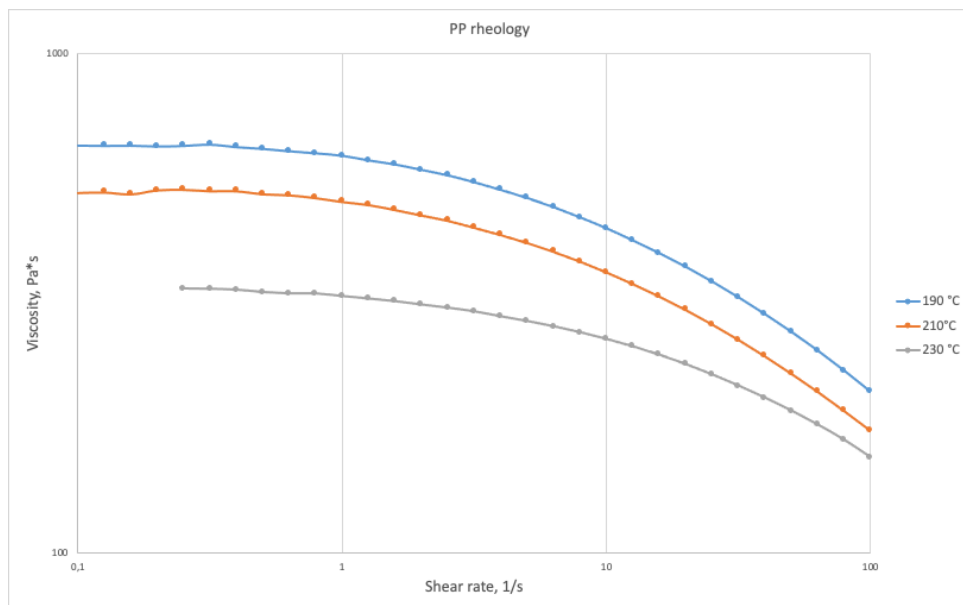


Figure 104. Viscosity as a function of shear rate for PP Moplen HP500N

The parameters requested by Ludovic that cannot be measured through experimental tests have been taken from the literature. The complete set of data entered in Ludovic Software is shown in Table 2.

| Molpen HP500N PP     |                       |
|----------------------|-----------------------|
| Solid Phase          |                       |
| Heat Capacity        | 1687 J/kg*°C          |
| Density              | 900 kg/m <sup>3</sup> |
| Thermal Conductivity | 0,118 W/m*K           |
| Liquid Phase         |                       |
| Heat Capacity        | 2931 J/kg*°C          |
| Density              | 770 kg/m <sup>3</sup> |
| Thermal Conductivity | 0,118 W/m*K           |
| Melting Temperature  | 164,63 °C             |
| Melting Enthalpy     | 112,9 kJ/kg           |

Table 2. PP input properties

As far as the PET is concerned, in the present study flakes coming from mechanical recycling operations of bottles have been used

Similarly to the PP, its melting temperature and enthalpy were calculated by DSC analysis, with the same apparatus described above. The applied cycle was:

- 1) a first heating step from 25 °C to 300 °C at 10 °C/min;
- 2) a cooling ramp to 25 °C at 10 °C/min;
- 3) a heating ramp from 25 °C to 300 °C at 10 °C/min.

Again, the two parameters were extrapolated using TA Universal Analysis software (Figure 105).

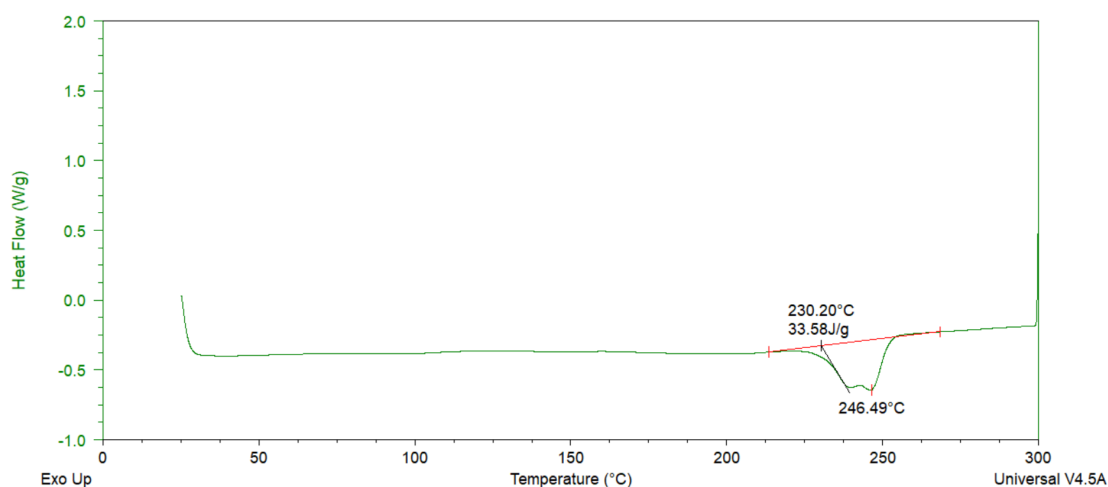


Figure 105. DSC analysis of PET.

With the same ARES parallel plate rheometer, and the same procedure, PET complex viscosity was measured applying frequency scans from  $10^{-1}$  to  $10^2$  rad/s at 260, 270 and 280 °C temperature values under nitrogen atmosphere (Figure 106).

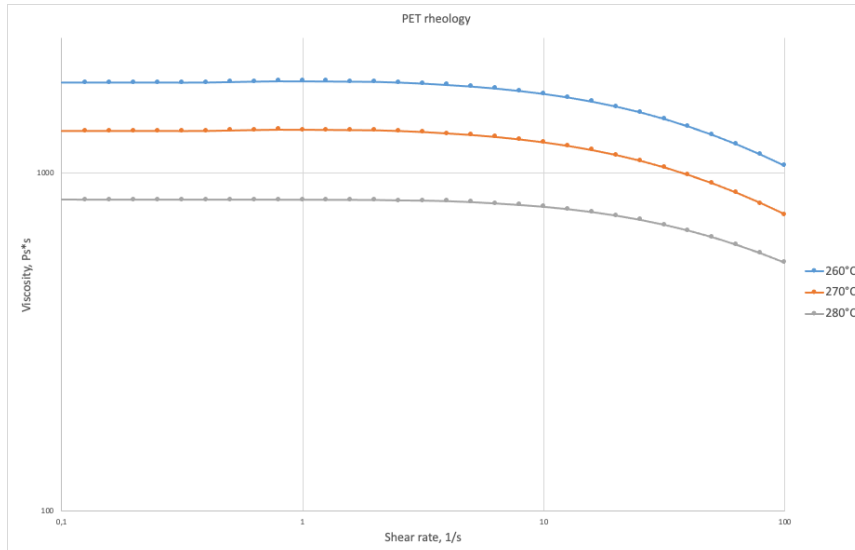


Figure 106. Viscosity as a function of shear rate for PET

The set of input data for Ludovic is reported in Table 3.

| PET                  |                        |
|----------------------|------------------------|
| Solid Phase          |                        |
| Heat Capacity        | 1100 J/kg*°C           |
| Density              | 1380 kg/m <sup>3</sup> |
| Thermal Conductivity | 0,22 W/m*K             |
| Liquid Phase         |                        |
| Heat Capacity        | 1589 J/kg*°C           |
| Density              | 1200 kg/m <sup>3</sup> |
| Thermal Conductivity | 0,52 W/m*K             |
| Melting Temperature  | 246,49 °C              |
| Melting Enthalpy     | 33,58 kJ/kg            |

Table 3. PET input properties

### 3.2 Setting of Ludovic simulations

The first simulation was conducted reproducing the performance of the Leistritz ZSE 18 HP machine, equipped with two screws whose profile as reported in Figure 107.

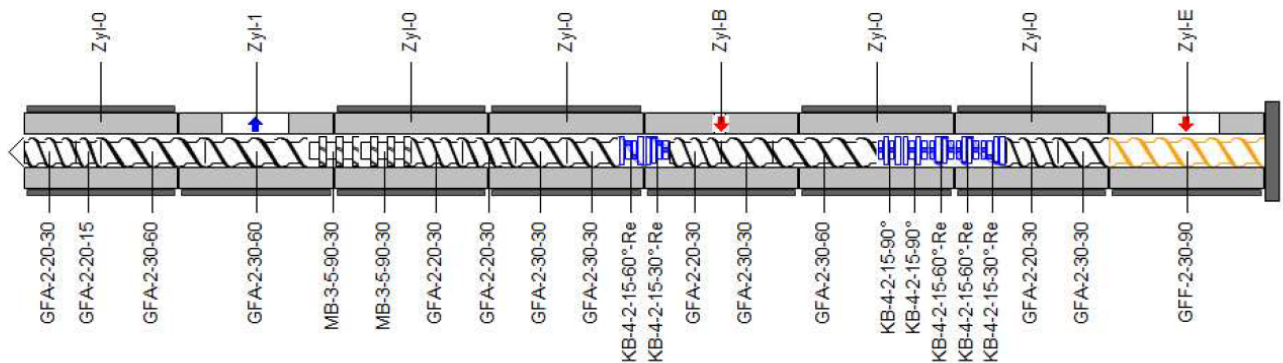


Figure 107. Leistritz screw profile

The codes represented in Figure 107 are those that allow the identification of each screw element necessary to build this specific screw profile. In particular, GFA and GFF acronyms

identify the conveying elements (also called screw elements by Ludovic) and the way to properly read these parameters is represented below (Figure 108).

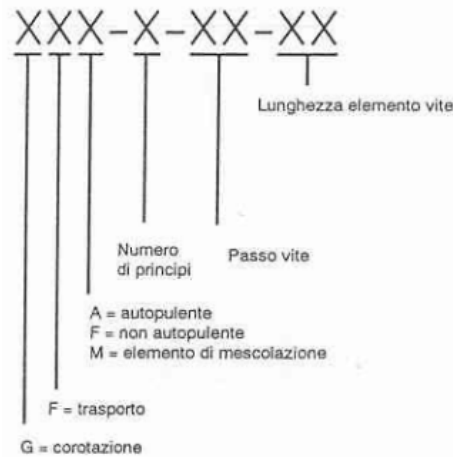


Figure 108. Conveying elements codes [TMP notes]

Similarly, KB indicates the kneading elements and the set of information contained in the code is again explained by Figure 109. The information about positive or negative transport is not needed if the staggering angle is 90°.

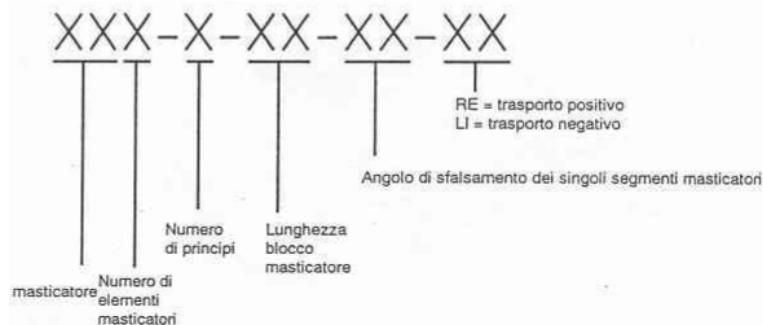


Figure 109. Kneading elements codes [TMP notes]

Concerning the MB codes, they correspond to the TMA elements in Ludovic, used in order to improve the mixing even more than with a simple mixing element.

### 3.2.1 “Extruder” section

#### Dimensions

As seen in Figure 100, to prepare a Ludovic simulation, the first thing to set are the extruder’s geometry parameters. In this case, the extruder has a barrel diameter of 18 mm, a centerline (distance between the screws) of 15 mm and the leakage between screw and barrel of 0,10 mm.

#### Zones & Barrels

In this case, the barrel is composed by 8 elements, each one with a 90 mm length. The feeding zone is approximated to be at the very beginning of the extruder. Two degassing (or extraction) elements are located in the fourth and in the seventh positions.

#### Screw elements

This tab is the one where the screw profile must be determined. Each chosen element that constitutes the screw must be characterized with its dimensions as mentioned before. The obtained extruder has the appearance represented in Figure 110.

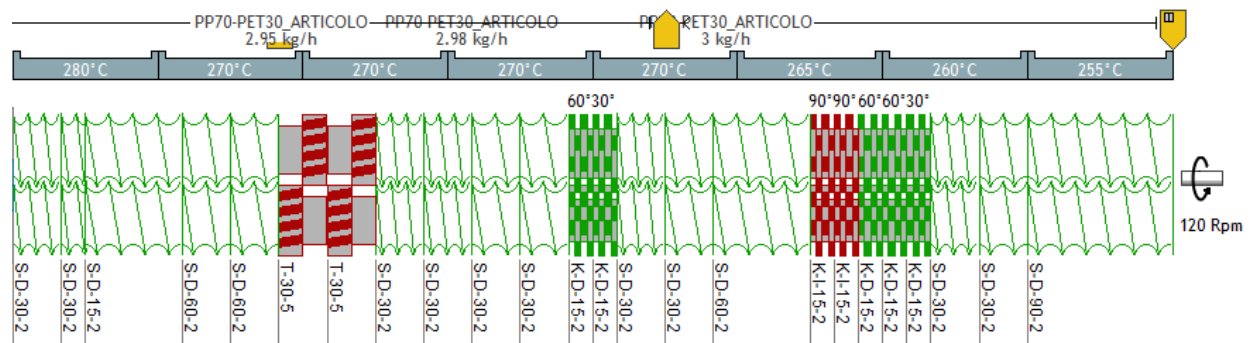


Figure 110. Leistritz screw profile in Ludovic.

### Die

To represent the die, the real one in Alessandria has been measured and has been built as a sequence of pipe elements. The result is the one represented in Figure 111. Analyzing the image from the right to the left, the first couple of pipes is composed by two intermeshing cylinders, while the last couple of pipes is made of two non-intermeshing elements. The table with each component's measures is reported below (Table 4.)

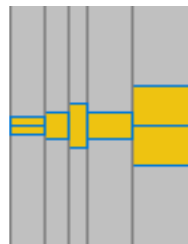


Figure 111. Die representation in Ludovic

| Length (mm) | Diameter (mm) | Number of Elements |
|-------------|---------------|--------------------|
| 20          | 18            | 2                  |
| 15          | 12            | 1                  |
| 6           | 20            | 1                  |
| 9           | 12            | 1                  |
| 11          | 4             | 2                  |

Table 4. Die dimensions

The “Set of elements” and “Extruder” tools have not been used.

### 3.2.2 “Products” section

The simulation was carried out using PP as a matrix in the amount of 70%wt and PET as the reinforcing phase in the quantity of 30%wt. In order to make a comparison, in one of the various simulations made with this system, the concentrations have been modified to have 90%wt of PP and 10%wt of PET. The parameters introduced in the software are those reported in Table 2 and Table 3.

### 3.2.3 “Process” section

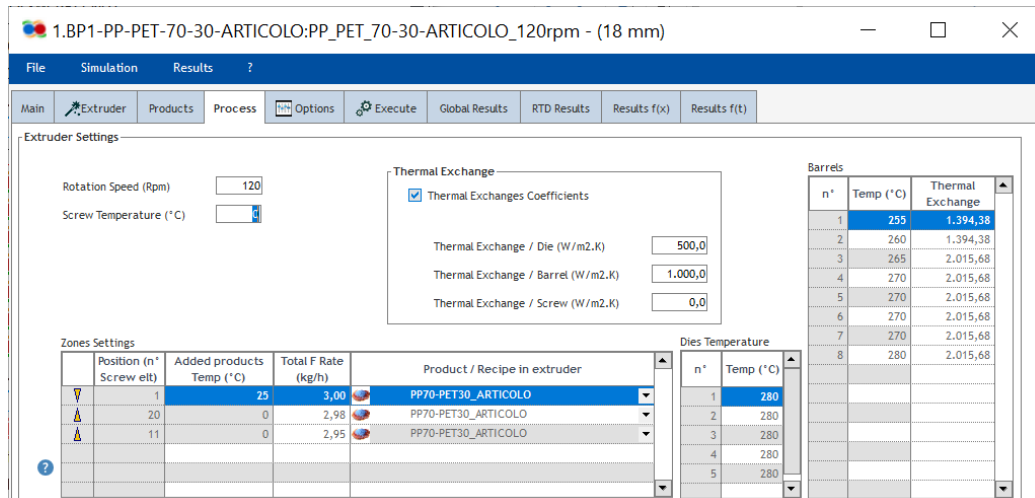


Figure 112. Process tab

Figure 112 displays all the information required to complete the simulation and launch it. The temperature profile (Table 5) and the rotation speed of 120 rpm have been defined according to the scientific paper that was taken as a model to analyze this system [5].

| Position         | 1   | 2   | 3   | 4   | 5   | 6   | 7   | 8   |
|------------------|-----|-----|-----|-----|-----|-----|-----|-----|
| Temperature [°C] | 255 | 260 | 265 | 270 | 270 | 270 | 270 | 280 |

Table 5. Temperature Profile

The thermal exchange coefficients, calculated by the thermal exchange coefficients  $h_{barrel}$ ,  $h_{die}$  and  $h_{screw}$  mentioned in chapter 2, have the typical values suggested by Ludovic software developers: 500 W/m<sup>2</sup>\*K and 1000 W/m<sup>2</sup>\*K. These values correspond to medium and good exchange, respectively. Due to the fact that the screw is not thermoregulated, the corresponding thermal exchange is kept at a 0 value. Thanks to the Advanced Control Interface (ACI) tool provided by Ludovic, the thermal coefficients can be automatically adjusted after a simulation has been run. It is done analyzing the difference between a computed temperature and a measured temperature. The measured temperature is typically the die temperature (280°C in the present case). In the “Barrels” table in Figure 112, column “Thermal Exchange”, the results obtained after the application of ACI tool are listed.

## 4. Results and discussion

### 4.1 Analysis of the obtained results

In the present work, one of the systems found in literature has been taken as reference to reproduce and evaluate the results obtained with Ludovic software. In particular, the first simulation was carried out filling in Ludovic's tabs with screw's speed (120 rpm) and materials' composition (PP 70%wt and PET 30%wt) reported in the selected scientific paper [5]. As far as screw's temperature profile is concerned, it has been defined on the basis of our PET's melting temperature, 246,5 °C. Due to the fact that the PET should melt as well inside the extruder, our temperature profile ranges from 255°C to 280°C.

After this first parameters' setting, five more simulations were carried out. The main aim of the execution of all these simulations is demonstrating how Ludovic software is reliable in the results that provides, and its efficiency must be taken into great account to find the best screw profile characteristics for the system of interest. Its use would permit an incredible saving of time and costs due to laboratory experiments, even if the software's accuracy as far as the morphology characteristic is not comparable to the one obtained in person.

With the exception of the residence time distribution (RTD), all the other properties are plotted as a function of the axial distance along the screw. The origin of the residence system corresponds to the point where the barrel ends and the die begins. The values on the x-axis are positive moving towards the hopper and negative in the opposite direction.

Concerning the RTD, instead, it corresponds to the plot of the amount (in percentage) of material that passes through the die as a function of time. In this case, all the obtained results will be analyzed together at the end of the paragraph to facilitate their comprehension, while results concerning temperature, shear rate and viscosity will be commented simulation by simulation.

#### 4.1.1 Simulation 1 – 120rpm - PP 70% + PET 30%

##### 4.1.1.1 Temperature

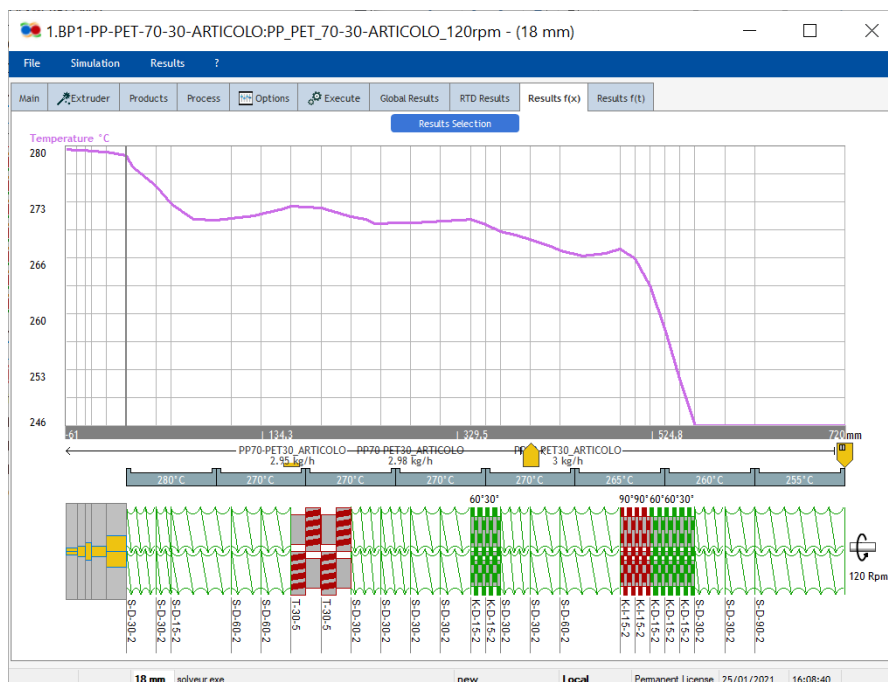


Figure 113. Temperature graph for 70%PP and 30%PET at 120rpm.



so, it only depends on the angular velocity  $\omega$  and on the extruder's geometry. It means that, once that the shape of the elements is fixed, the value of  $\dot{\gamma}$  is determined by the rotation speed. In fact, the shear rate plots are the same if the composition of the molten materials changes (see Figure 64 and Figure 80) because viscosity and material's composition do not influence  $\dot{\gamma}_0$ , while some differences can be seen when the rotation speed is modified.

As the plot in Figure 64 shows, the highest values of shear rate correspond to the restricting elements (namely,  $76,7 \text{ s}^{-1}$  in the kneading elements and  $75 \text{ s}^{-1}$  in the TME elements), while the conveying ones present a lower  $\dot{\gamma}$  value ( $40 \text{ s}^{-1}$ ). This is in line with what was expected, but what constitutes something unforeseen is the constant value of the shear rate along the kneading elements. In fact, due to the presence of different staggering angles, an increase in  $\dot{\gamma}$  in correspondence of higher angles was expected but do not seem to appear. This phenomenon can be explained considering that the kneading elements are composed by discs, each one with the same shape. Due to the fact that  $\dot{\gamma}$  is calculated on the tip area of each disc and all these areas are equivalent, it is correct to approximate a constant value of the shear rate on the whole kneading block.

The last peak encountered at  $x=5 \text{ mm}$  is probably due to the fact that the diameters of the die elements are smaller with respect to the screw elements' ones, so the melt in this region is subjected to higher shear stresses.

#### 4.1.1.3 Viscosity

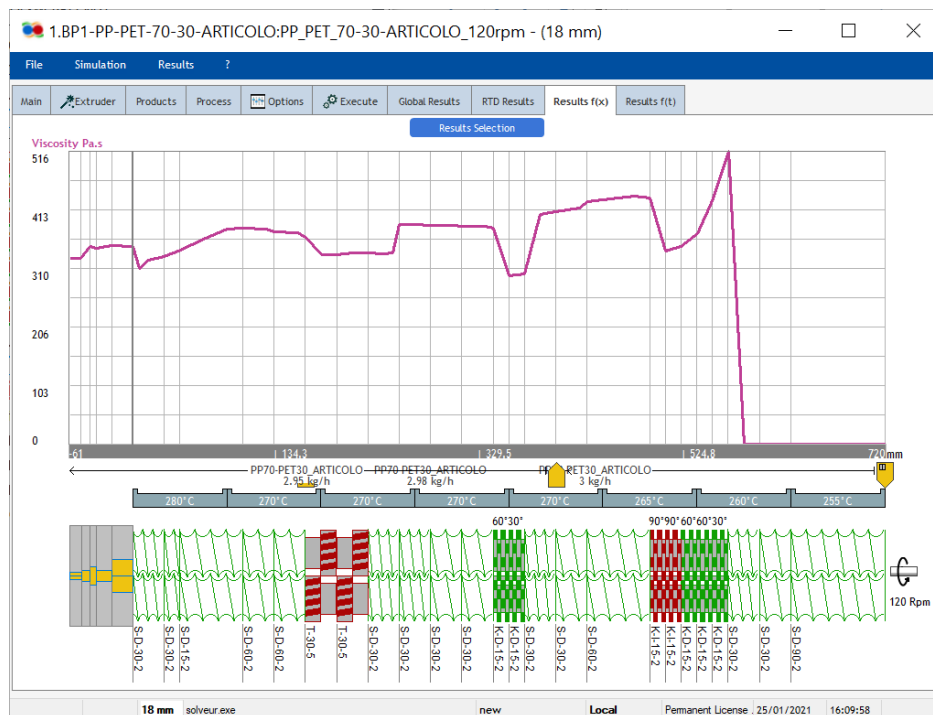


Figure 115. Viscosity graph for 70%PP and 30%PET at 120rpm.

Viscosity can be considered the most crucial parameter to be analyzed. In fact, the shape that the reinforcing phase assumes inside the matrix depends on it, as well as the overall value of the melt viscosity  $\eta_{melt}$ , (which is the parameter plotted in Figure 65). As mentioned by García-Masabet et al. [11], the configuration of the reinforcing material depends on the formula

$$p = \frac{\eta_{reinforce}}{\eta_{matrix}}$$

and so, it is undeniable the influence that the viscosity has on the final morphology of the material.

As can be seen in Figure 65, the viscosity maintains a value of 0 Pa\*s until the first kneading element is reached. At this point,  $x=585$  mm, there is a substantial raise in  $\eta_{melt}$ , that reaches the value of 516 Pa\*s at  $x=570$  mm. Here, the melt acquires a higher fluidity and  $\eta_{melt}$  decreases until the value of 345 Pa\*s. In correspondence of the following block of conveying elements, the temperature slightly decreases because of the lower shear rate, and this results in an increase in the melt viscosity, that reaches values up to 440 Pa\*s. Again, the viscosity decreases in correspondence of the kneading and TME elements and increases in the conveying one, for the same reasons mentioned above. The last decrease of  $\eta_{melt}$  occurs at the interface between the screw profile and the die and, as explained for the shear rate case, it is due to smaller radius of the die elements that provokes an increase in temperature and shear rate and a decrease in viscosity.

Another aspect that is noteworthy is that viscosity increases and decreases in a less remarkable way along the screw profile in the die direction. This is due to the fact that the thermoregulation system imposes a temperature that gradually increases while moving towards the die.

#### 4.1.2 Simulation 2 – 180rpm - PP 70% + PET 30%

The second simulation was carried out maintaining all the same parameters, except for the rotation speed, that was modified from 120 rpm to 180 rpm. In the following paragraph, the differences encountered with respect to the first simulation will be underlined and commented.

As long as the temperature profile is concerned (Figure 116), the shape of the curve is exactly the same as the one in Figure 113, the peaks are in the same positions along the screw profile and the isothermal plateaux as well. What changes is the value of the temperatures corresponding to each position on the x-axis. In fact, the whole curve appears at shifted values of temperature, about 2-3 °C higher with respect to the first simulation. For example, while in Figure 63 the first kneading elements cause an increase in temperature that reaches 267°C in  $x = 495$  mm, in this second case, in the same x-position, the reached temperature is 270°C, and so on. As known from the shear rate formula

$$\dot{\gamma}_0 = \omega \frac{R_2}{H}$$

an increase in the rotation speed provokes the increase in the shear rate value and, as mentioned before, the higher the shear rate the higher the energy dissipation, that causes an increase in temperature.

A similar analysis can be done describing the shear rate behavior in this second simulation. Again, the profile obtained is exactly the same as the one in the simulation 1 concerning the x-positions, but the shear rate values appear to be notably increased. This can be explained in the same way as in the previous paragraph: the increase in the rotation speed causes the increase in the shear rate. If, for example, the highest shear rate value in the current simulation, obtained in correspondence of the kneading elements, is  $115 \text{ s}^{-1}$ , in the first one it was  $76 \text{ s}^{-1}$ , and so on.

After all these considerations, it comes by itself the fact that an increase in the rotation speed provokes a decrease in the viscosity profile. In fact, if in simulation 1 the first peak corresponding to the first kneading element reaches a viscosity value of 516 Pa\*s, in this case the maximum is at 431 Pa\*s. Furthermore, the increase in rpm seems to render more marked

and sharper the viscosity profile, that increases notably in correspondence of the conveying elements and decreases in a steeper way where there are the restricting elements. Again, the presence of the thermoregulating system that smoothens the profile must be taken into account.

#### 4.1.2.1 Temperature

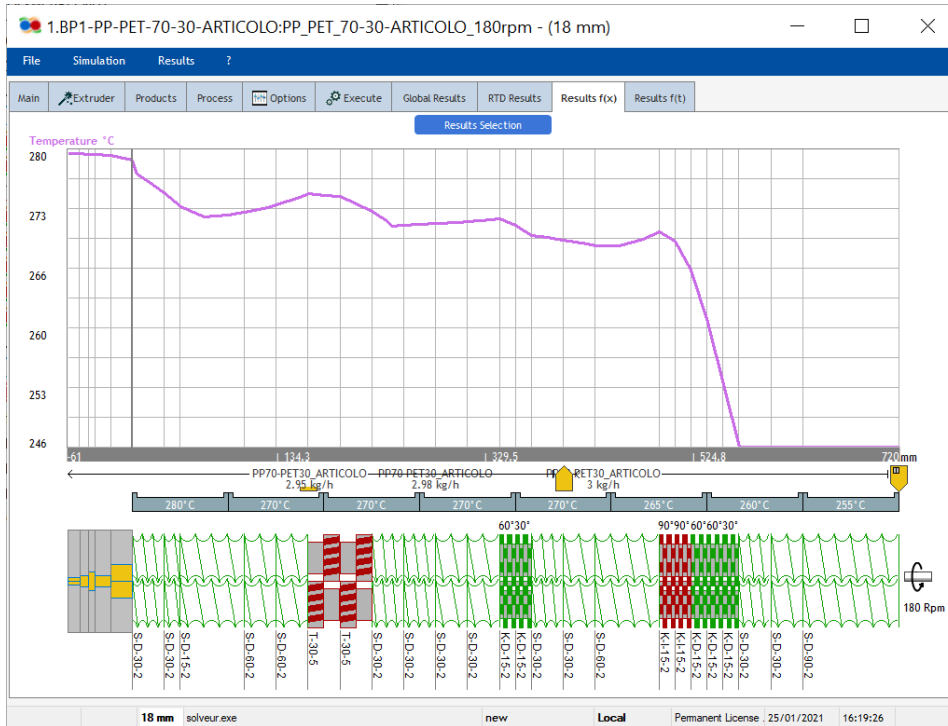


Figure 116. Temperature graph for 70%PP and 30%PET at 180rpm.

#### 4.1.2.2 Shear Rate

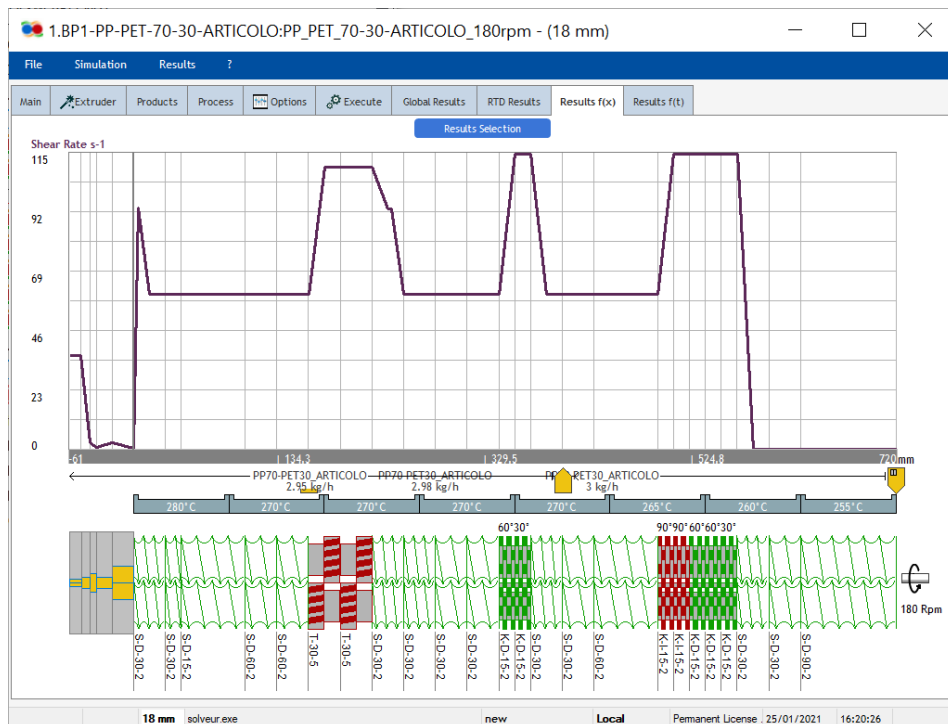


Figure 117. Shear rate graph for 70%PP and 30%PET at 180rpm.

### 4.1.2.3 Viscosity

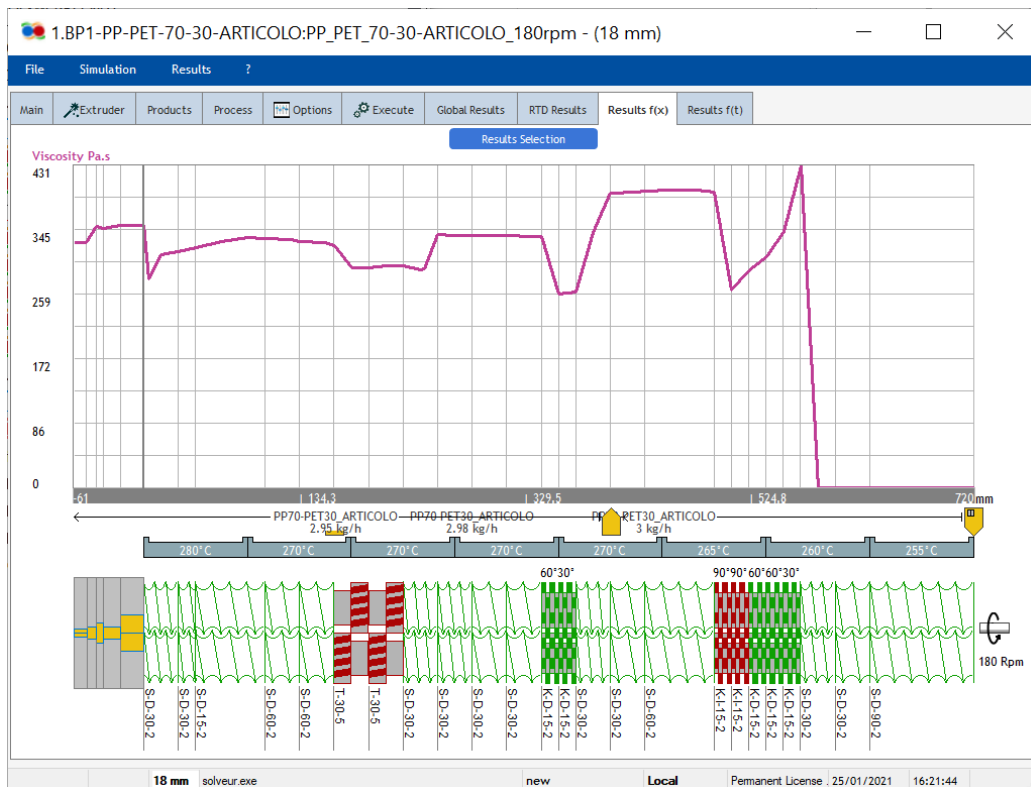


Figure 118. Viscosity graph for 70%PP and 30%PET at 180rpm.

### 4.1.3 Simulation 3 – 200rpm - PP 70% + PET 30%

Similarly to what was done in simulation 2, also in this case the only change occurred in the rotation speed, which was modified from 120 rpm to 200 rpm. The results expected are the same as in the previous simulation, but with even more marked values of the different parameters.

Concerning the temperature, a slight difference can be observed in the presence of an isothermal plateau in correspondence of the second block of conveying elements, while in the previous simulations this characteristic was much less marked. Also in this case, then, the curve is shifted to higher values of temperature: the T value corresponding to  $x = 495$  mm is  $271^{\circ}\text{C}$ , and this, again, is due to the fact that the increase in  $\omega$  provokes an increase in the shear rate that causes higher amounts of dissipated energy.

For the same reasons mentioned above, at higher rotation speeds correspond higher shear rates, and so, while the curve profile remains the same also in this graph, the maximum  $\dot{\gamma}$  value increases from  $76\text{ s}^{-1}$  in the first simulation and  $115\text{ s}^{-1}$  in the second, to  $128\text{ s}^{-1}$  in this one.

Viscosity decreases in a way which is even more marked with respect to the second simulation: its maximum value decreases to  $422\text{ Pa}\cdot\text{s}$  instead of  $516\text{ Pa}\cdot\text{s}$  in the first and  $431\text{ Pa}\cdot\text{s}$  in the second. The reasons are the same mentioned in the comment to the second simulation.

### 4.1.3.1 Temperature

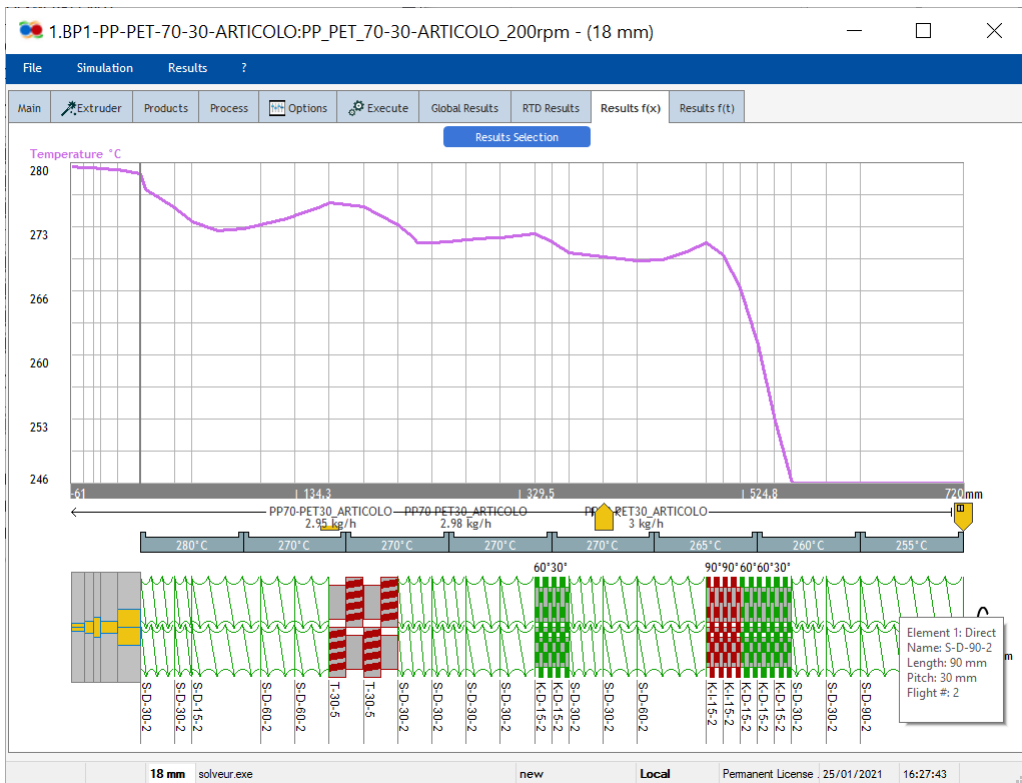


Figure 119. Temperature graph for 70%PP and 30%PET at 200rpm.

### 4.1.3.2 Shear Rate

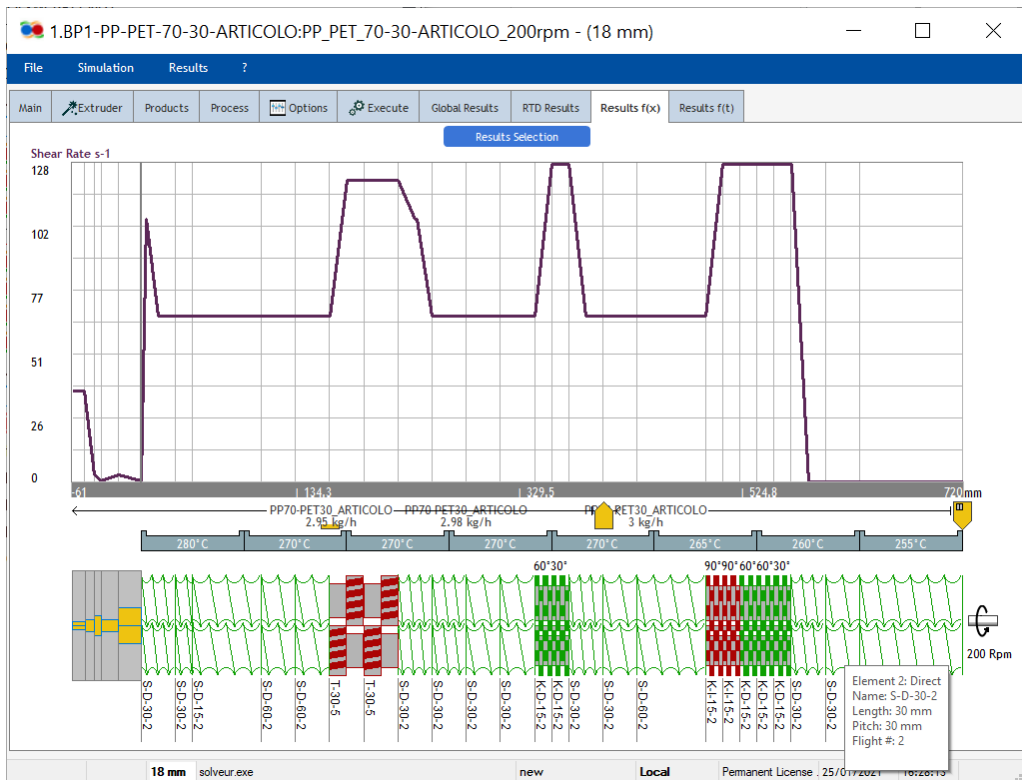


Figure 120. Shear rate graph for 70%PP and 30%PET at 200rpm.

### 4.1.3.3 Viscosity

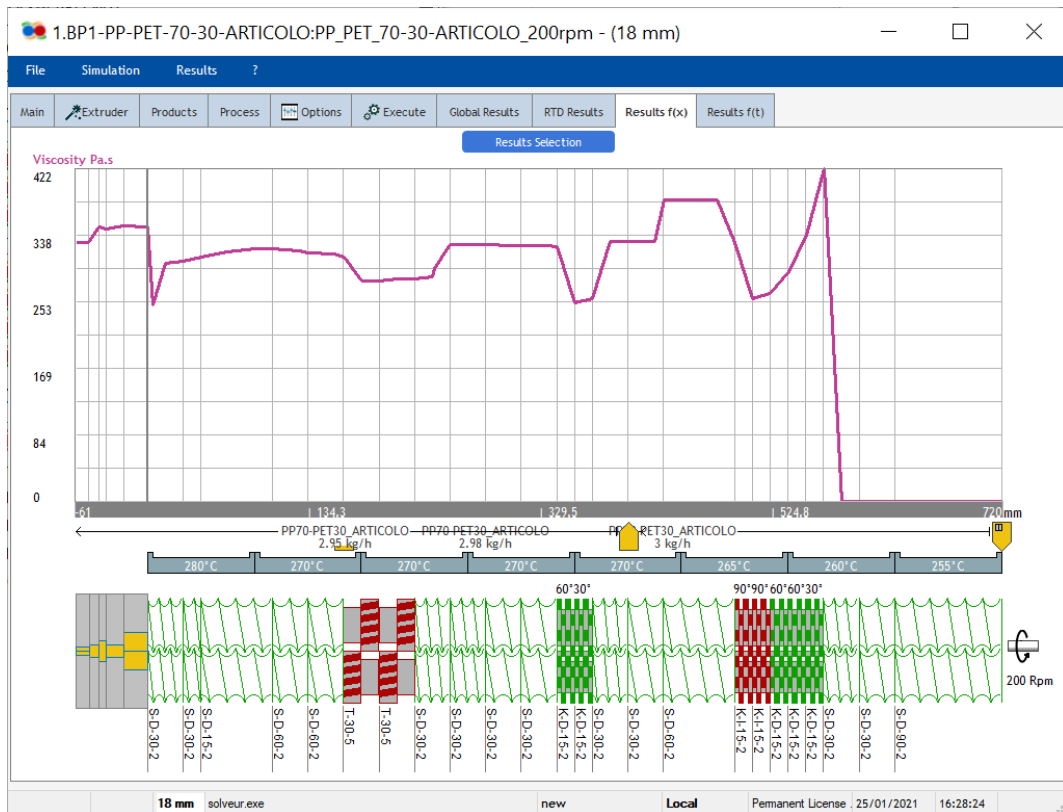


Figure 121. Viscosity graph for 70%PP and 30%PET at 200rpm.

### 4.1.4 Simulation 4 – 250rpm - PP 70% + PET 30%

One more change in the rotation speed has been applied, from 120 rpm to 250 rpm. The obtained results are very similar to those described above.

The temperature corresponding to  $x = 495$  mm, the value arbitrarily chosen as reference to compare the results, is  $274,8$  °C instead of  $267$ °C in the first simulation (Figure 122). The maximum shear rate value obtained in correspondence of the two series of kneading elements is  $159$   $s^{-1}$  instead of  $76$   $s^{-1}$  (Figure 123), while the viscosity has its major peak at  $372$  Pa\*s, a notably lower value if compared to the  $516$  Pa\*s obtained in the first case (Figure 124).

#### 4.1.4.1 Temperature

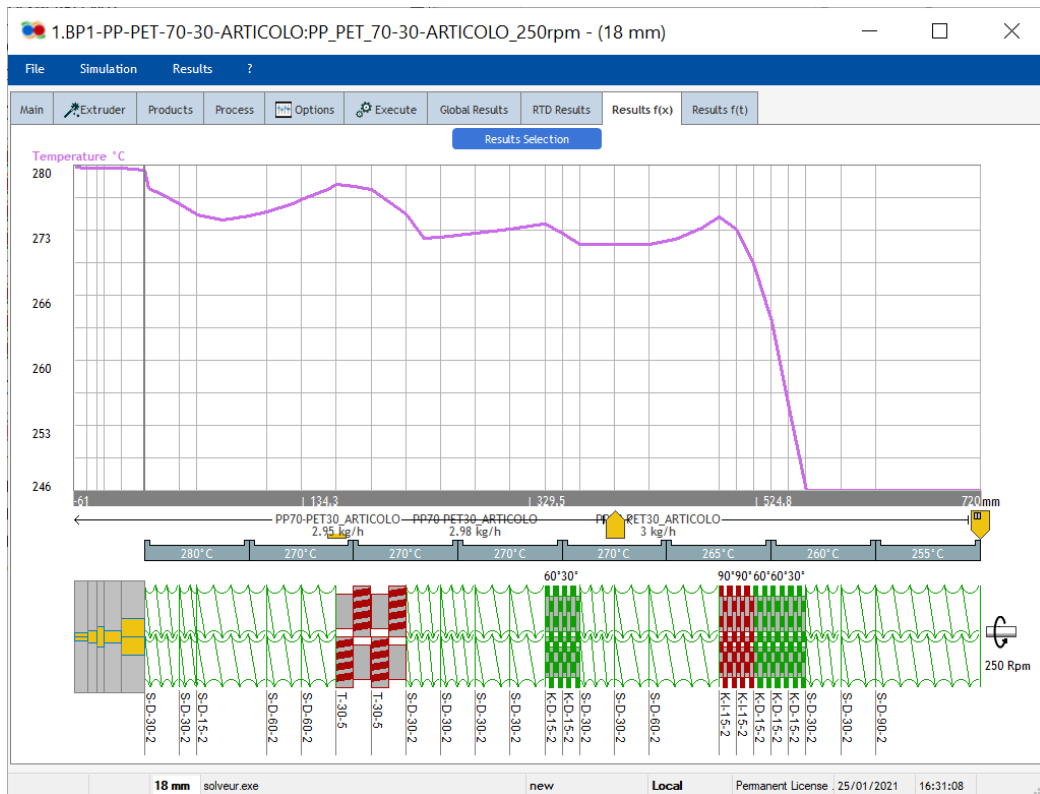


Figure 122. Temperature graph for 70% PP and 30% PET at 250rpm.

#### 4.1.4.2 Shear Rate

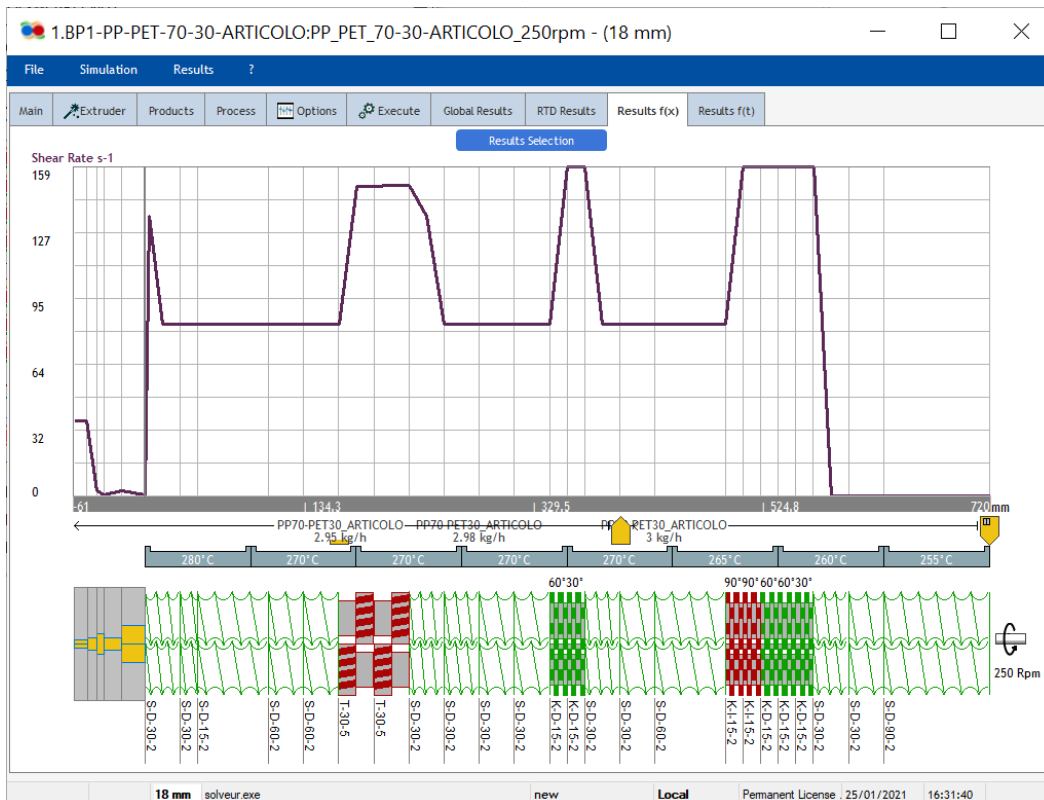


Figure 123. Shear rate graph for 70% PP and 30% PET at 250rpm.

#### 4.1.4.3 Viscosity

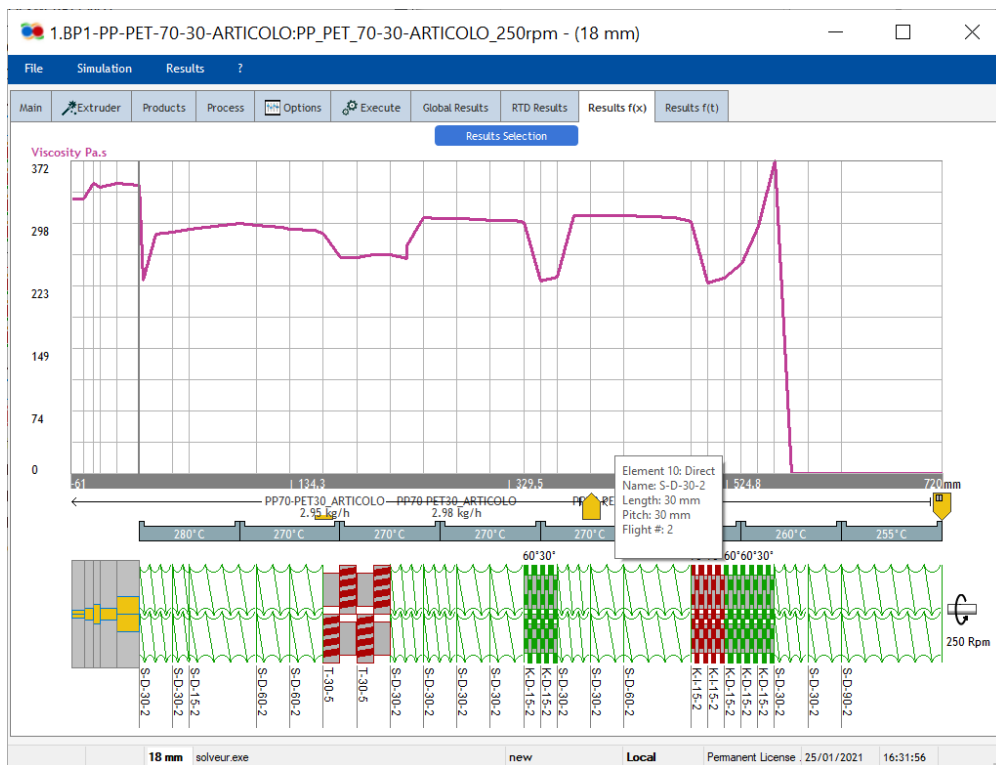


Figure 124. Viscosity graph for 70% PP and 30% PET at 250rpm.

The last two simulations have been carried out modifying the composition of the melt and the temperature profile, respectively. The rotation speed has been maintained at 120 rpm because it implies a higher residence time of the material inside the extruder, which should allow a more effective modification of the PET dispersed phase.

#### 4.1.5 Simulation 5 – 120rpm and PP 90% + PET 10%

The change in the composition do not seem to influence too much the temperature profile, but what can be noticed is the curve, in this case, is slightly shifted at lower temperatures. To the position along the screw  $x = 495$  mm correspond  $265^{\circ}\text{C}$  while in the first case the temperature in this point was  $267^{\circ}\text{C}$ . this can be due to the fact that the 90% of the molten material is constituted by PP, whose viscosity is lower than that of PET. A bigger amount of PP could require the production of a bit less dissipation energy.

As already mentioned before, the shear rate does not depend on the material's composition and therefore there are no differences in the two plots (Figure 114 and Figure 126).

The viscosity, instead, as a remarkably lower value in the present simulation with respect to the first one. While the profile shape is quite similar, the highest peak reached in this case only reaches  $262 \text{ Pa}\cdot\text{s}$ , versus the  $516 \text{ Pa}\cdot\text{s}$  obtained in Simulation 1 (Figure 115 vs Figure 127). The only possible explanation is the fact that, here, the 90% of the material in the extruder is PP, which has a notably lower viscosity with respect to the PET.

### 4.1.5.1 Temperature

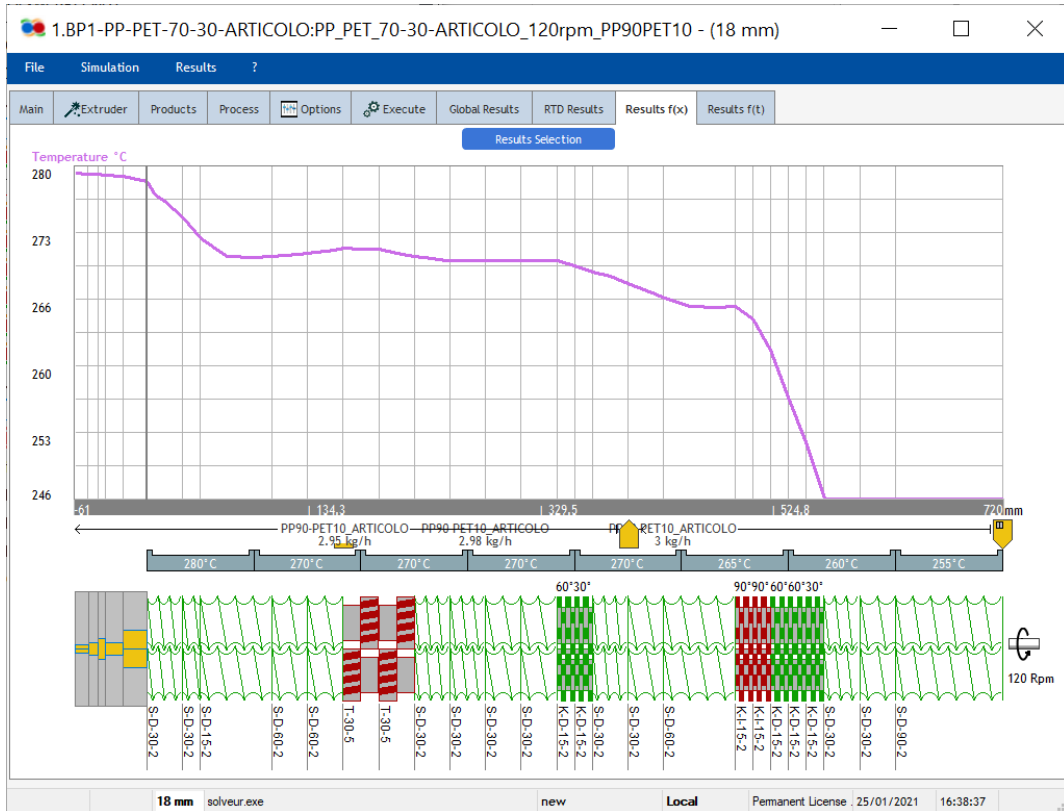


Figure 125. Temperature graph for 90% PP and 10% PET at 120rpm.

### 4.1.5.2 Shear Rate

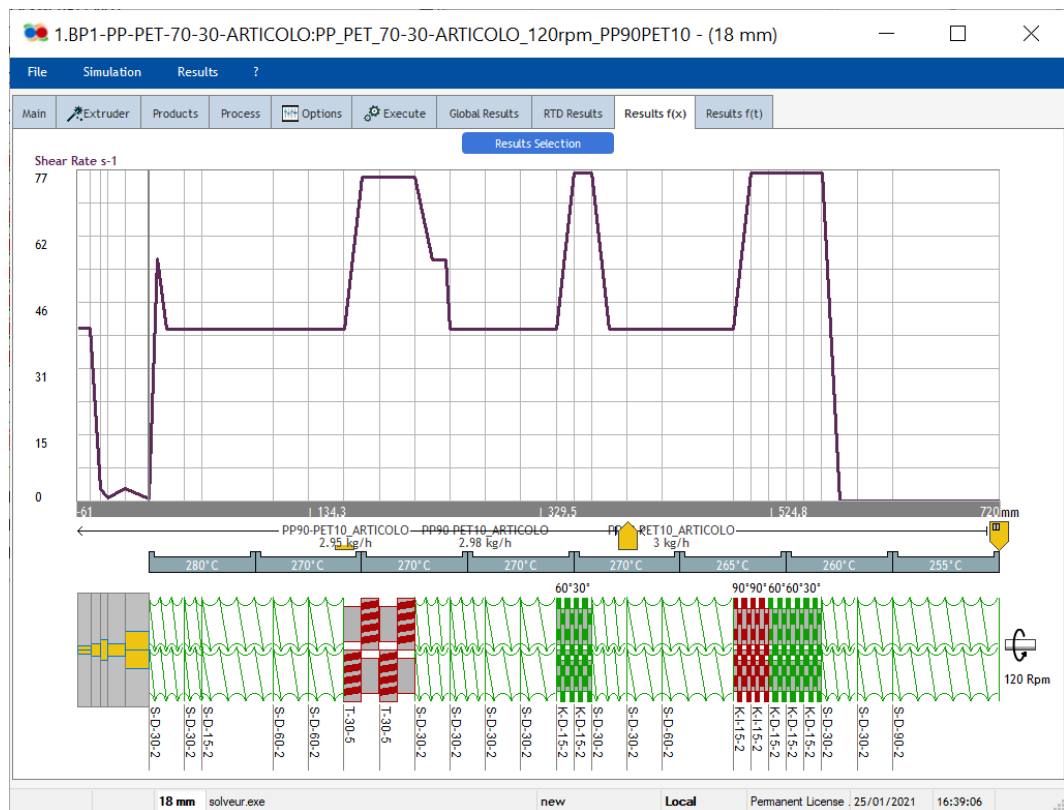


Figure 126. Shear rate graph for 90% PP and 10% PET at 120rpm.

### 4.1.5.3 Viscosity

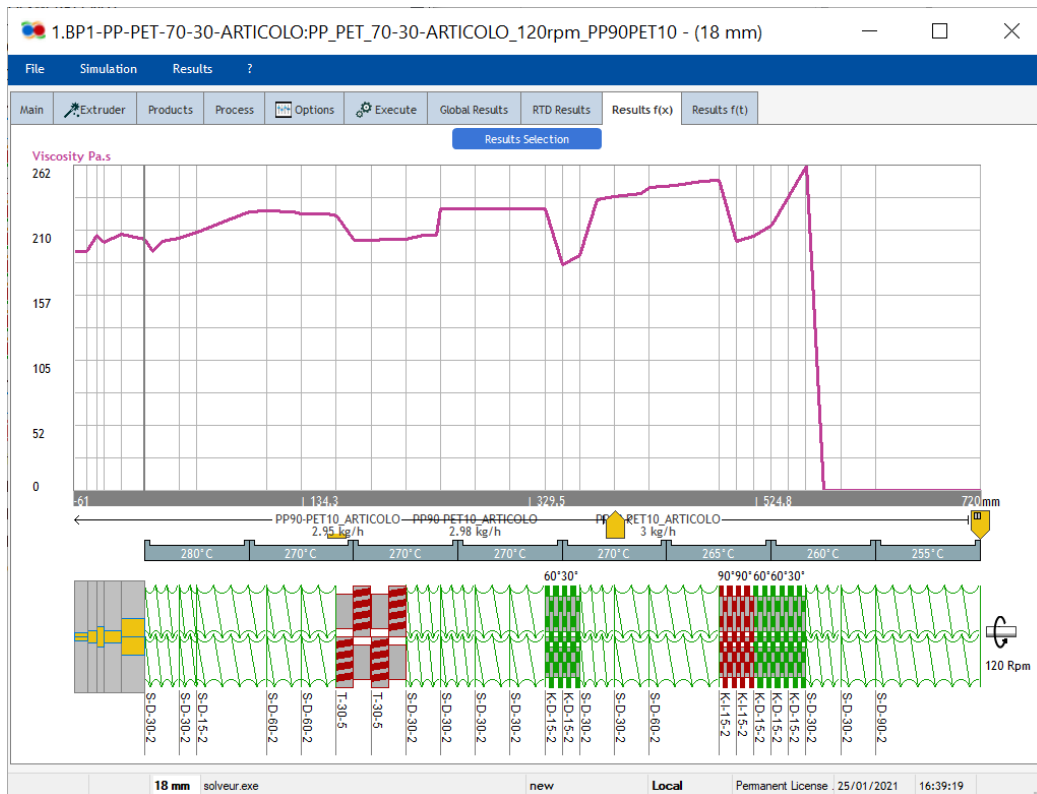


Figure 127. Viscosity graph for 90% PP and 10% PET at 120rpm.

### 4.1.6 Simulation 6 – 120 rpm and change in the temperature profile

| Screw element             | 1     | 2     | 3     | 4     | 5     | 6     | 7     | 8     |
|---------------------------|-------|-------|-------|-------|-------|-------|-------|-------|
| 1 <sup>st</sup> T profile | 255°C | 260°C | 265°C | 270°C | 270°C | 270°C | 270°C | 280°C |
| New T profile             | 260°C | 265°C | 270°C | 275°C | 280°C | 285°C | 290°C | 285°C |

This last modification has been applied maintaining the temperature slightly higher with respect to the first profile, always remaining in the range where the PET is molten.

As it happened in all the previous simulations as well, the temperature starts raising in correspondence of the first kneading element and, in this case, it continues to increase in a quite gradual way: the peaks and the plateau are nearly indistinguishable here, the temperature profile follows accurately the input parameters.

Due to the fact that the temperature has no influence in the shear rate computation in Ludovic software, no differences are expected in this graph. In fact, the shear rate profile in Figure 129 is exactly the same as in Figure 114.

Instead, a great change is expected as far as the viscosity profile is concerned. Temperature increases, in fact, always produce a decrease in viscosity, and that is what happens in this case as well (Figure 130). After a similar trend until  $x = 345$  mm, in the present case the viscosity starts to decrease quite regularly until the die, while Simulation 1 has a behavior that remarks

more notably the screw profile. In this last simulation, instead, a sort of Newtonian plateau is obtained in correspondence of the viscosity value of 243 Pa\*s and it goes from about  $x = 235$  mm to 7 mm.

#### 4.1.6.1 Temperature



Figure 128. Temperature graph for 70% PP and 30% PET, at 120rpm and with the modified profile temperature.

#### 4.1.6.2 Shear Rate

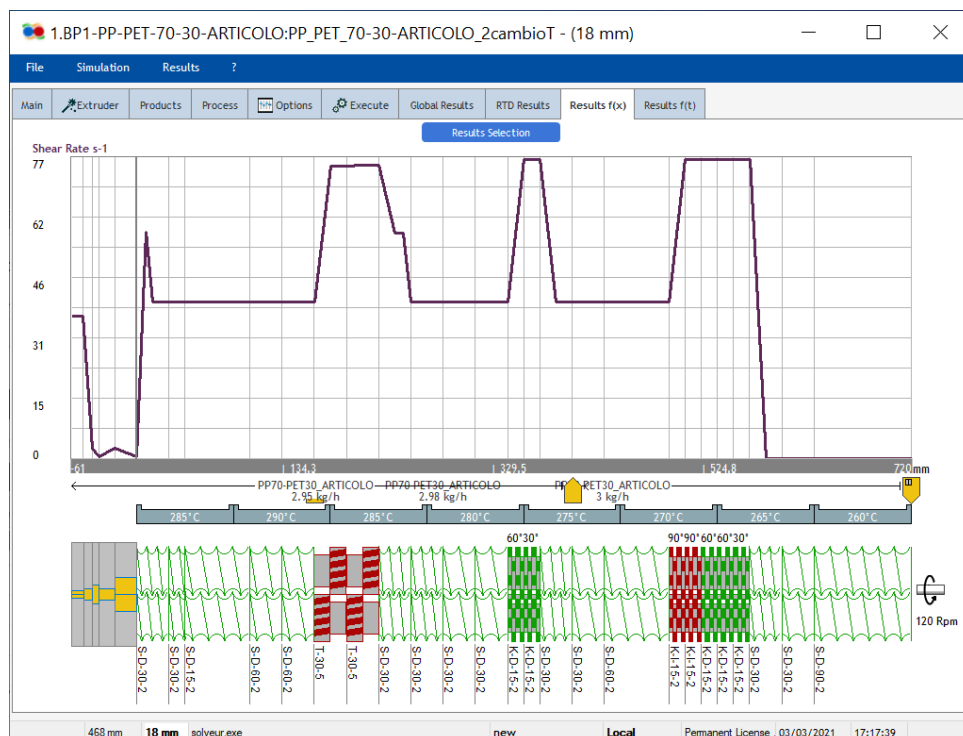


Figure 129. Shear rate graph for 70% PP and 30% PET, at 120rpm and with the modified profile temperature.

### 4.1.6.3 Viscosity

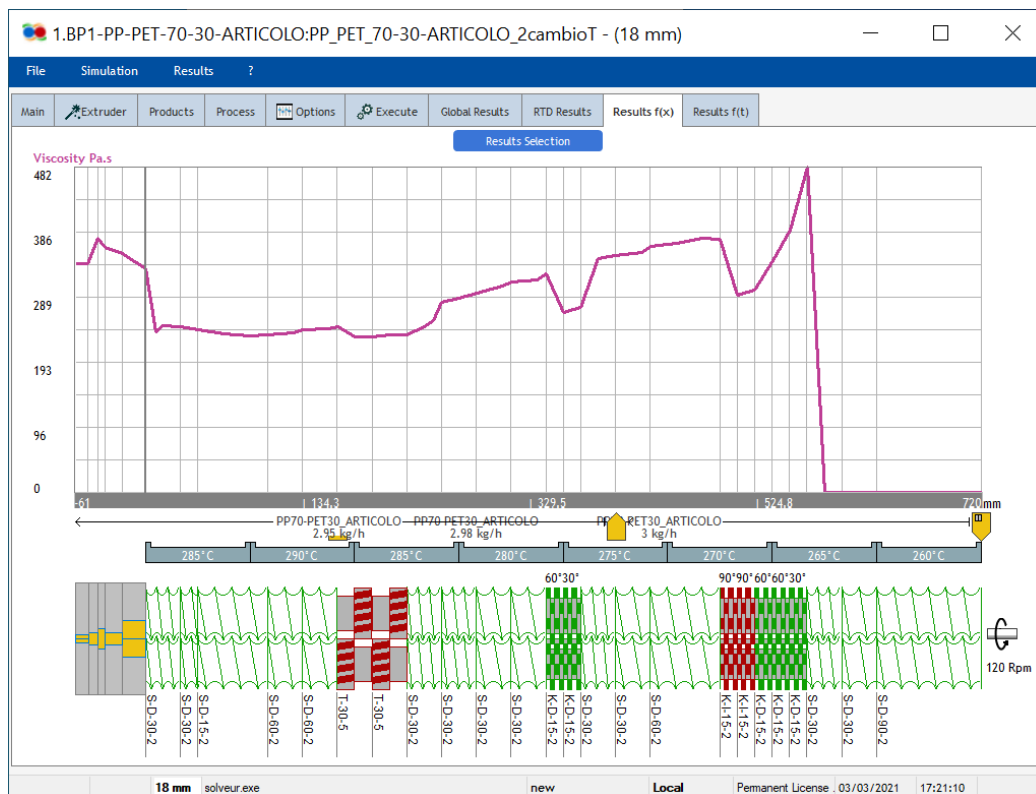


Figure 130. Viscosity graph for 70% PP and 30% PET, at 120rpm and with the modified profile temperature.

### 4.1.7 Residence Time

The results obtained in the Residence Time Distribution tab are the only ones that are not reported with respect to the x-axis but as the amount (in percentage) of material that passes through the die with respect to the time (resident time). The given results are the minimum resident time, the mean one and the value of the peak. The shape of the distribution curve, evaluated at its mid-height, provides information about the time needed by the material to pass through the die: a more restricted distribution means that a major part of the molten material crosses the die section in a similar (or equal) time, while a wider distribution indicates the presence of some delay. The first case is the preferred one because it renders the process easier to be controlled. What must be underlined is the fact that the residence time distribution does not provide results for each screw element but is a general parameter.

In the RTD case, in contrast to the other results, all the obtained data are compared in Table 6 in order to better understand the information given. What can generally be said, is the fact the Residence Time Distribution values decrease with the increase of the rotation speed. The change in the composition slightly decreases the RTD values, probably because the modification of the melt viscosity. The modifications in the temperature profile do not affect the residence time, notwithstanding the variation of the material viscosity resulting from the different temperature established within the extruder should induce some differences in the measured RTD.

| Simulation number | Modified parameter              | Minimum RTD | Mean RTD | Peak Value |
|-------------------|---------------------------------|-------------|----------|------------|
| 1                 | -                               | 44,67 s     | 80,2 s   | 62,26 s    |
| 2                 | Rotation Speed<br>180 rpm       | 37,04 s     | 71,8 s   | 54,47 s    |
| 3                 | Rotation Speed<br>200 rpm       | 35,46 s     | 70,15 s  | 52,66 s    |
| 4                 | Rotation Speed<br>250 rpm       | 32,62 s     | 67,19 s  | 49,94 s    |
| 5                 | Composition –<br>90% PP-10% PET | 42,4 s      | 74,55 s  | 58,26 s    |
| 6                 | Temperature<br>Profile          | 44,63 s     | 80,2 s   | 62,27 s    |

Table 6. RTD values obtained for all the carried-out simulations.

In the following pages, all the obtained graphs related to the RTD are presented.

### Simulation 1

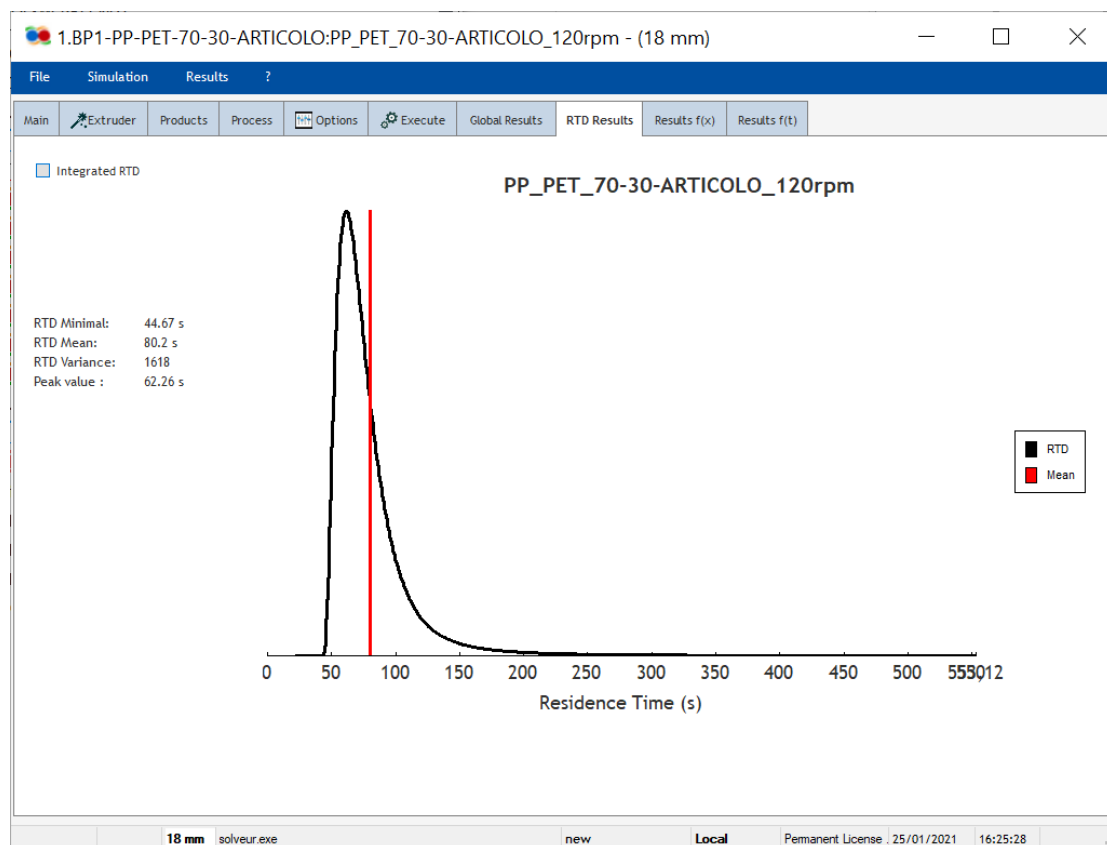


Figure 131. Residence time graph for 70%PP and 30%PET at 120rpm

## Simulation 2

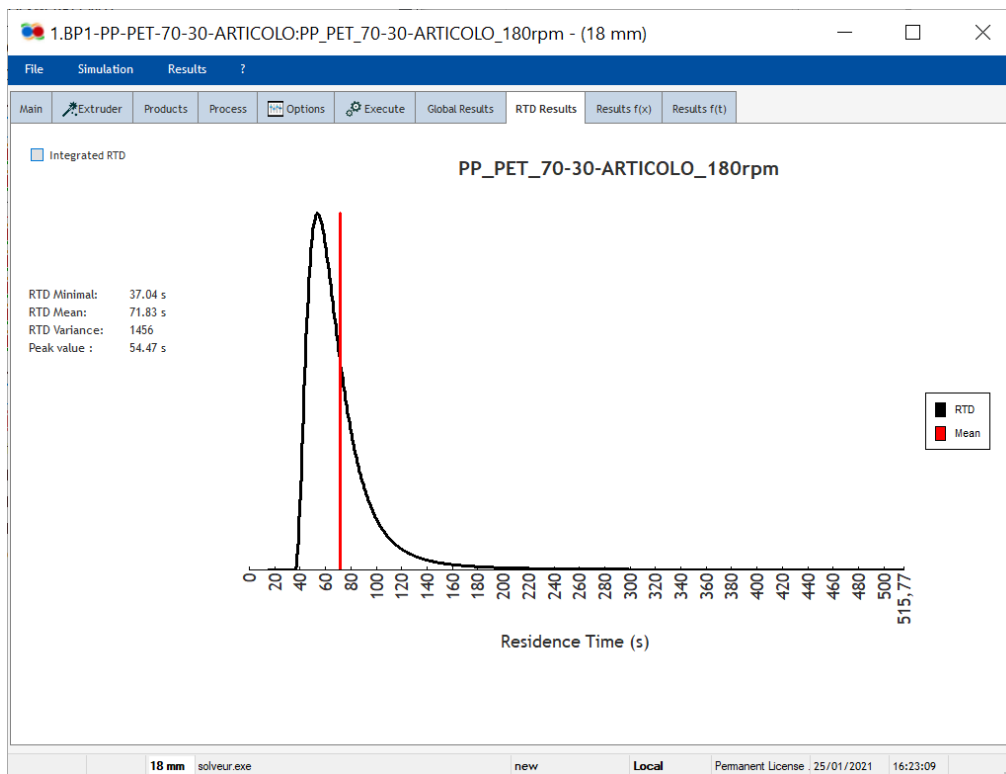


Figure 132. Residence time graph for 70%PP and 30%PET at 180rpm

## Simulation 3

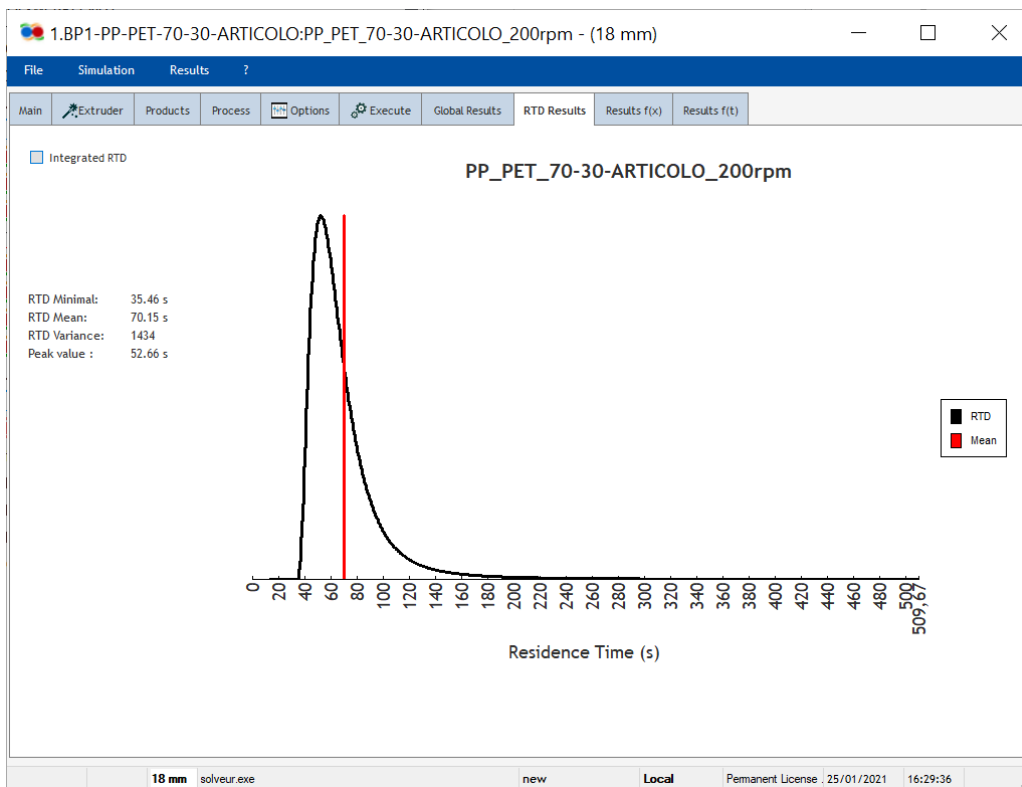


Figure 133. Residence time graph for 70%PP and 30%PET at 200rpm

## Simulation 4

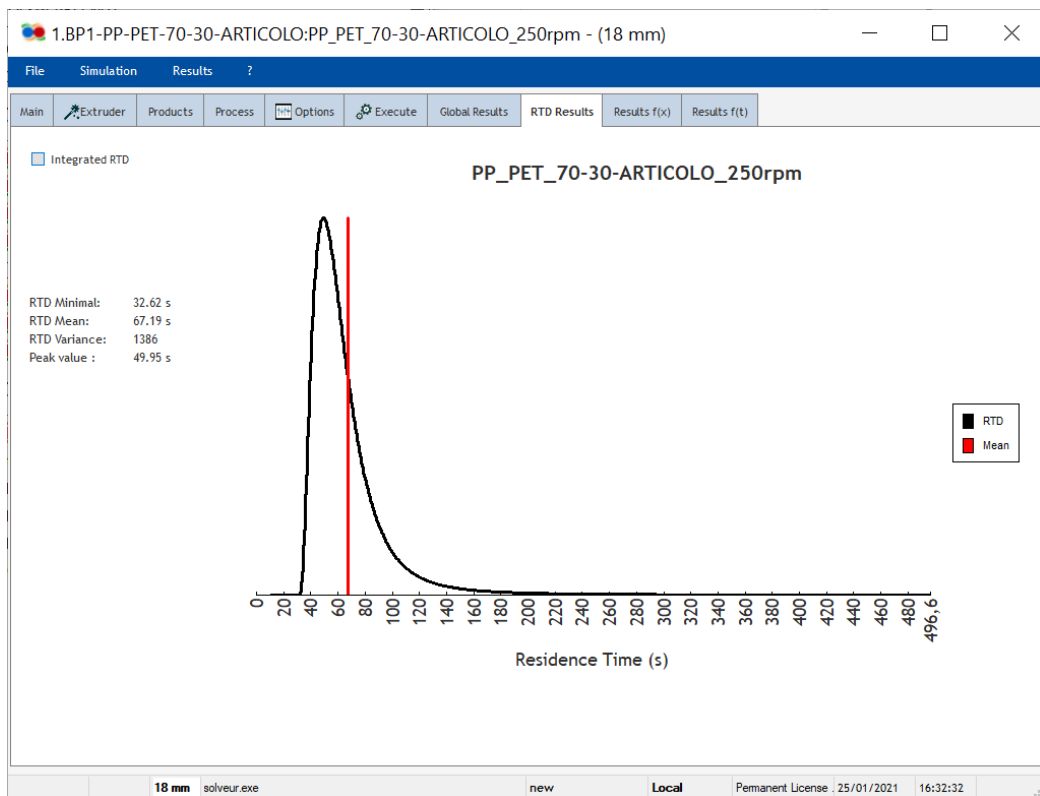


Figure 134. Residence time graph for 70%PP and 30%PET at 250rpm

## Simulation 5

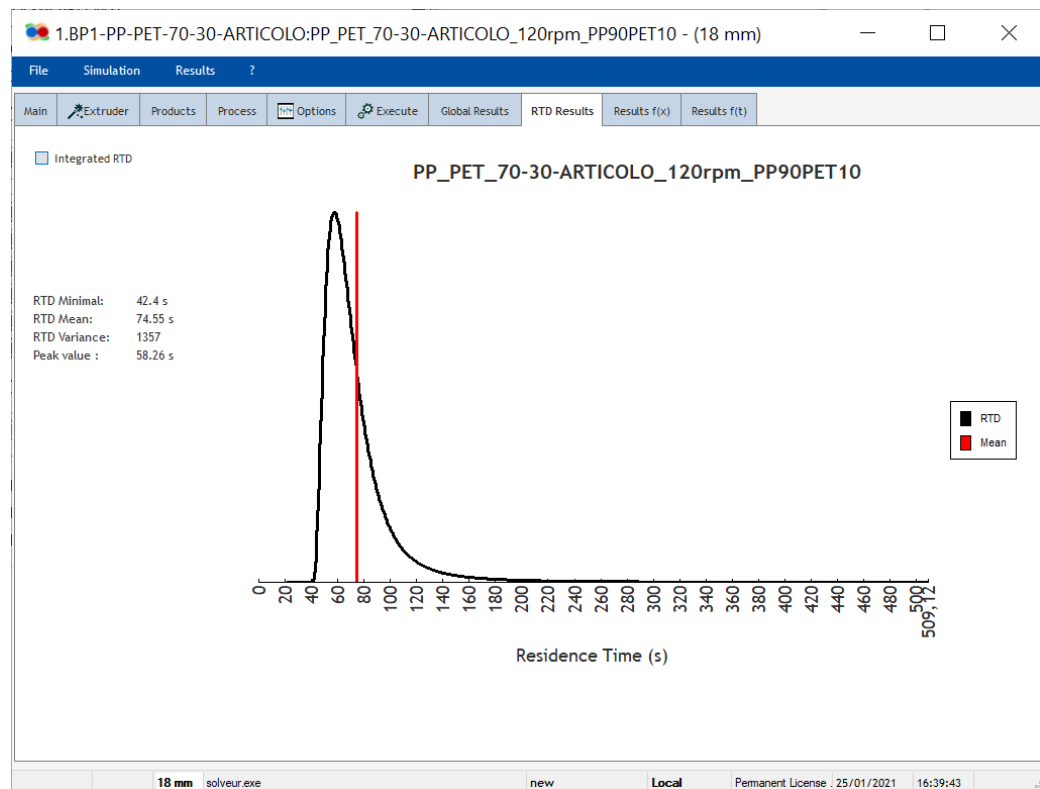


Figure 135. Residence time graph for 90%PP and 10%PET at 120rpm

## Simulation 6

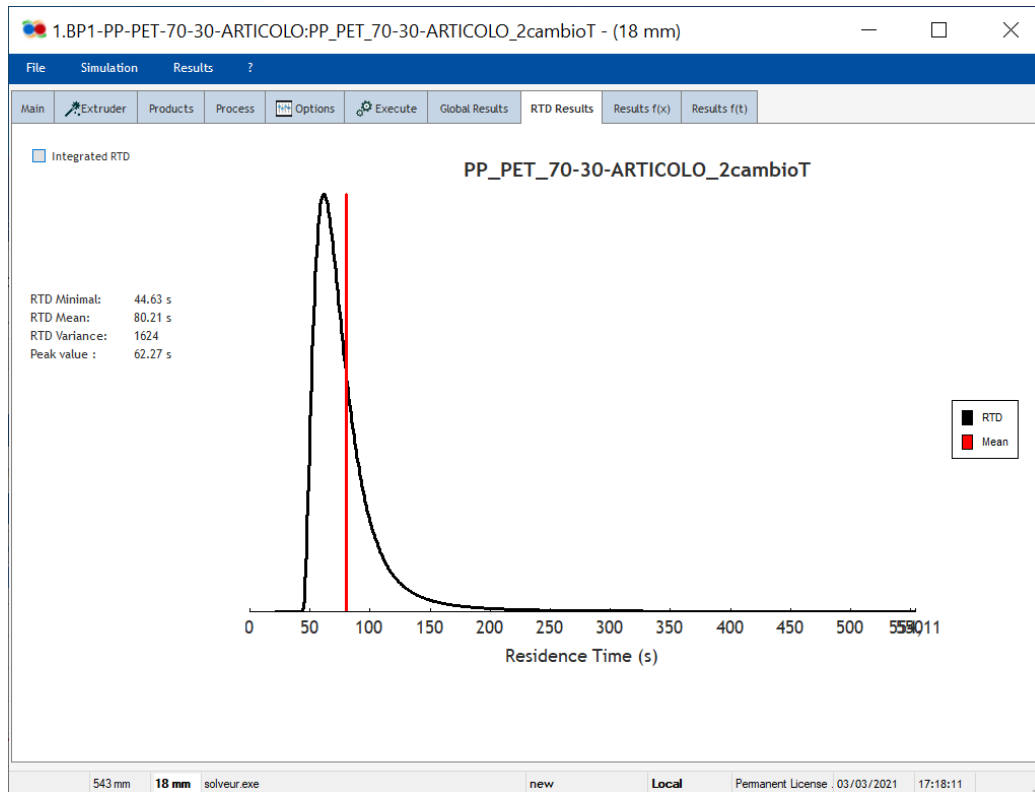


Figure 136. Residence time graph for 70% PP and 30% PET, at 120rpm and with the modified profile temperature.

### 4.2 Conditions to obtain fibrillation

As mentioned by Garcia-Masabet [11], a rheological analysis of the parameters that characterize the behavior of neat polymers is a key method to predict the morphology of the microfibrillar composites that will be obtained. This knowledge can consequently lead to an enormous increase in the mechanical properties of the obtained material. These parameters are, in particular:

- the viscosity ratio  $p$
- the capillary number  $Ca$

To properly understand the importance of these parameters, it is fundamental to comprehend the physical process taking place during the mixing conditions experienced by the melt. During the melt flow, the dispersed phase is subjected to an important change in geometry, and this is governed by the capillary number  $Ca$ , that is defined as the ratio between the hydrodynamic forces (in which the viscosity of the phase that acts as the matrix has a leading role) and the interfacial tensions between the two phases, that tends to bring the dispersed phase back to a spherical shape. In a shear flow field, the capillary ratio is described by the following formula

$$Ca = \frac{\eta_m \dot{\gamma} R}{\Gamma_{d,m}}$$

where  $\eta_m$  is the matrix's shear viscosity,  $\dot{\gamma}$  is the shear rate,  $R$  the radius of the droplet and  $\Gamma_{d,m}$  is the interfacial tension between the phases. Grace et al. [13] investigated the deformation and

breakup of the dispersed phase assuming a correlation between the capillary number  $Ca$  and the shear viscosity ratio  $p$ . In particular, the shear viscosity ratio  $p$  is defined as

$$p = \frac{\eta_d}{\eta_m}$$

where  $\eta_d$  is the viscosity of the dispersed phase and  $\eta_m$  is the one of the matrix phase. According to their study, the breakup of the as-inserted particles occurs when the system reaches a critical value of the capillary number ( $Ca_{crit}$ ). This value depends on the viscosity ratio  $p$  and on the flow field applied. The trend of the critical capillary number as a function of the viscosity ratio is presented in Figure 137.

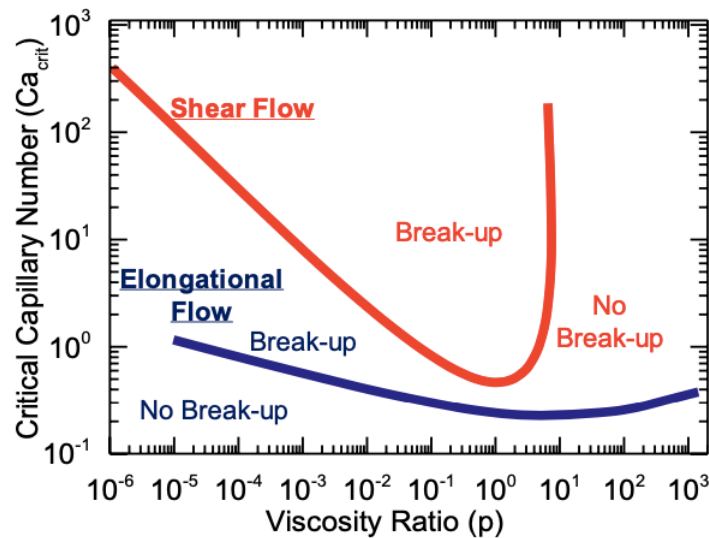


Figure 137. Critical capillary number as a function of the viscosity ratio.

Furthermore, it has been found that, knowing the viscosity ratio  $p$  and having reached the critical capillary number, it is possible to predict the different deformation and breakup mechanisms, as shown in Figure 138.

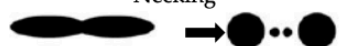
| Viscosity Ratio ( $p$ ) | Break-up Mechanism   | Description  |
|-------------------------|--|--|
| Much lower 0.1          | Tip streaming<br>     | The break-up occurs at the tip of the deformed droplet and generally produce very fine droplets                    |
| 0.1 < $p$ < 1           | Necking<br>           | The deformed droplet breaks up into two daughter droplets.   |
|                         | End pinching<br>      | The deformation produces a dumbbell shape, after which the break-up occurs in the two droplets formed at the ends. |
| 1 < $p$ < 3.8           | Rayleigh break-up<br> | Interfacial instabilities produce disturbances that will break up the fibril into a line of droplets.              |
| $p > 3.8$               | No break-up<br>       | The break-up of the droplet under shear is not possible.   |

Figure 138. Deformation and breakup mechanisms related to viscosity ratio  $p$ .

This same argument has been applied to the system analyzed in this work, in order to predict if the chosen operating conditions promote the formation of a fibrillated composite material.

It is important to underline that, after the extrusion, the production process of these materials always involves a stretching step carried out by a take-up machine. This step is fundamental to impart further elongational flow to the composite that, after the extrusion, tends to relax and lose the elongated shape acquired by the initial particles. Thanks to the take-up step, the fibrils created inside the extruder are permanently maintained even during cooling (Figure 139).

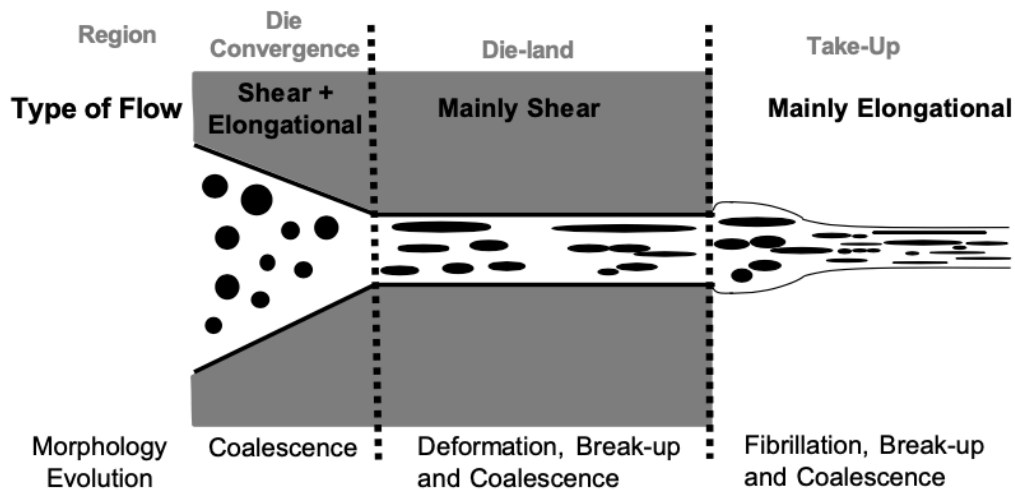


Figure 139. Relationship between the kind of flow and induced morphology in the different die zones.

To verify if the parameters inserted in Ludovic software could effectively bring to the formation of the fibrils, even if the take-up process is not part of our investigation, all the simulations executed on the blend materials were carried out again on our pure PET and PP.

Subsequently, the data concerning the obtained viscosities in every case were exported as excel files and the viscosity ratio  $p$  has been calculated for all the screw speed rotations applied and for the modified temperature profile. The case concerning the change in the composition has not been taken into consideration because there were no changes in the viscosities with respect to the other simulations.

The viscosity ratio  $p$  between the  $\eta_{PET}$  and  $\eta_{PP}$  has been calculated for 120, 180, 200 and 250rpm, as well as for the different temperature profile. The obtained values have been plotted as a function of the screw configuration, as Figure 140 and Figure 141 show.

As explained in Figure 138, the objective was to verify for which conditions the viscosity ratio had a value greater than 3,8, because those are the situations that can lead to the formation of the fibrils.

The results obtained confirm that the optimal screw rotation speed is 120 rpm, the minimum value among those that have been tested. This can be explained with the fact that the longer compounding times that result from lower rotation speeds promote the formation of thinner and stronger fibrils [1]. Even though 120 rpm appears as the speed that assures the formation of the better-shaped fibrils, also 180 and 200 rpm seem to be good enough to reach the objective. Only at 250 rpm the viscosity ratio presents some points in which its value is minor than 3,8, reason for which this is not a recommendable value to use during the processing of our PP/PET system.

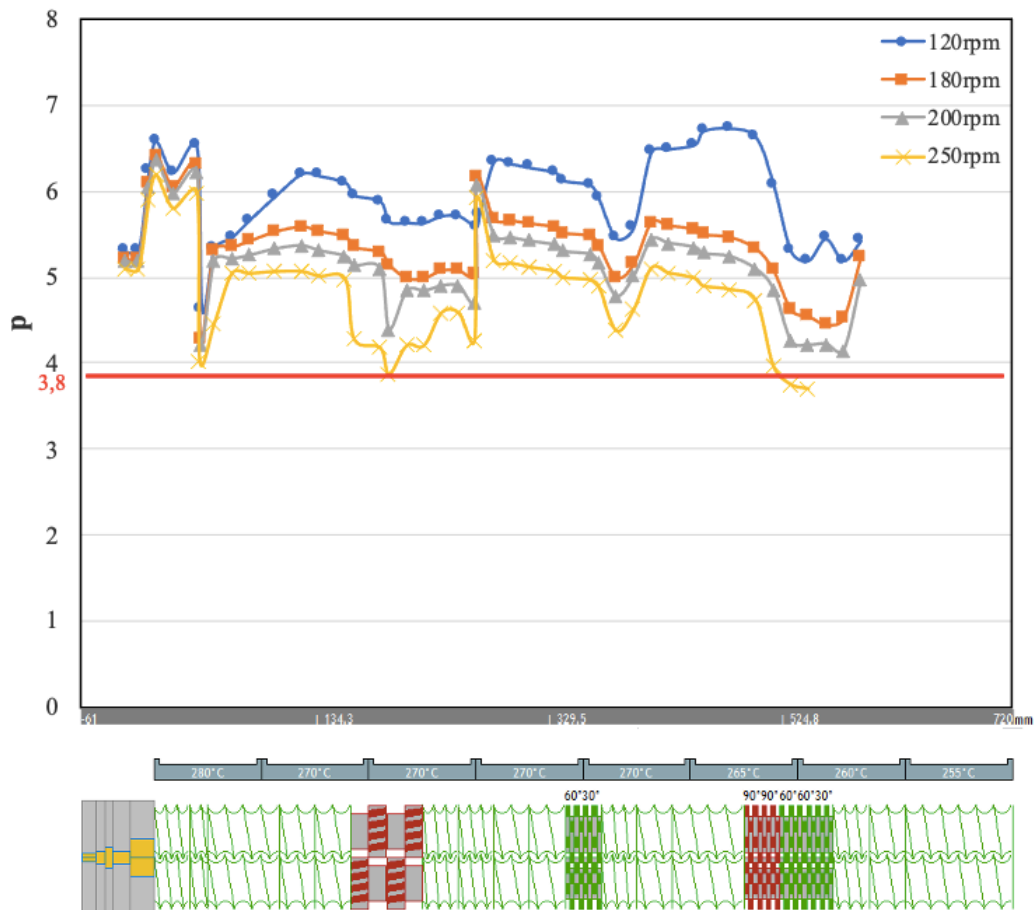


Figure 140. Viscosity ratio  $p$  as a function of the screw profile when the screw speed rotations change.

Concerning the comparison between the two temperature profiles, instead, it can be said that the best performance is obtained with the first one used, which corresponds to the blue line in Figure 140. When it is modified at slightly higher values of temperature, light-blue line in Figure 140, the viscosity ratio is shifted to values closer to 3,8 and, in some cases, even lower. At higher temperatures, in fact, it is widely known that the viscosity decreases, and, in the analyzed system, this behavior is much more marked for the PET, where the viscosity curve after the temperature change is significantly shifted at lower values (Figure 142). This means that the best choice to process the fibrillar composite of interest is using the first temperature profile, that is 255, 260, 265, 270, 270, 270, 270, 280°C.

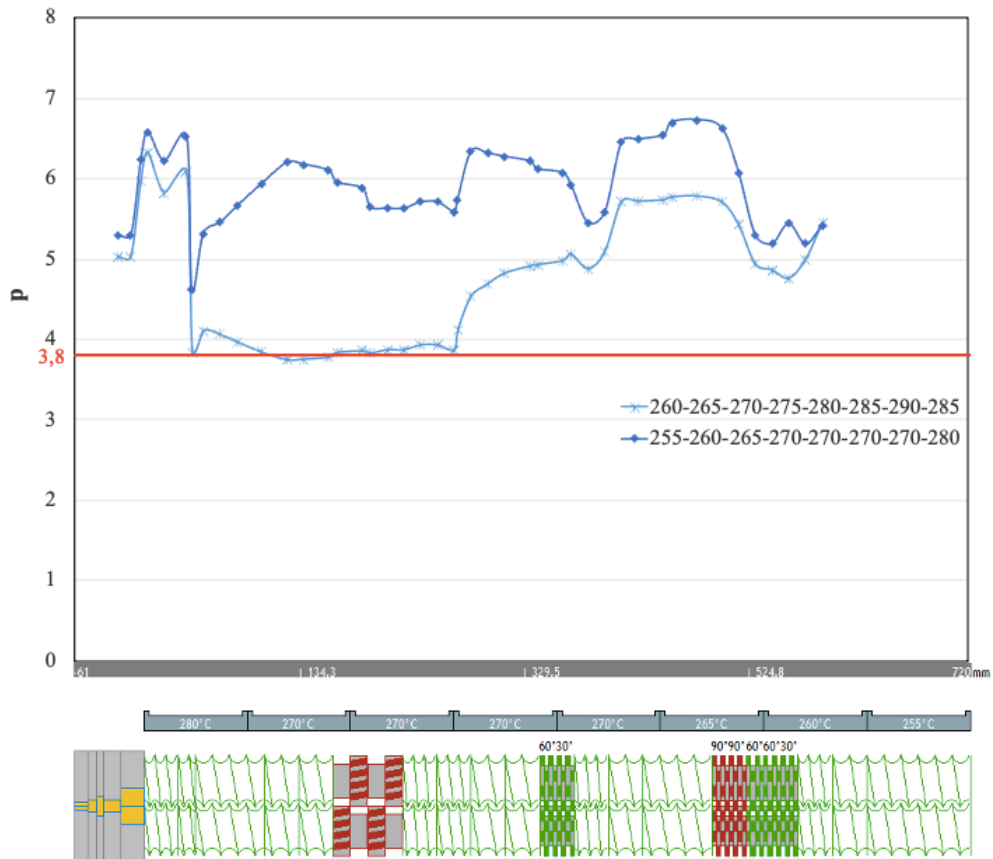


Figure 141. Viscosity ratio  $p$  as a function of the screw profile when the temperature profile changes.

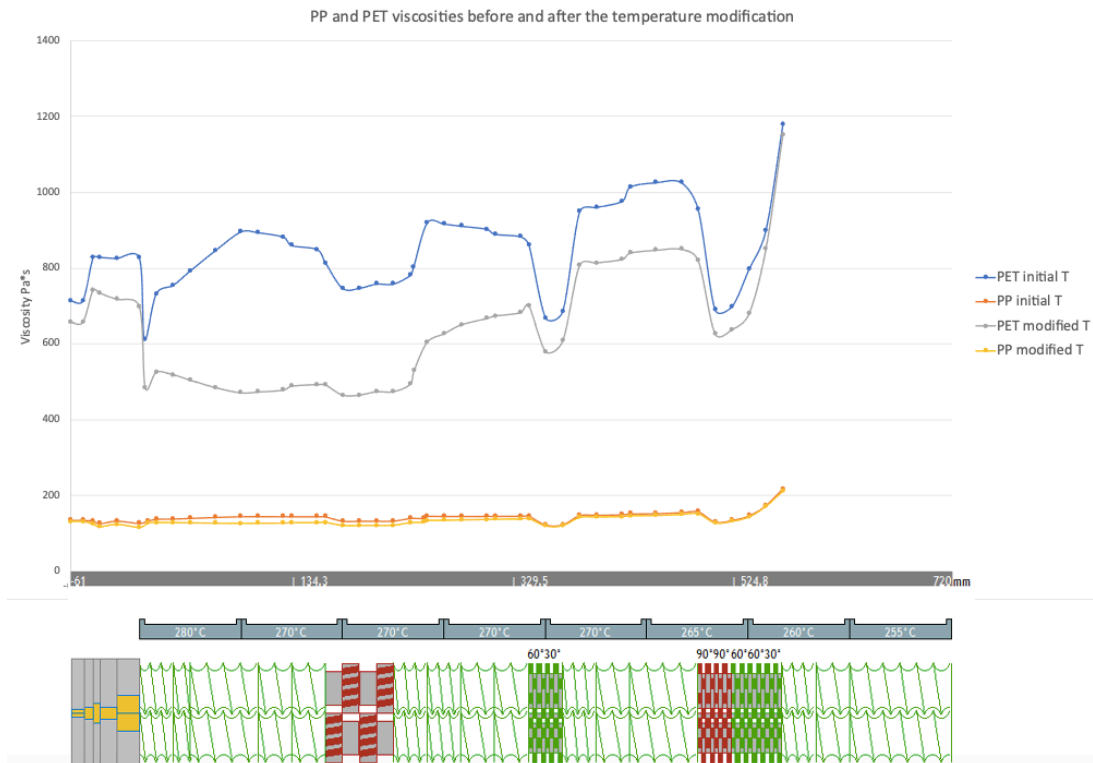


Figure 142. PP and PET viscosities variation with the change of temperature.

## 5. Conclusions

After the definition of the system of interest, composed by 70% wt of PP and 30% wt of PET, the first step of the results analysis consisted in verifying Ludovic software's reliability. To do so, the obtained plots concerning temperature, shear rate, viscosity and residence time were studied. The outcome of the different graphs was satisfactory.

First of all, the temperature and the shear rate curves present a sharp increase in their trend in correspondence of the restricting elements, which is in line with what was expected. Furthermore, the increase in temperature and in the shear rate always provoked a notable decrease in viscosity, that corresponds to what we know that happens with polymers.

Secondly, the increase in the screw speed rotation from 120 to 180, 200 and 250 rpm brought to a general increase in the shear rate. Higher values of shear rates cause a major quantity of dissipated energy that results in higher values of temperature. Consequently, the viscosity experienced a significant decrease. Another aspect to underline is the fact that the increase in screw speed rotation provokes a decrease in the mean residence time that, in the present work, is something undesired because longer residence times promote the formation of thinner and stronger fibrils.

The change in the composition from the initial one to 90%wt of PP and 10%wt of PET did not modify in any significant way the temperature and shear rate profile, while it produced a notable decrease in the viscosity plot. This is correct, in fact the 90% of the blend is composed by PP, which is the material with the lower viscosity. For this same reason, also the mean residence time presents slightly lower values.

After all these considerations, it has been concluded that the results obtained with Ludovic are reliable and its sensitivity is good enough to employ this software to evaluate the selected system's behavior when some changes in the parameters occur.

In order to choose the best conditions for the system analyzed in this work, instead, another study has been carried out as explained by García-Masabet et al. [11]. In particular, it has been found out that the fibrils can be formed in a polymer blend when the ratio between the reinforcing material's viscosity and the matrix material's one is major than 3,8. So, this viscosity ratio has been calculated for all the simulations launched in order to evaluate the best conditions to obtain fibrils in our system. In this way, it has been concluded that the best screw speed rotation to promote fibrils' formation is the lowest one, 120 rpm, but also 180 and 200 rpm produce a viscosity ratio higher than 3,8 in every position inside the extruder, so they can also be employed. The worst one appeared to be 250 rpm, that lays down the 3,8 value in some points. As far as the temperature profile is concerned, the best one was the first applied, 255, 260, 265, 270, 270, 270, 270, 280°C. The second one had slightly higher values that provoked a remarkable decrease in PET viscosity, which led to a sharp drop of the viscosity ratio, in various cases below the 3,8 value.

## 6. References

- [1] H.S. Xu, Z.M. Li, J.L. Pan, M.B. Yang, R. Huang, "Morphology and Rheological Behaviors of Polycarbonate/High Density Polyethylene in situ Microfibrillar Blends", *Macromolecular Materials and Engineering*, vol. 289, pp. 1087-1095, 2004.
- [2] K. Jayanarayanan, T. Jose, S. Thomas, K. Joseph, "Effect of draw ratio on the microstructure, thermal, tensile and dynamic rheological properties of in-situ microfibrillar composites", *European Polymer Journal*, vol. 45, pp. 1738-1747, 2009.
- [3] S. Fakirov, D. Bhattacharyya, R.J. Shields, "Nanofibril reinforced composites from polymer blends", *Colloids and Surfaces A-Physicochemical and Engineering Aspects*, vol. 313, pp. 2-8, 2008.
- [4] M. Kuzmanović, L. Delva, L. Cardon, K. Ragaert, "The Effect of Injection Molding Temperature on the Morphology and Mechanical Properties of PP/PET Blends and Microfibrillar Composites", *Polymers*, vol. 8, pp. 355-341, 2016.
- [5] A.R. Kakroodi, Y. Kazemi, W. Ding, A. Ameli, C.B. Park, "Poly(lactic acid)-Based in Situ Microfibrillar Composites with Enhanced Crystallization Kinetics, Mechanical Properties, Rheological Behavior, and Foaming Ability", *Biomacromolecules*, vol. 16, pp. 3925-3935, 2015.
- [6] K. Jurczuk, A. Galeski, E. Piorkowska, "All-polymer nanocomposites with microfibrillar inclusions generated in situ during compounding", *Polymer*, vol. 54, pp. 4617-4628, 2013.
- [7] K. Jurczuk, A. Galeski, "Thermoplastic elastomers reinforced with poly (tetrafluoroethylene) nanofibers", *European Polymer Journal*, vol. 80, pp. 58-69, 2016.
- [8] W. Li, A.K. Schlarb, M. Evstatiev, "Influence of Processing Window and Weight Ratio on the Morphology of the Extruded and Drawn PET/PP Blends", *Polymer Engineering and Science*, vol. 49, no. 10, pp. 1929-1936, 2009.
- [9] P. Taepaiboon, J. Junkasem, R. Dangtungee, T. Amornsakchai, P. Supaphol, "In Situ Microfibrillar-Reinforced Composites of Isotactic Polypropylene/Recycled Poly(ethylene terephthalate) System and Effect of Compatibilizer", *Journal of Applied Polymer Science*, vol. 102, pp. 1173-1181, 2006.
- [10] A. Huan, X. Peng, L.S. Turn, "In-situ fibrillated polytetrafluoroethylene (PTFE) in thermoplastic polyurethane (TPU) via melt blending: Effect on rheological behavior, mechanical properties, and microcellular foamability", *Polymer*, vol. 134, pp. 263-274, 2018.
- [11] V. García-Masabet, O. Santana Pérez, J. Cailloux, T. Abt, M. Sánchez-Soto, F. Carrasco, M.L. Maspocho, "PLA/PA Bio-Blends: Induced Morphology by Extrusion", *Polymers*, vol. 12, 2019.
- [12] SCC Consultants, "Ludovic User's Manual - v7.0".
- [13] H. P. Grace, "Dispersion Phenomena in High Viscosity Immiscible Fluid Systems and Application of Static Mixers As Dispersion Devices in Such Systems," *Chemical Engineering Community*, vol. 14, pp. 225-277, 1982.
- [14] F. Zhong, J. Schwabe, D. Hofmann, J. Meier, R. Thomann, M. Enders, R. Mülhaupt, "All-polyethylene composites reinforced via extended-chain UHMWPE nanostructure formation during melt processing", *Polymer*, vol. 140, pp. 107-116, 2018.
- [15] J. Zhao, Q. Zhao, L. Wang, C. Wang, B. Guo, C.B. Park, G. Wang, "Development of high thermal insulation and compressive strength BPP foams using mold-opening foam injection molding with in-situ fibrillated PTFE fibers", *European Polymer Journal*, vol. 98, pp. 1-10, 2018.
- [16] Z. Li, Y.S. Shi, C.X. Sun, Q. Zhang, Q. Fu, "In situ micro and nano fibrillar reinforced elastomer composites based on polypropylene (PP)/olefinic block copolymer (OBC)", *Composites Science and Technology*, vol. 115, pp. 34-42, 2015.

[17] A. Rizvi, C.B. Park, B.D. Favis, “Tuning viscoelastic and crystallization properties of polypropylene containing in-situ generated high aspect ratio polyethylene terephthalate fibrils”, *Polymer*, vol. 68, pp. 83-91, 2015.